ABSTRACT

Title of Dissertation:	INNOVATIVE SCANNING PROBE METHODS FOR ENERGY STORAGE SCIENCE: ELUCIDATING THE PHYSICS OF BATTERY MATERIALS AT THE NANO-TO-MICROSCALE
	Jonathan Michael Larson, Doctor of Philosophy, 2018
Dissertation directed by:	Professor and Chair, Janice E. Reutt-Robey, Department of Chemistry and Biochemistry

In recent decades, approaches to generate electrical energy through renewable means has greatly benefited from technological advancements. However, the need for robust schemes to store that energy in safe and cost-effective manners persists. Thus, there is a shared global call to advance electrical energy storage science and technology. Breakthroughs in the field stand to impact humans, ecosystems, environments, economies, and even international security. Currently, many innovative routes rooted in basic science are being taken to develop novel concepts, chemistries, electrolytes, and geometries for electrical energy storage. Many of these approaches make use of nano-to-mesoscale structures and technologies which increases the demand for new methods of characterization and scientific discovery at those scales. Still, progress to address this demand is stymied by practical

scientific and technological challenges associated with the buried interfaces in battery systems.

In this dissertation, I present how my PhD work has precisely targeted this need within the energy storage community, and made lasting impact. I detail why, and how, I have pioneered scanning-probe based technologies and techniques that make use of "battery probes" consisting of electrochemically active materials. A suite of techniques is developed and leveraged for basic electrical energy storage science: scanning nanopipette and probe microscopy, pascalammetry with microbattery probes, inverted scanning tunneling spectroscopy, and nanoscale solid-state electrochemistry with nanobattery probes. The use of these techniques motivated finite-element numerical simulations of electrostatic potentials, and electric fields, at play during field-driven lithiation of multi-walled carbon nanotubes. Also motivated were analytical models for surface diffusion and diffusion through a stressed electrolyte simultaneously experiencing latent-species activation.

INNOVATIVE SCANNING PROBE METHODS FOR ENERGY STORAGE SCIENCE: ELUCIDATING THE PHYSICS OF BATTERY MATERIALS AT THE NANO-TO-MICROSCALE

by

Jonathan Michael Larson

Dissertation submitted to the Faculty of the Graduate School of the
University of Maryland, College Park, in partial fulfillment
of the requirements for the degree of
Doctor of Philosophy
2018

Advisory Committee:
Professor, Theodore L. Einstein, Chair
Professor, Sang Bok Lee
Professor, Janice E. Reutt-Robey, Advisor
Professor, Ellen D. Williams
Assistant Professor, James R. Williams

Dedication

To my wife Kristin

You are my best friend and awake in me the desire to be a better person.

To my children

You are the source of so much joy and motivation in my life.

To my parents

Your steadfast love and provision will never be forgotten, you enabled this feat.

To my grandfather “Bapa”

You are my inspiration and the scientist and grandfather I aspire to be.

Acknowledgements

In route to graduate school I received a common thread of advice from personal mentors – choose your advisor wisely. I was told that this choice could make or break the graduate school experience. I am extremely thankful that over the course of my graduate career I have been able to call Janice Reutt-Robey my advisor. Janice holds a rare breadth of knowledge spanning chemistry, surface science, vacuum technology, physics, and scanning probe microscopy, and has been vital to my personal development as a scientist during my graduate studies. Janice has the ability to "see" problems through multiple scientific and technological lenses in such a way to leverage her interdisciplinary expertise to facilitate innovation. Being exposed to her unique sets of skills has inspired me, and continues to inspire me, to strive for similar attributes as a scientist.

I would like the thank Janice for the many hours of scientific discussions we have had over the course of my graduate studies at group meetings as well as during unscheduled drop-in meetings. I have learned a great deal from you, to which I am very grateful. Thank you also, Janice, for supporting my studies financially, without which this work could not have happened. And finally, beyond providing me the aforementioned, Janice has been a consistent source of encouragement and understanding over the years. In all these ways, and more, she has shown me a great first-hand model of an effective principal investigator, and exemplary boss.

During my graduate studies, I have also had the distinct privilege of having Theodore (Ted) Einstein as my co-advisor. I entered the University of Maryland in the chemical physics Ph.D. program, and during my first year of studies I began to consider the possibility of transferring to the physics Ph.D. program. I discussed this possibility with Ted, and he was extremely supportive, and encouraging. I am not sure if he knows, but his confidence in me during that time was pivotal, and I want to thank him for believing in me and my potential. After the transition to the physics program was complete, Ted graciously agreed to serve as my co-advisor. Thank you for taking me on even though I was an experimentalist, and the likelihood of direct collaboration was limited. Also, thank you for always being available/willing to read over my diffusion models, provide advice, or just talk physics. You have challenged me to become a clearer, more precise physicist, and I sincerely thank you for that.

Janice and Ted have both been significant resources of important scientific perspectives for research, as well as advice on writing and oral presentations, thank you both. I also want to thank Janice and Ted for allowing me to serve as a guest lecturer in their classes on a number of occasions.

Thanks also go to William Cullen for his instrumental help and guidance on all things scanning probe related over the years. Early in my graduate studies Bill helped to introduce me to all the nitty gritty details of scanning probe microscopy, and was always willing and able to answer questions. Later in my graduate studies,

after he went to the National Institutes of Standards and Technology, he was still always just an email or phone call away, thank you.

On a similar note, I would like to thank Satyaveda Bharath for his time and help regarding scanning probe microscopy training early in my graduate studies, as well as being a research collaborator.

Also from the University of Maryland, special thanks go to Kristen Burson and Jake Tosado who were always willing to chat and share advice on all things relating to graduate school, qualifier exams, teaching, physics, and looking for jobs. Other colleagues I have had the pleasure of working with at the University of Maryland I would like to acknowledge are: Yilin Wang, Keith Gregorczyk, Karen Gaskell, Wentao Song, Nam Kim, Qian Shao, Eric Rosenthal, Dennis Wang, Jeremiah Wathen, Avinash Kumar, Neal Pisenti, Alexander Kozen, Alexander Pearse, Alexander Yulaev, Joel Dahlin, and Yi-Hsieh Wang.

I would also like to especially thank the Energy Frontier Research Center Nanostructures for Electrical Energy Storage. Both director Gary Rubloff, and co-director Sang Bok Lee have been wonderful sources of information on electrochemistry and atomic layer deposition, and generally good examples of successful project managers of large scientific efforts. They also entrusted me with a number of opportunities to publically represent the energy frontier research center, to which I am both humbled and thankful for the experience.

Alec Talin has been an invaluable collaborator I would like to thank within the center. Alec has been instrumental in fabricating nanobattery probes and discussing efficient scientific approaches to characterize energy materials with novel scanning probe approaches. Without Alec's help, the nanobattery work would have been greatly inhibited.

I would also like to thank Elizabeth Lathrop for being so polite, helpful, and organized in all her many center-related efforts and initiatives. Other colleagues from the Energy Frontier Research Center I would like to specifically thank are Xin (Sylvia) Le, Mya Le Thai, and Timothy Plett.

Finally, I want to thank and acknowledge my wife Kristin. It is hard to overstate the amount of time, energy, and effort you have spent over the years supporting me (and our family) in this endeavor. Thank you for this steadfastness and love, it has been key to my success.

Table of Contents

List of Figures

List of Abbreviations

AFM	Atomic Force Microscopy
ALD	Atomic Layer Deposition
BP	Battery Probe
CNT	Carbon Nanotube
CV	Cyclic Voltammetry
DAE	Diffusion Activation Equation
DAT	Diffusion Activation Theory
EES	Electrical Energy Storage
HOPG	Highly Ordered Pyrolytic Graphite
ISTS	Inverted Scanning Tunneling Spectroscopy
LCO	Lithium Cobalt Oxide
LDOS	Local Density of States
LiPON	Lithium Phosphorus Oxynitride
MBP	Microbattery Probe
MWCNT	Multi-Walled Carbon Nanotube
NBP	Nanobattery Probe
NC-AFM	Non-Contact Atomic Force Microscopy
ROC	Radius of Curvature
ROI	Region of Interest
SAD	Stress-Assisted Diffusion
SEM	Scanning Electron Microscopy

SLi-NPM	Scanning Lithium Nanopipette and Probe Microscopy
SNPM	Scanning Nanopipette and Probe Microscopy
SPM	Scanning Probe Microscopy
SSE	Solid-State Electrolyte
STM	Scanning Tunneling Microscopy
STS	Scanning Tunneling Spectroscopy
UHV	Ultra-high Vacuum

Chapter 1: Scanning Battery Probes for Energy Storage Science

1.1 Basic Electrical Energy Storage Science: Context, Needs, and Challenges

The pursuit of advancements in electrical energy storage (EES) solutions is increasingly in the public and scientific spotlights due to wide-ranging implications for the climate[1,2], economy[3], and national security[4]. Despite progress in methods to generate electrical energy by renewable means such as geothermal[5], wind[6], water[7], and solar[8-10], needs persist to store energy in safe, reliable, and cost-effective manners[11]. Two specific examples for which substantial advancements are needed are grid-scale storage and economically viable safe vehicular batteries. An essential foundation for these endeavors is the progression of basic energy science, the enabler to innovation.

In recent years, many creative and cutting-edge approaches to EES have begun to materialize. Rooted in fundamental scientific ingenuity, innovations are being made in storage concepts[12-14] and chemistries[15-18], electrolyte materials[19-21], interfacial layerings[22-24], and geometries[25-27]. These advances notwithstanding, progress in EES research is stymied by a combination of unique challenges, not least of which is the implicit interdisciplinary nature of the science. Certainly, EES science is comprised, at a minimum, of components in chemistry, electrical engineering, materials science, mathematics, and physics, and as such, is practically challenging. Beyond this general challenge, specific

challenges to basic EES science exist. In batteries, two specific challenges are buried interfaces and averaged properties.

Within functioning batteries there are a minimum of four heterogeneous materials interfaces. A cross-sectional schematic of a full-cell battery shown in Figure 1 highlights these interfaces with red arrows. The four heterogeneous interfaces correspond to eight material surfaces of functional importance. Adopting a "top-to-bottom" terminology referencing the battery schematic in Figure 1, the interfaces are: current collector(bottom) joining anode(top), anode(bottom) joining electrolyte(top), electrolyte(bottom) joining cathode(top), and cathode(bottom)

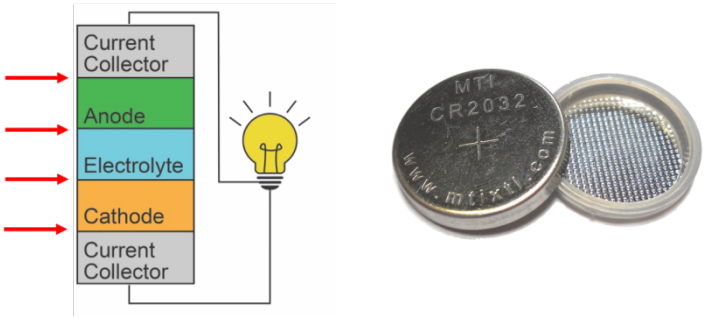

Figure 1: Battery Schematic (left) and Coin-Cell Battery Casing (right)

joining current collector (top). From a basic science perspective, controllable study of these interfaces and component surfaces is a major challenge.

A second specific challenge for the advancement of basic EES science is moving beyond characterizing battery properties in ways that average information over multiple and expansive interfacial areas, thereby obscuring potentially important variations in local materials properties. The lion's share of battery research[28,29] is conducted on full-cell batteries encapsulated in "coin cells" on the order of a centimeter in diameter, as depicted on the right-hand side of Figure

1. Subsequent measurements and data analysis of these coin cell batteries are largely insensitive to inhomogeneity in morphology, defects composition, and electrochemical potential that exist at the buried interfaces and surfaces. While the coin-cell approach is essential for benchmarking full-cell performance, and will/must remain a cornerstone of battery testing, intensive efforts to integrate micro-to-nanoscale technologies[30-33] into EES devices call for new approaches to characterize battery materials properties at those scales.

Based on these challenges, the EES research community stands to benefit greatly from new, and enabling, technologies, techniques, and theories. Particularly important are those that precisely target and characterize battery-relevant interfacial and surface properties at the micro-to-nanoscale. New interface-specific information can be used to provide feedback for future battery design. This perspective has helped to fine-tune research vectors throughout my Ph.D. as I strived to generate work to impact EES. This dissertation builds off surface physics approaches to interfacial and nanoscale science, extending these methodologies and conceptual framework to battery-relevant materials.

1.2 Scanning Probe Microscopy: Interfacial Science at the Nanoscale

Arguably the best-known and successful methods for studying nano-to-microscale phenomena at interfaces are based in scanning-probe microcopy (SPM). The advent of SPM approaches in the 1980's, such as scanning tunneling microscopy (STM)[34,35] and atomic force microscopy (AFM)[36,37], have in the following decades enabled atomic[38,39] resolution imaging, diverse schemes of

interfacial characterization[40], and manipulation at surfaces[41]. Indeed, the storied success of SPM has resulted in countless peer-reviewed papers, and volumes of books; it remains a centerpiece of many experimental surface science research efforts.

Generally, in SPM approaches, a probe is brought close enough to a surface for tip-sample interactions to arise, enabling characterization techniques. The sharp apex of the probe (the tip) is ideally atomically sharp, but usually has a radius of curvature between 10^0-10^1nm. As displayed in Figure 2, in STM, the probe and sample are electrostatically biased, and the tip-surface separation distance is reduced. Eventually the electron wave functions for each overlap and allow electron tunneling current between the two. The magnitude of this current, exponentially dependent on tip-surface separation distance[35], can then be used in combination with an electronic feedback loop (control electronics in Figure 2) to scan over a surface and reconstruct a three-dimensional image of the nanoscale terrain. As STM measures the local density of states (LDOS)[35], topographic STM images provide atomically resolved information on surface electronic structure and symmetry, and can be analyzed for structure. AFM, conducted in either contact or non-contact modes, provides a quantitative measure of topography through force measurements.

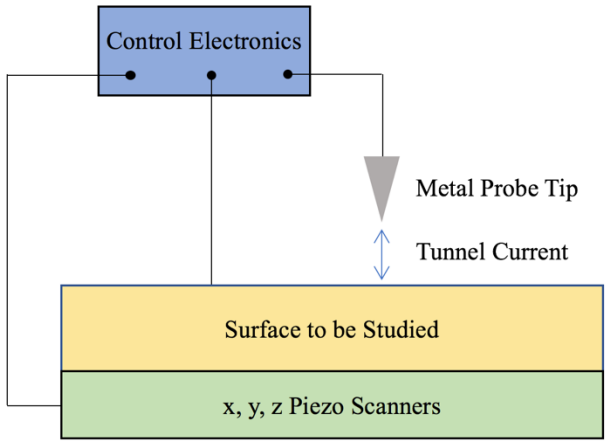

Figure 2: Schematic of scanning tunneling microscope (STM)

Beyond topography, SPM approaches can be used to map many varied surface properties. To list a few, approaches (surface properties) include Kelvin probe force microscopy (electrostatic potential)[42,43], scanning tunneling spectroscopy (electron band gap)[44,45], and constant current STM (electron density of states)[46]. Over the decades since 1980, the proliferation and use of SPM approaches has spread into many disciplines[47], including those related to energy science[48-50]. While some liquid-electrolyte based SPM approaches[51,52] have reached a level of commercialization, solid-state approaches for local nano-to-microscale electrochemical characterization are limited[53]. As a result, a fundamental understanding of micro-to-nanoscale ion transport phenomena and related properties in solid electrochemically active materials remains elusive.

1.3 Hybridization of Scanning Probe Microscopy and Solid-State Electrochemistry

To address the need to characterize electrochemical properties at the nanoscale, and overcome the challenges associated with buried relevant interfaces, I have developed a new class of scanning probe: a battery probe (BP). Broadly defined, BPs are STM or AFM probes comprised of, or coated with, electrochemically active materials. These innovative BPs move beyond serving solely as passive current collectors and serve as active elements in solid-state electrochemical reactions that can be performed (or confined) to the nano-to-microscale. In Figure 3 is a schematic diagram of the apex of a conventional probe and BP.

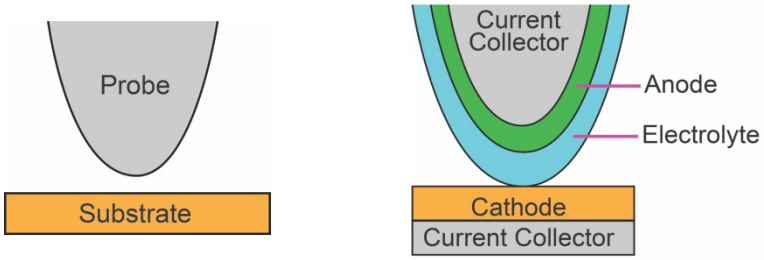

Figure 3: Schematic of conventional SPM probe, shown in non-contact geometry for STM or NC-AFM measurements (left) and Battery Probe (BP) shown in operational contact geometry (right)

As concisely described in the following section, this novel BP technology can be used to accomplish local solid-state electrochemistry at the nanoscale and microscale. At the nanoscale (microscale) the term nanobattery probe (microbattery probe) is adopted and denoted as NBP (MBP). The use of BPs for local electrochemical experiments in a SPM system allows the electrochemical cells to be closed (by probe approach) or non-destructively broken (by probe

retraction) for subsequent characterization with conventional SPM in-situ. A powerful utility of this approach is the ability to select the interface/surface to be studied by choice of BP materials/layerings. As well as enabling unique SPM-based solid-state electrochemistry measurements, BPs also serve as a platform for further technique innovation, as will be shown with scanning nanopipette and probe microscopy, pascalammetry, and inverted scanning tunneling spectroscopy. This technology, in combination with resultant techniques and theories, addresses critical EES research needs and allows for quantitative exploration of defined interfaces under operational conditions.

1.4 Overview: Leveraging Innovative Technologies, Techniques, and Theories

The main focus of this dissertation is to convey the design, development, and exploitation of scan-probe based approaches I have developed that advance the capability to characterize model solid-state EES systems. The novel technologies and techniques are all fundamentally related due to the centrality of multi-functioning electrochemically active probes. These innovative technologies, techniques, and complementing theories, help to overcome challenges to basic EES science, and enable the collection and analysis of data on battery material interfaces at the micro-to-nanoscale. In the remainder of this section I present brief summaries of the forthcoming chapters, providing snapshots into the impact and utility of leveraging these technologies, techniques, and theories for the advancement of basic EES science.

In chapter two I present a carbon-nanotube-enabling scanning probe nanotechnology and technique for manipulating and measuring lithium at the nano-

mesoscale. Scanning nanopipette and probe microscopy (SNPM)[49] is based on a conductive atomic force microscope (AFM) cantilever with an open-ended multi-walled carbon nanotube (MWCNT) affixed to its apex, as shown in Figure 4. SNPM operation is demonstrated with a model system consisting of a Li thin film on a Si(111) substrate. By control of bias, separation distance, and contact time, attograms of Li can be controllably pipetted to or from the MWCNT tip. Patterned surface Li features are then directly probed via non-contact AFM measurements with the MWCNT tip. The subsequent decay of Li features is modeled with a mesoscale continuum theory specifically developed to quantify the evolution of Li features. The Li surface diffusion coefficient for a four (two) Li layer thick film is thus measured as $D=8.0(\pm1.2)*10^{-15}cm^2s^{-1}$ ($D=1.75(\pm0.15)*10^{-15}cm^2s^{-1}$). Dual Li pipetting and measurement with the SNPM enables a broad range of time-dependent Li and nanoelectrode characterization studies of fundamental importance to energy storage research.

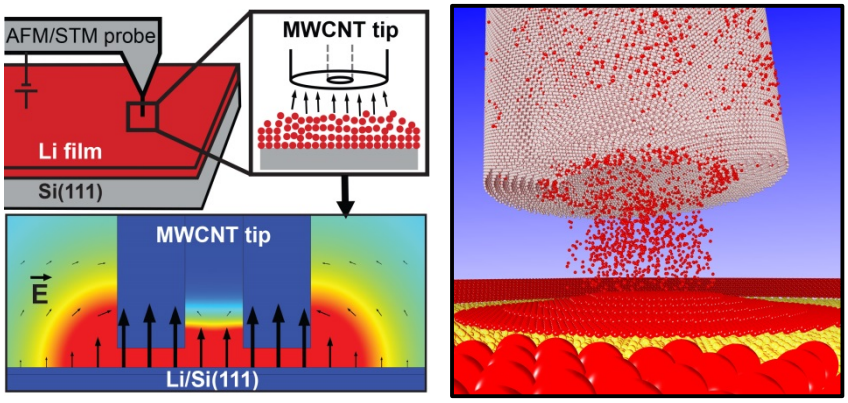

Figure 4: Schematic of scanning Li-nanopipette and probe microscopy

In chapter three I introduce a technology (MBP), technique, and analytical framework, used in tandem for the first controlled study of stressed EES devices. The new technology is called a microbattery probe, and the realization of this technology is described in section 3.3. When stress is applied to a solid-state electrochemical device through microbattery probes (left-hand side Figure 5), faradaic current transients are induced and measured (right-hand side Figure 5). I introduce the term Pascalammetry to describe such Pressure-Current measurements at fixed voltage. Pascalammetry measurements performed with operando solid-state microbattery probes (Li_2O/Li) and Si cathodes reveal stress-assisted Li+ diffusion. I show how non-Cottrellian active-lithium diffusional kinetics signals stress and provides a signature of stress-induced battery degradation. A "diffusion/activation" theory is presented, and a corresponding diffusion/activation equation is analytically solved to describe this non-Cottrellian signature, with characteristics distinct from Cottrell's classic solution for unstressed systems. This technique provides unprecedented opportunity to detect stress in solid-state battery electrolytes and to provide critical, quantitative information regarding the stress-related degradation and failure modes in these energy storage devices.

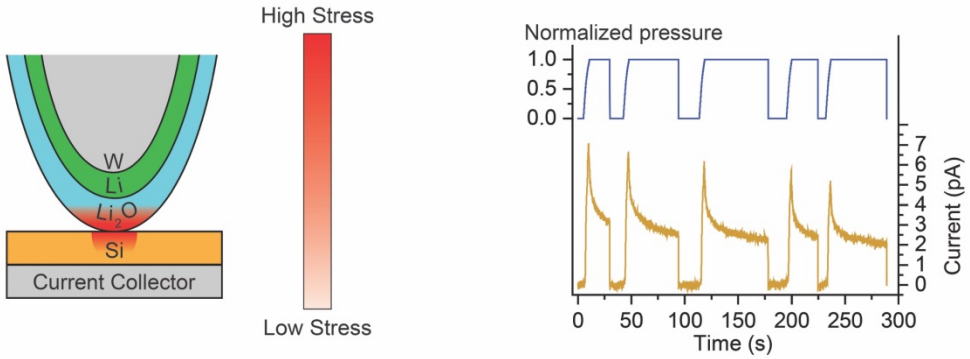

Figure 5: Schematic of a stressed microbattery probe during a pascalammetry measurement (left) and representative data (right)

In chapter four I present preliminary results on a new approach/technique to measure local interfacial structure, electronics, and electrochemical properties as a function of local chemical changes, like lithiation. This is accomplished by a novel hybrid invention NBPs (Figure 6). These efforts are motivated by the need for greater knowledge of interfacial charge/mass transport processes in battery materials - especially as a function of lithiation - to understand and overcome materials limitations in performance. Also, increased use of nanostructured and/or nanoscale electrodes in energy storage systems, calls for research tools that allow for direct, local probes of materials interfaces and inhomogeneity. I describe these NBPs, conventional scanning tunneling microscopy probes layered with nano-thin, functional energy-storage materials. I perform in situ measurements of the electronic properties of oxide-clad probes, via inverted tunneling spectroscopy, determining effective electron transport gaps. I then utilize these probes as fine Li sources and as nanobattery probes for local cycling against anodic substrates silicon

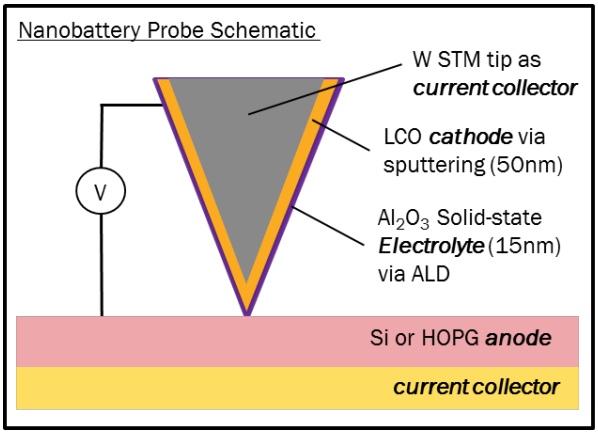

Figure 6: Schematic, with details, of nanobattery probe (NBP) for local, nanoscale, solid-state electrochemistry

and highly ordered pyrolytic graphite. In this way, local, nanoscale, solid-state electrochemistry is accomplished.

In chapter five, I summarize the totality of my work described in this dissertation. I begin by reiterating the contextual relevancy of my research perspective that motivated the development of BPs, SNPM, pascalammetry, inverted tunneling spectroscopy, and related theories. I then proceed to highlight key accomplishments, significance, and impact of these innovative approaches. Vectors for potential future research projects, and their promise for impact, are discussed. Finally, in the appendices, I provide derivations/justifications for modeling approaches, and Mathematica code used for diffusion simulations and analysis.

Chapter 2: Scanning Nanopipette and Probe Microscopy

Acknowledgment: This work was published in the journal *Small* in 2015[49]. Authors who participated in the work are as follows, with associations held at the time:

Jonathan M. Larson[1] (J.M.L.), *Satyaveda C. Bharath*[2] (S.C.B.), *William G. Cullen*[1] (W.G.C.), and *Janice E. Reutt-Robey*[2] (J.E.R-R.)

University of Maryland Department of [1]Physics, [2]Chemistry and Biochemistry

J.M.L., J.E.R-R., and S.C.B. conceived of the experimental possibility. J.M.L. discovered, and initially developed, the scanning nanopipette and probe technique. W.G.C. performed control experiments and assisted J.M.L. and S.C.B. with experimentation and data acquisition. J.M.L. and S.C.B. prepared samples, and carried out experiments. J.M.L. modeled electrostatics, designed the diffusion simulation, analyzed the data, and wrote the paper. J.E.R-R., S.C.B., and W.G.C. edited the paper. All authors discussed the results and implications.

2.1 Introduction

Nanotechnology advances have come about through the development of new tools to measure and manipulate materials at the nano-mesoscale. Pipettes are particularly powerful tools that enable deposition and/or extraction of select materials with length dimensions in the nanometer to micrometer regime[54,55]. Diverse fields have made use of these so-called "nanopipettes" (or "micropipettes") in far-reaching applications. Nanopipettes (micropipettes) have acted as cellular syringes[56,57], detectors of single molecules of DNA[58], scaffolds for sub-microliter droplet pH detection[59], and DNA traps for miniaturized biological analysis[60], to list a few representative applications. Carbon nanotubes (CNTs) functioning as nanopipettes have acted as nanoscale switches[61], "nanorobotic" copper spot welders[62], electromechanical memory devices[63], and conduits for metal transport[64-67]. The mechanisms of material storage and motion within CNTs have also been studied theoretically[68-70]. While powerful CNT-based nanopipette applications have been developed, many more are yet to be discovered.

In 2004 a CNT-based "tool" that could "efficiently deliver" groups of atoms to or from a "work area" as well as perform scanning probe microscopy (SPM) measurements in situ, was proposed[71]. Zettl et al., perhaps partially inspired by advancements in scan-probe lithographic methods[72-74], envisioned a technique/nanotechnology that would exploit the capabilities of CNTs to act as both mass transport vehicles and SPM probe tips. We dub this technique Scanning Nanopipette and Probe Microscopy (SNPM). In principle, SNPM would give experimentalists robust access to controlled nano-micro scale manipulation

expanding further the SPM measurement arsenal[35,37]. In the present work, we present the first realization of SNPM through controlled lithium transfer and patterning, in combination with in situ SPM structural measurements. This new tool could further enable mechanistic studies of lithiation processes in energy storage devices.

Advanced energy-storage materials and designs demand new tools to characterize Li transport and nanoelectrode response at the nanoscale. This need has driven the development of innovative SPM techniques such as electrochemical strain microscopy[75-77] and scanning ion conductance microscopy[78]. Nonetheless, no single SPM method to date fulfills the needs for complete nanoelectrode characterization[79]. Intrigued by the potential benefits SNPM could contribute to nanoelectrode characterization efforts as well as fundamental energy storage research in general, our lab set out to develop this technique. Herein we introduce SNPM in which the multi-walled carbon nanotube (MWCNT)/nanopipette/scan-probe tip is actuated for Li manipulation/transport as well as SPM: Scanning Li-Nanopipette and Probe Microscopy (SLi-NPM).

SLi-NPM enables precision nanoelectrode lithiation and transport studies in an ultrahigh vacuum (UHV) environment to extract fundamental information about the intercalation and diffusion of Li in a solid-state battery environment. Previous scan probe studies have shown how a conventional metallic tip can be used to deposit Li on a surface[80-82]. The SLi-NPM complements and expands upon these methods through multimode operational features: (i) The ability to perform in situ time-resolved SPM measurements such as scanning tunneling

microscopy (STM), atomic form microscopy (AFM), and conductive AFM with nm resolution, (ii) an extremely precise and controllable integrated Li ion source or sink, (iii) a high level of systemic mechanical integrity (able to make mechanical contact with surfaces without jeopardizing imaging function), and (iv) an integrated nanoelectrode (the MWCNT tip) highly relevant to advanced battery technology[83-85] with the potential to be chemically functionalized[86,87]. In the remainder of the manuscript we present the development, first demonstration, and application of SNPM: a SLi-NPM for integrated Li-ion CNT-nanopipetting and nanoimaging for basic energy storage applications.

2.2 Development and Demonstration of SLi-NPM

The SLi-NPM is a scan-probe technique/nanotechnology which employs a conductive SPM cantilever with an appended open-ended MWCNT for use as both a Li nanopipette and SPM probe. Development and demonstration was performed with a model thin-film system (see Figure 7 and Section 2.13 below) under UHV conditions in a scanning electron microscopy/STM/AFM facility (JEOL JSPM-4500A). Samples were prepared in situ, and consisted of a thin Li film ($\sim .6 - 1.2\ nm$ thick, equivalent to two – four Li Layers, vapor deposited on a (7x7)-Si (111) substrate at room temperature. Further details on the MWCNT probe and sample are found in the Section 2.13. Upon probe positioning and select bias conditions, the SLi-NPM tip operates as a nanopipette for controlled Li exchanges between the MWCNT and the sample. A probe bias of $-3V$ $(+3V)$, relative to the sample, was reliably used for Li extraction from (deposition to) the sample surface.

These bias conditions were determined experimentally by increasing the electrical bias in successive pipetting attempts until Li transfer had been clearly demonstrated. Post pipetting, the SLi-NPM maintains operational capability of SPM measurements such as STM or NC-AFM measurements.

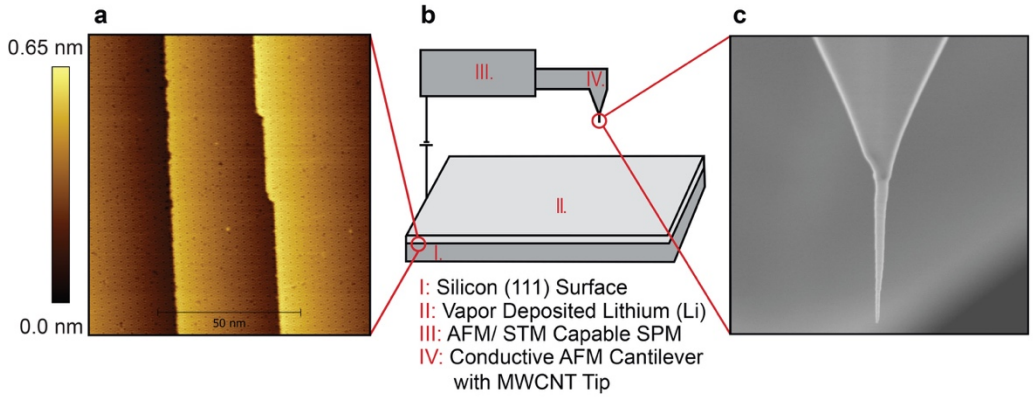

Figure 7: Model system to demonstrate SLi-NPM operation: a) STM image of (7x7)-Si(111) electrode pre lithium deposition. b) Schematic of model system. c) SEM image of MWCNT-terminated tip used for SLi-NPM. The MWCNT is ca. 1 µm long and 30 µm in diameter. A partial Pt coating of the MWCNT increases rigidity and gives a tapered appearance by leaving < 250nm of the apex exposed. The MWCNTs inner volume and intertubular gaps are used for pipetting nanoscale volumes and attogram masses of Li.

2.3 Protocol for SLi-NPM

The detailed protocol for nanopipetting and imaging using the SLi-NPM is shown in Figure 8. In step 1, a survey image is taken in the NC-AFM mode with the MWCNT-terminated probe; followed by probe positioning for the desired pipetting, marked in the figure by a red 'X' (step 2). The probe is then lifted and switched to an STM mode (steps 3 and 4). Feedback is turned off, allowing control of the absolute height (z position) of the probe. The probe is then manually stepped toward the surface under appropriate biasing conditions for Li transfer ($\pm 3\,V$), while monitoring the current signal (step 5).

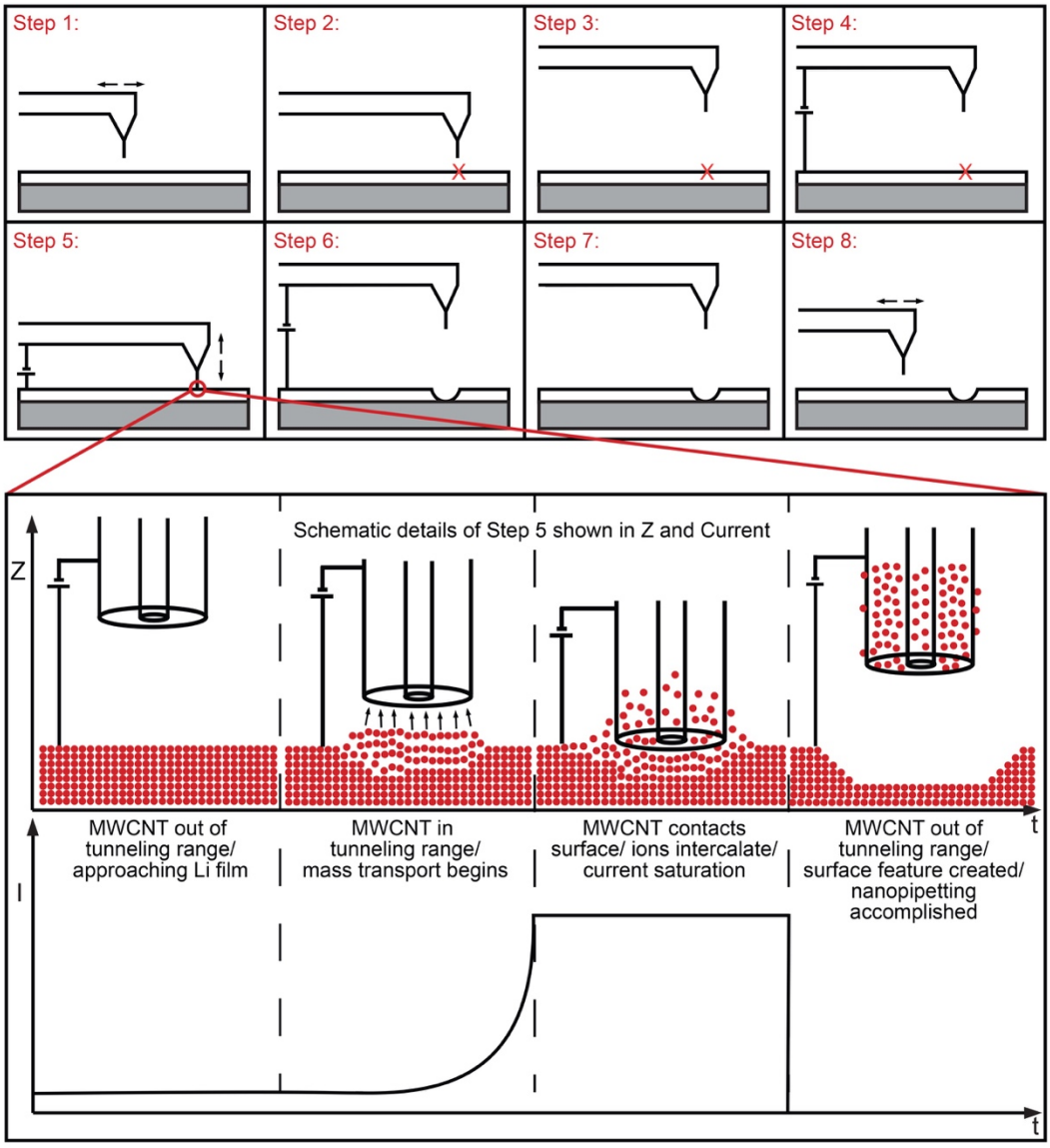

Figure 8: Protocol for Li pipetting and probing using SLi-NPM. This figure qualitatively displays the steps reliably used to pipette Li to the MWCNT tip of the SLi-NPM followed by NC-AFM imaging.

The current reveals the proximity of the probe to the surface. Once a tunneling regime of ~ 1 nA is reached, the probe is stepped toward the surface through the application of small piezo steps (~0.01 nm each) until the MWCNT is in physical contact with the surface (see Section 2.13 below). The transfer (pipetting) of Li begins when the tip is sufficiently "close" (~6Å, see Section 2.2) to the film and

continues while the MWCNT-tip is in mechanical contact with the film (see Section 2.2). The tip may then be slightly retracted and stepped back in for further Li-nanopipetting, or completely retracted to switch the measurement mode to NC-AFM mode (steps 6 and 7). Finally, nanopipetting verification (void observation) and Li diffusion measurements are performed by time-lapse NC-AFM imaging, revealing the evolution of pipette-generated lithium surface features.

Lithium pipetting into the MWCNT probe tip does not degrade performance for sequential NC-AFM measurements. Neither the tube diameter nor the resonant frequency of the cantilever are remarkably altered. Radial expansion of MWCNTs upon lithiation is known to be a modest 5.9%[88], and the amount of mass transferred is insufficient to appreciably alter the cantilever's resonant frequency. This can be understood by estimating the amount of Li transfer required to change the resonant frequency by a small amount, then comparing that amount of Li to the actual physical system. Modeling the cantilever as a cantilevered beam with added end mass[89], $\sim 2\times10^{-5}$ ng (20,000 ag) of Li would need to be pipetted to the MWCNT in order to change the resonant frequency by one one-millionth of a percent. This amount of solid metallic Li would occupy a volume 13 times that of the MWCNT tip. Clearly much less than 2×10^{-5} ng (20,000 ag) of Li could be transferred into the MWCNT tip during a pipetting event. Thus pipetting Li using SLi-NPM does not appreciably alter the cantilever's resonant frequency and NC-AFM measurements post-pipetting are readily performed.

2.4. Pipetting Attograms of Lithium

NC-AFM images obtained before and after a nanopipetting event measure pipette-induced topographic changes and confirm Li transfer. Figure 9 demonstrates the pipetting and probing capabilities of SLi-NPM through a series of "before and after" topographical images (the "X," as in Figure 8, denotes the location selected for nanopipetting).

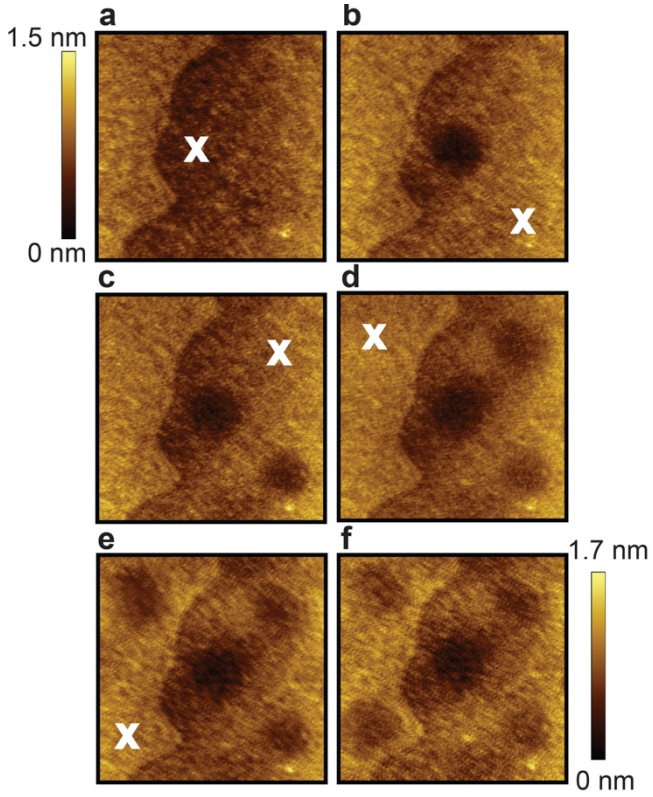

Figure 9: Experimental observation of SLi-NPM-Induced surface vacancy islands: a-f), Series of NC-AFM images (1µm x 1µm) showing the topography of the lithium film before and after five extractive pipetting events in which the tip was biased -3V relative to the Li/Si(111) surface. The red 'X' marks the spot of performed lithium pipetting with the SLi-NPM.

After five site-selective pipetting events the images reveal circular voids in the film where lithium was extracted. In all these pipetting events a fixed -3V potential difference (tip potential minus surface potential) was applied while approaching and making surface contact with the thin Li film. Total contact time of

approximately 115 seconds was used to generate the ~200 nm diameter features shown in Figure 9. While large diameter pits were generated here to demonstrate transfer capabilities, pits with diameters as small as ~80 nm were generated with proportionally smaller contact times (We did not study smaller structures due to their faster decay at our room temperature measurement conditions.).

Once the SLi-NPM tip was loaded with Li by extraction from the Li film, delivery to the surface was also performed. Following placement of the SLi-NPM tip, the tip is biased 3V relative to the surface (substrate potential 3V less than tip potential), thereby expelling Li. This expulsion generates lithium mounds with ~30 nm diameters commensurate to the MWCNT diameter. Lithium deposition from the MWCNT tip was performed on planar Li/Si(111) regions, as well as in SLi-NPM-prepatterned regions. Displayed in Figure 10 is a schematic of this Li-nanopipetting process as well as NC-AFM measurements of Li depositions to both featureless and pre-patterned Li/Si(111) surfaces. A detailed description of the physical principles at work during Li-nanopipetting is presented in Sections 2.7-10.

Quantification of pipette-induced feature volume was facilitated with use of SPM data analysis software Gwyddion: first the feature is identified (as described is Section 2.11) and then its volume is determined. The measured feature volume for a single pipetting event ranged from 100's of nm^3 to 10,000's of nm^3. Using the known density of Li, along with the volume measurements, the amount of Li mass removed from (or deposited to) the film during a single pipetting event ranged in order of magnitude from $10^{-2} - 10^{1}$ ag. Thus, this Li-nanopipetting technique, as described above, supports the controlled transfer of $10^{2} - 10^{6}$ Li atoms to/from

a chosen surface location with nm planar precision. In principle, fewer atoms could be transferred with this methodology, with the non-contact regime best suited to lowest level transfer.

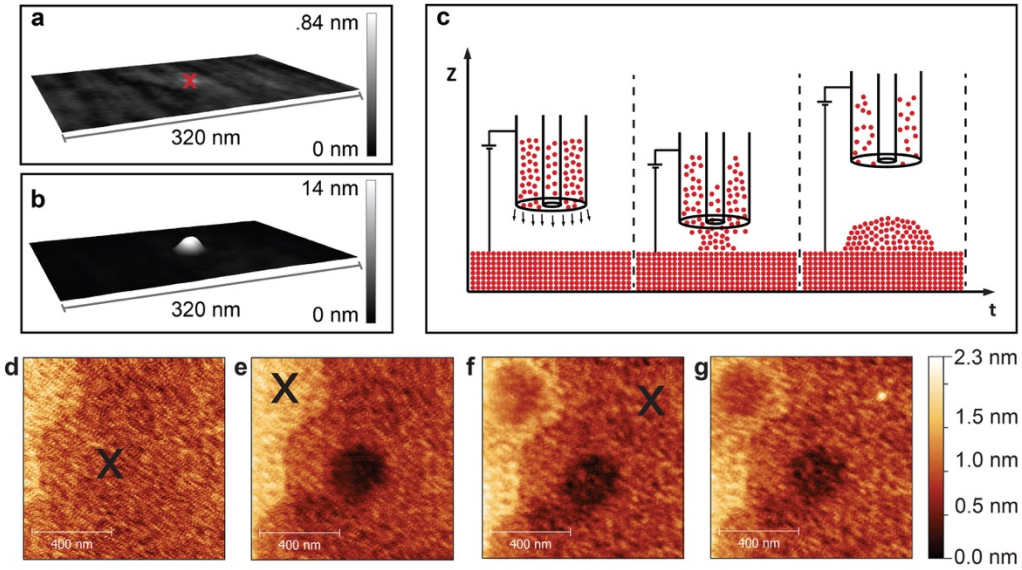

Figure 10: Li pipetting from SLi-NPM to the surface. The red (or black) 'X' marks the designated spot where the pipetting occurs: (a) The smooth Li/Si(111) surface topography imaged by NC-AFM before lithium transfer. b) The surface after pipetting. The ~13nm tall x 25 nm diameter mound was expelled from the MWCNT to the surface by reversing the bias polarity (3V tip bias) and making contact with the surface for ~120s. c) Schematic of experimental protocol for lithium pipetting to the surface. d-g) Series of SLi-NPM-induced features including (e-f) lithium pipetted to the MWCNT tip to generate surface pits by making surface contact for ~250s (-3V tip bias), (g) lithium pipetted from the MWCNT tip to generate a smaller feature than those generated in (b), (e), or (f) by making contact for ~20s (3V tip bias).

2.5 MWCNT-Tip Saturation

After multiple pipetting actions (generally <10) have removed Li from the surface to create multiple ~400 nm diameter voids in the Li film via extraction, a transition in pipette action occurs. The SLi-NPM can no longer extract Li from the surface. Instead, further attempts at Li withdrawal from the surface (i.e. negative tip bias) result in symmetric Li *mound* formation about the point of

attempted pipetting (usually ~300nm diameter protrusions), as displayed in Figure 11 (and Figure 12a-b).

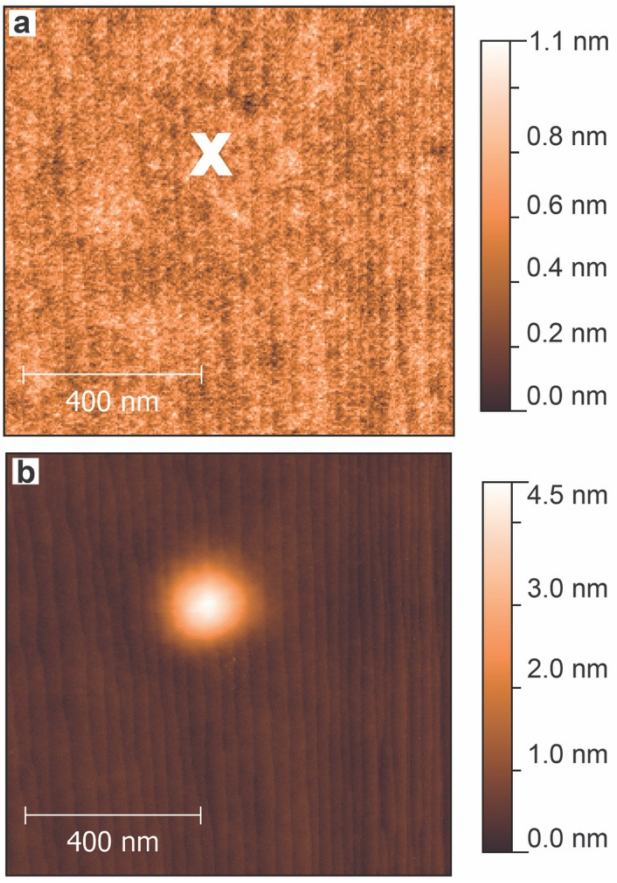

Figure 11: Lithium Necks. a) NC-AFM topography image of a featureless portion of the Li film, acquired with a "fully loaded"/ "saturated" SLi-NPM tip. The red 'X' marks the spot for subsequent pipetting. b) NC-AFM topography image of the same planar region post pipetting revealing a Li mound located at the point the MWCNT contacted (-3V tip bias). Lithium field- migrated to the filled SLi-NPM tip, inducing mound formation.

These results are understood as MWCNT tip saturation. The above "transition" indicates the MWCNT has reached its Li capacity and cannot accommodate more Li. Under continued negative-tip-bias conditions, however, the electric field about the filled tip induces Li transport toward the MWCNT. As Li can no longer enter the MWCNT, lithium nucleates to form mounds. These mound features are

reminiscent of those observed during STM studies of tip-surface "jump to contact" phenomena and related nanoscale "neck" formations[90,91].

2.6 Lithium Mounds and Vacancy Islands Decay by Surface Diffusion

The Li structures generated by pipetting events with the SLi-NPM are kinetically unstable and decay in time. Using time-lapse NC-AFM measurements we monitored the pipette-induced vacancy islands (mounds) created by the SLi-NPM and their relaxation due to Li diffusion. Representative data of the decay of Li features as imaged by the SLi-NPM is displayed in Figure 12. The submicron-diameter voids in the Li film decay with characteristic lifetimes that depend on film thickness (Figure 12d-h). The films studied, four (two) Li layers, exhibited a decay time at room temperature of *ca.* 64 (289) minutes as shown in Figure 12h. This indicates diffusing Li interacts more strongly with the substrate at lower film thicknesses. The capability to directly track morphologic evolution of Li features (which have a convenient cylindrical symmetry) motivated the development of a model to simulate feature decay and quantify Li surface diffusion. Modeling details are described in section 2.11.

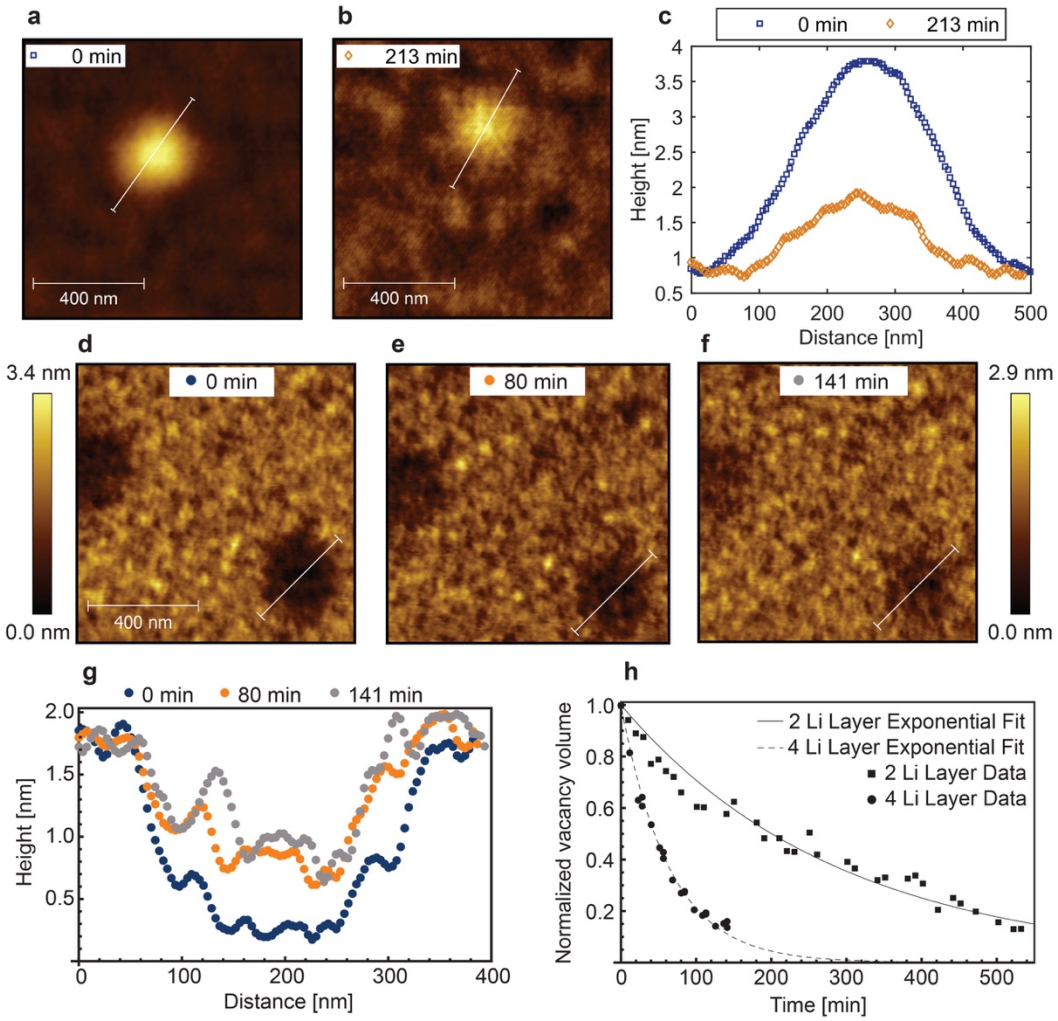

Figure 12: Lithium Surface Diffusion on Si(111) Electrode. a-b) Time-lapse NC-AFM measurements showing decay of a SLi-NPM-generated Li mound. c) Height cross-sections of mound displayed in (a) and (b). d-f) Time-lapse NC-AFM images showing decay of SLi-NPM-generated vacancy islands in a Li film, ~1.2 nm thick/four atomic layers, by means of lithium surface diffusion. g) Height cross-sections of the bottom right feature displayed in (d)-(f). Note that the apparent "noise" in the topographic cross-sections is actual topographic variation in the advancing lithium. h) Normalized vacancy island volume decay of features by surface diffusion for the two film thicknesses studied: ~.6 nm (two atomic layers) and ~1.2 nm (four atomic layers).

2.7 Physical Principles of Li-Nanopipetting

As shown above, the MWCNT tip is negatively (positively) biased by 3V with respect to the surface when transporting lithium to (from) the tip. This is consistent with the transfer of positively charged lithium (oxidizing before or

during transfer to the tip and reducing upon return). Utilization of the SLi-NPM as a Li-nanopipette relies on material properties, electrostatics, and film ionization to effect Li transfer. Below we consider in turn how the well-known lithiation properties of MWCNT materials, local electrostatics (analyzed with COMSOL Multiphysics – details given in Section 2.13), and lithium's ionizability support Li-nanopipetting.

2.8 Role of MWCNT in Li-Nanopipetting

Key to the Li-nanopipetting function of SLi-NPM is the open-ended MWCNT serving as the microscope tip. Pipetting attograms of Li is made possible by Li accommodation and transport in the MWCNT. When ionic Li comes in contact with a MWCNT, ions readily (and preferentially) insert into the tube through any tube openings and surface defects. Post insertion, Li ions intercalate the inter-tubular gaps, interstitial sites, and inner volume. This process, known as "electrochemical lithiation of carbon nanotubes," has been studied for >15 years and is supported by extensive experimentation[88,92-97] and modeling[98-107]. Nanopipetting of Li with the MWCNT tip is the systematic transfer of Li mass by electrochemical lithiation (de-lithiation): Li transport into (out of) the inter-tubular gaps, interstitial sites, and inner volume.

2.9 Electrostatics of Li-Nanopipetting: MWCNT-Tip Approach

In order to understand Li-ion transport for the biased-MWCNT in both tunneling range and in direct contact (see Fig. 2 Step 5 details), the charge state of Li in the Li film must be considered. Due to the low ionization potential of Li, some amount of electron charge is transferred to the Si substrate[108,109]. Bias application (Figure 8, Step 4) sets up a gradient in the electrostatic potential and a corresponding electric field. These quantities are displayed in Figure 13a for the case of a tip-film separation distance of Δ=3nm (see corresponding schematic Figure 13c) while the MWCNT is biased -3V relative to the film surface. Note that the electric field vectors overlaying the color-coded potential map are all normalized (for field direction visualization), and that due to cylindrical/azimuthal symmetry the electrostatics can be understood from two-dimensional cross-sections. In the electrostatic modeling, z now represents distance above the Li film surface, while Δ represents the tip-sample distance.

As the biased MWCNT-tip approaches the film, the electric field direction at the film surface, as in Figure 13a, is normal to and away from the surface for all $\Delta > 0$. For such noncontact geometries (all $\Delta > 0$), field lines originating at the film surface terminate into and normal to one of three MWCNT surfaces: the outer-most tube wall, the tube end, or the inner-most tube wall (as displayed in Figure 13a). For studying Li transport from the film to the tip, three relevant film regions arise: (I) within the tube inner radius ($-4.5\ nm < x < 4.5\ nm\ , z = 0$), (II) between the inner and outer tube radii ($4.5\ nm < |x| < 15\ nm\ , z = 0$), and (III) outside the tube ($|x| > 15\ nm\ , z = 0$). During tip approach, field lines originating

in region I (region II, region III) of the film terminate at the inner-most tube wall (tube end, outer-most tube wall).

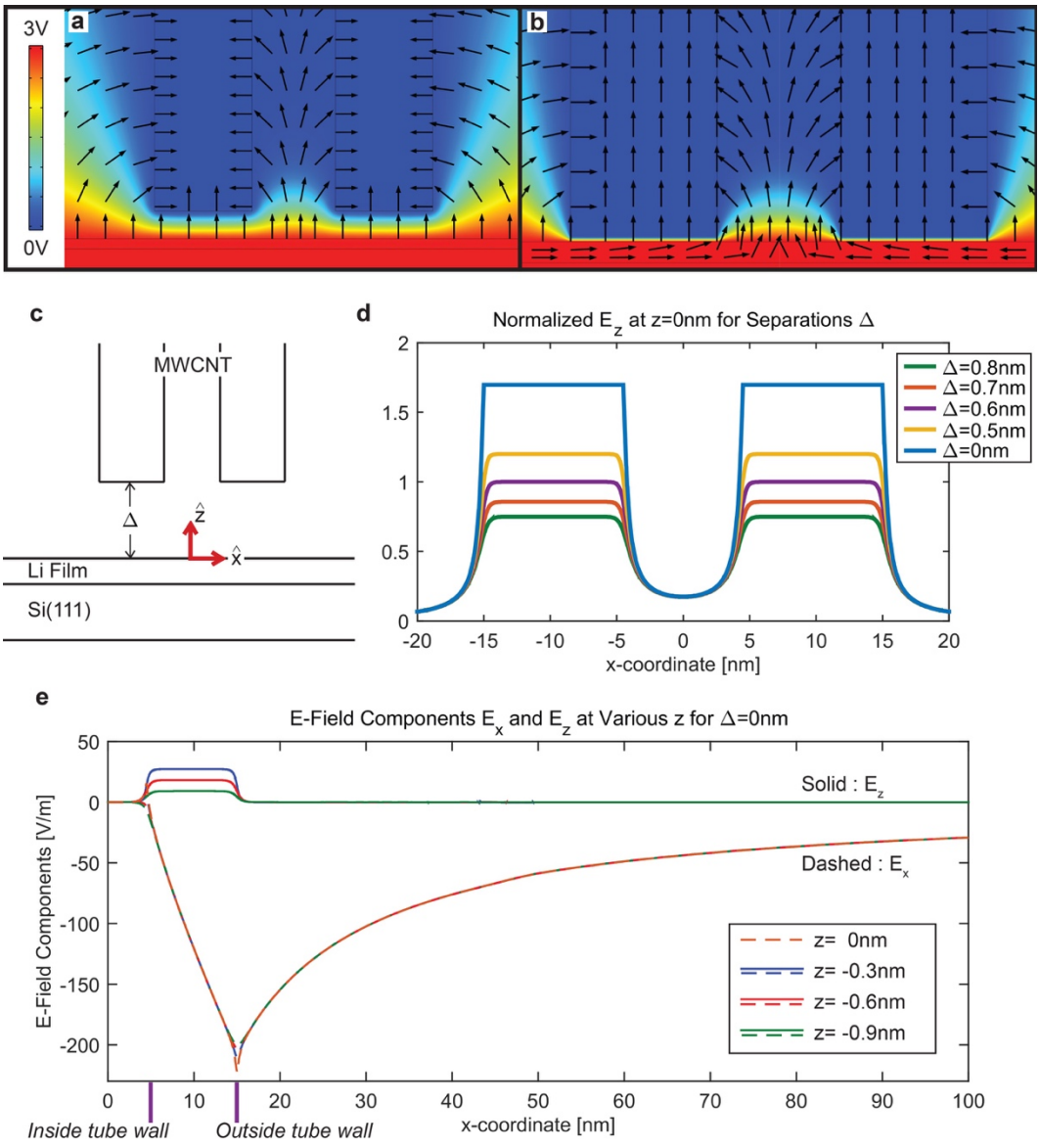

Figure 13: Electrostatics of Li-Nanopipetting. a-b) Cross-sections of the local electrostatic potential for tip-film separation distances of 3nm and 0nm respectively. Normalized electric field vectors are superimposed. Lithium ions experience an electrostatic force in the direction of these vectors. In both (a) and (b) the conductive cantilever is biased at -3V relative to the surface, matching the experimental conditions used to pipette Li from the surface to the MWCNT tip. c) Schematic of the cross-sectional geometry. The display of red unit vectors sets the coordinate system and origin for all modeling in Section 2.11. The tip-film separation distance is denoted by Δ. d) Electric field strength at the Li-film surface for various separation Δ (normalized to classical strength needed to ionize atomic Li). e) Electric field components for Δ=0. An electric field (pointing radially inward) penetrates the Li film for all radial distances outside the inner tube wall promoting planar Li field migration to the tip. Lithium under the tube walls or inner volume electrochemically intercalate the MWCNT and/or enter the tubes inner volume.

When the tip is not in contact, $\Delta > 0$, the strength of the electric field at the film surface, $E_z(x, z = 0; \Delta)$, in these three regions determines further film ionization and the possibility of field-induced Li transport. Partially ionized Li (from charge transfer), $Li^{0<q<1}$, at the film surface experiences an electrostatic force normal and away from the surface. Any ion removed from region I (region II, region III) will be transported to the inner-most tube wall (tube end, outer-most tube wall) according to the field lines. From the clear evidence of Li transfer, we know that sometime during nanopipetting the electric field is strong enough to overcome film bond energies (Li-Li and/or Li-Si) and transport Li ions to the MWCNT-tip.

Figure 13d shows $E_z(x, z = 0; \Delta)$, for various tip-sample distances Δ, normalized to the classical field strength needed to ionize atomic Li: $\sim 5 * 10^9\ V\ m^{-1}$. This classical ionization field strength was derived by simple energy arguments described elsewhere[110], and serves as an instructive upper bound for the local field strength that determines further ionization of Li at the film surface. As can be seen from Figure 13d, during the approach, the electric field at the film surface is always strongest in region II, followed by region I, then region III. For all $\Delta \leq 6$Å the field strength at the surface in region II equals or surpasses the classical field strength needed to ionize atomic Li. Consequently, during the approach any field-induced ion transport predominantly comes from Li originating in region II and would transfer to the tube end and in turn intercalate the intertubular gaps. Notwithstanding, any field-induced transfer from region I or region III during

approach would begin to decorate, respectively, the interior or exterior tube wall (with a greater concentration decorating the interior).

2.10 Electrostatics of Li-Nanopipetting: MWCNT-Tip / Film Contact

Under direct contact between the MWCNT-tip and the Li film ($\Delta = 0$) the electrostatic landscape changes significantly. As displayed in Figure 13b, the electric field permeates the interiors of the MWCNT as well as the Li film and Si substrate and the electric field vector alignment is modified. Another change is a shift in the Li transport mechanism to in-plane migration toward the tip and electrochemical lithiation of the MWCNT. As our nanopipetting is performed predominantly in contact mode, we further expand on Li transport during contact.

As noted above, under contact the electric field immediately permeates the entire Li film (Figure 13b). This is a substantive point in that the moment contact is made, any/all $Li^{0<q<1}$ ions comprising the film simultaneously experience a force from the electrostatic field. To better understand the electrostatics behind transport during contact, both components of $\vec{E}(x,z\,;\,\Delta=0) = E_x(x,z)\,\hat{x} + E_z(x,z)\,\hat{z}$ are plotted in Figure 13e for various values of z. All $E_x(x,z)$ are plotted as dashed curves while all $E_z(x,z)$ are plotted as solid curves. Plots corresponding to field components having the same z-value are color-matched. The plotted region of Figure 13e is $0\ nm \leq x \leq 100\ nm$, corresponding to the right half of Figures 2.7a, b, and c. However, from symmetry, the following results deduced from the data are identical for all cylindrical-coordinate radial values between 0 and 100 nm.

One of the most prominent features displayed in Figure 13e is the electric field in the negative x-direction that permeates the Li film for all z-values of the film. The corresponding electrostatic forces promote Li field migration radially inward toward the tube center (as seen in Figure 13b) and account for the present experimental observations of SLi-NPM-induced Li vacancy islands (Figures 2.3, 2.4 and 2.6). This electric force explains how the MWCNT-tips, when bias-actuated in contact to the film, readily generate Li vacancy islands with much larger diameters then their nominal 30nm diameter: Observed Li vacancy diameters ranged from 80nm-400nm. Both experimental observations and electrostatic simulations support in-plane field migration of Li.

Further analysis of local electrostatics provides insight on the destination of the field-migrating Li. While in-plane migration was discussed in the previous paragraph, Li upward migration to the MWCNT can also be understood from electrostatic considerations. Figure 13b and Figures 2.7d-e show that $Li^{0<q<1}$ ions comprising the film within the outer tube radius ($|x| \lesssim 15\,nm$), experience electrostatic forces in the positive z-direction toward the tube ends and inner volume. Any film vacancies will be quickly refilled via Li field migration radially inward or upward.

Electrostatic forces ultimately transport Li to the intertubular gaps, interstitial sites, or inner volume. Li outside the outer tube wall should either field migrate into the film under the tube end (Figure 13b and Figure 13e), or begin diffusing up the exterior tube wall (Figure 13d when $\Delta = 0$ and Figure 13e). Any Li transferred to the exterior tube wall will preferentially enter into the MWCNT

intertubular gaps through any surface defects[88,92-107]. This follows the electrostatic model displayed in Figure 13b: positively charged exterior wall Li experiences an electrostatic force into and normal to the wall. Li under the tube end will either electrochemically intercalate the intertubular gaps though any partial/full openings or defects[88,92-107] (Figure 13d-e) or field migrate into the film region directly below the inner volume (Figure 13b and Figure 13e). Finally, Li below the inner volume will be transferred to the interior tube walls and/or inner volume by electrostatic forces upward and/or surrounding high pressure film regions (Figure 13b and Figure 13d-e).

In this section, we have considered in detail the material properties and electrostatics that enable MWCNT-nanopipetting to produce vacancy islands in thin Li films. Additionally, as shown in Section 2.5, nanopipetting can also generate Li mounds in two very different ways. First, larger ~300nm diameter mounds are produced when the MWCNT is biased -3V relative to the sample after already having reached its Li capacity (Section 2.5 / Figure 11 and Figure 12a-b). In light of the above electrostatic considerations this makes sense. Upon contact Li would field migrate radially inward, but would be unable to intercalate the intertubular gaps or inner volume. Thus, the migrating Li would aggregate around the tube generating a mound with diameter larger than 30nm. The second way mounds were formed was by reducing the substrate to a lower electrostatic potential (-3V with respect to the tip) with a filled or partially filled MWCNT (Section 2.4 / Figure 10a-b / Figure 10f-g). In these cases, smaller 10-30 nm diameter mounds form. These can be understood from the above electrostatics by inverting all arrows

in Figure 13a and Figure 13b: Li intercalated into the intertubular gaps and inner volume are locally deposited.

2.11 Modeling Vacancy Island Decay by Surface Diffusion in Thin Films

As shown and discussed in section 2.6 the Li features (vacancy islands and mounds) produced by nanopipetting are kinetically unstable. The decay of these features provided an opportunity to obtain quantitative values for Li surface diffusion coefficients on the silicon substrates. A continuum model was developed to quantitate the decay of the pipette-generated vacancies. This required a general solution to the classical diffusion equation in cylindrical coordinates suitable for the vacancy island symmetry. This solution – or more properly the volume integral of the solution in the vacancy island region – was used to simulate the direct experimental measure of Li mass in the refilled void. With the surface diffusion coefficient D as the sole adjustable parameter in this model, experimental data of vacancy island volume in time, and an initial condition, is sufficient to determine D.

Our measurements (Figure 12) of the decay of Li vacancy islands illustrate chemical surface diffusion of Li: ad-Li surface diffusion driven by a gradient in chemical potential. Generally, this gradient in chemical potential is related to the gradient of adsorbate density to give Fick's first law[111]. Fick's first law, used in conjunction with the continuity equation, yields Fick's second law[112]. We here use this second law to model the ad-Li diffusion along the surface of the (7x7)-Si(111) substrate,

$$\frac{\partial \rho}{\partial t} = D\,\nabla^2 \rho \tag{2.1}$$

where ∇^2 is the Laplacian operator in cylindrical coordinates, D is the constant collective chemical surface diffusion coefficient (at room temperature), and ρ is the density of ad-Li.

"Density of ad-Li" is here defined as the Li mass within a volume element located at $(r, \emptyset)$, divided by the volume of the element: $\delta m/(r dr d\varphi\, h)$. (Note that h in the volume element is the height of the unaltered Li film.) This definition of "ad-particle density" is slightly different from the conventional definition of ad-atoms above an area element divided by the area element: $\delta N/(r dr d\varphi)$. However, the two are linked by multiplying the conventional definition by the constant ratio of Li atomic weight to h. This formulation was purposefully developed/chosen so that the boundary condition on ρ would be the known density of metallic Li.

Solving Equation (2.1) to simulate feature decay is greatly simplified by taking into account the symmetry and scale of the Li features. The Li vacancy islands have cylindrical/azimuthal symmetry and thus any derivatives with respect to φ in Equation (2.1) vanish. The typical vacancy island depth, $\sim .6 - 1.2\ nm$ is much smaller than the island diameter. We can thus treat the problem as two-dimensional (dependent on r and time) by removal of the z-dependence in Equation (2.1), reducing the diffusion equation to:

$$\frac{\partial \rho}{\partial t} = D \frac{1}{r} \frac{\partial}{\partial r}\left(r \frac{\partial \rho}{\partial r}\right) \tag{2.2}$$

where the ad-Li density ρ is a function of time and cylindrical coordinate r. A general solution (Appendix A) to the reduced diffusion equation (the "vacancy island diffusion equation"), Equation (2.2), obtained with separation of variables is:

$$\rho(r,t) = g + \sum_{n=1}^{\infty} A_n e^{-D\left(\frac{x_{0n}}{a}\right)^2 t} J_0\left(\frac{x_{0n}}{a} r\right) \tag{2.3}$$

with coefficients

$$A_n = \frac{2}{a^2 [J_1(x_{0n})]^2} \int_0^a J_0\left(\frac{x_{0n}}{a} \tilde{r}\right) [\rho_0(\tilde{r}) - g]\, \tilde{r}\ d\tilde{r} \tag{2.4}$$

where g is the known density of metallic Li, a is the radius of the Li vacancy island, ρ_0 is an initial condition for ad-Li density to be determined experimentally, J_0 and J_1 are the zero-order and first-order Bessel functions of the first kind, and x_{0n} is the nth zero of J_0. Equation (2.3) together with Equation (2.4) gives the general solution to the relevant diffusion equation, Equation (2.2). We emphasis that this solution is valid for all thin film vacancy island decay by surface diffusion having congruent symmetry and scale so long as parameters g, a, and ρ_0 are selected appropriately for the system being studied. See Appendix A for more details.

For theoretical consistency, it is essential to verify that an asymptotic analysis of the general solution (Equations (2.3) and (2.4)) is physically reasonable. There are three such limiting cases to consider here: time zero, large times, and when the radial coordinate is equal to the vacancy island radius. The latter two can be trivially seen to match the appropriate values by taking limits of Equation (2.3). Additionally, in the case of zero time, $\rho(r,0)$ needs to match the experimental initial condition, $\rho_0(r)$. This can be shown mathematically using Equations (2.3) and (2.4).

Obtaining the general solution to Equation (2.2) requires knowledge of the boundary condition $\rho(a,t) = g$ and initial condition $\rho(r,0) = \rho_0(r)$. The vacancy island radius a and density initial condition ρ_0 are obtained from the experimental data with a systematic method developed to precisely select the vacancy island features. Initial measurements (Figure 14a) show a featureless plane (unaltered Li film) and the vacancy island/s. Height statistics of the unaltered Li film (Figure 14b) reveal a normal distribution (Figure 14c). All height data pixels two standard deviations below the featureless plane mean height (unaltered Li film mean height denoted as h above) are identified as the vacancy island/s (Figure 14d). This process sets/determines the vacancy island radius a. (This process also allows precise vacancy island volume measurement via SPM software.) With the vacancy island established, a density initial condition can be found. For accurate determination, many height profiles of the initial circularly symmetric vacancy island are taken, all originating from the vacancy island center, and extending to the vacancy island boundary at various angles. The composite radial height taken

from these profiles is then scaled with height to give g at boundary $r = a$, giving ρ_0. In this way, the boundary and initial conditions can be quantitatively and reproducibly found from the experimental data.

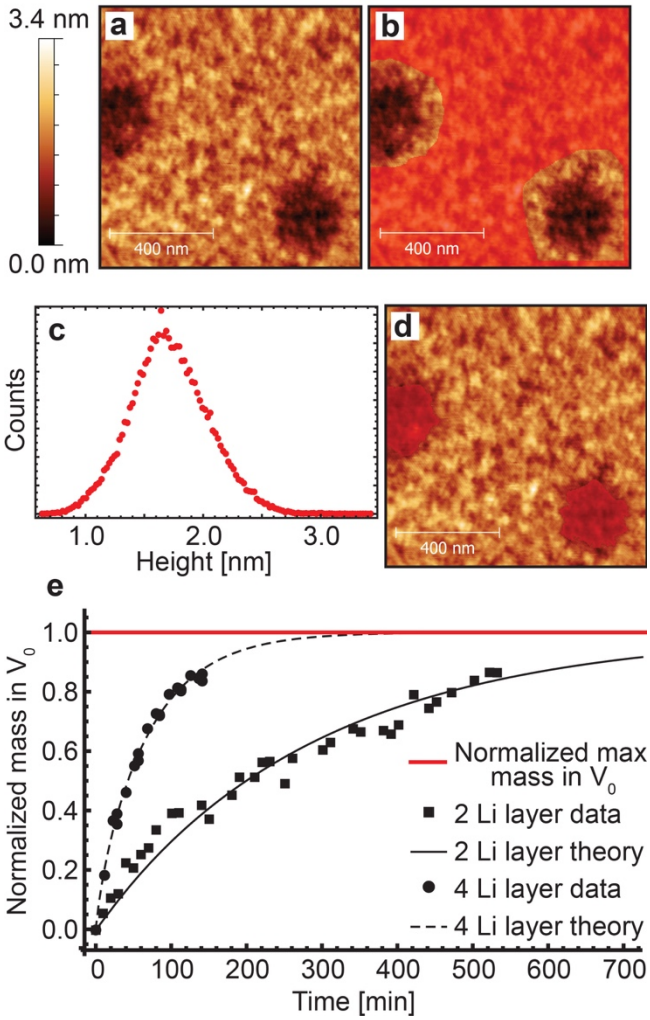

Figure 14: Method for determination of $'a'$ (vacancy island radius) and fitting the experimentally determined refilled and normalized Li mass with the theoretical model. a) Topography of SLi-NPM-induced vacancy islands. b) Highlighted in red, for height analysis, is a region of the bare Li film. c) Normal height distribution of the bare Li film highlighted in (b). d) Regions highlighted in red are large groupings of height values that are two standard deviations or more below the mean height of the film as determined from (c), and selected as vacancy island "features." e) Determination of D from the temporal decay of SLi-NPM-induced vacancy islands in two film thicknesses. Combined and normalized data is fit with the general solution to the reduced diffusion equation for vacancy island decay.

As shown in section 2.1, SLi-NPM lends itself to measuring the volume of Li vacancy islands as they decay in time. Using the known density for metallic Li, these volume measurements can be trivially related to the total amount of Li mass that has diffused into the vacancy island,

$$M_{V_0}^{Ex}(t) = [V_0 - V(t)]g \tag{2.5}$$

where V_0 is the initial vacancy island volume measured, $V(t)$ is the vacancy island volume in time, and $M_{V_0}^{Ex}(t)$ is the experimentally determined Li mass within V_0. Now the general solution to the reduced diffusion equation, Equation (2.3) and Equation (2.4), gives the density in a cylinder having radius and height commensurate with initial vacancy island radius and film height respectively. We refer to this cylindrical region as the "region of interest" (ROI). The general solution can be integrated over the ROI to provide the Li mass having refilled V_0 in the following way:

$$M_{V_0}^{Th}(t;D) = \int_{ROI} \rho(r,t;D)dv - \int_{ROI} \rho_0(r;D)dv \tag{2.6}$$

where $M_{V_0}^{Th}(t;D)$ is the Li mass within V_0 by theory with free parameter D. Equating Equation (2.5) and Equation (2.6) yields the expression used for simulating Li mass diffusion into the initial vacancy island volume with one free parameter: the room-temperature chemical surface diffusion coefficient D. A Mathematica[113] code for calculating D for any azimuthally symmetric vacancy

island decay in thin films by chemical surface diffusion, using the above method, was written (the code can be viewed in Appendix B).

Using this method of simulation, the room temperature value for D for Li on Si(111) was determined for the two most common film thickness deposited. Not unexpectedly, D varied with film thickness: for ~1.2 nm (four atomic layers) $D = 8\ (\pm 1.2) * 10^{-15}$ cm^2 s^{-1} and for ~.6 nm (two atomic layers) $D = 1.75\ (\pm .15) * 10^{-15}$ cm^2 s^{-1}. Both intervals given here for D are 99% confidence intervals. The combined multi-feature diffusion data and theory, $M_{V_0}^{Ex}(t)$ and $M_{V_0}^{Th}(t; D)$, for both film thicknesses are displayed in Figure 14e and normalized to the maximum Li mass capable of diffusing into a given V_0. The reduction in D with decreasing film thickness can be understood in that the thinner the film, the more diffusing Li interacts with the corrugated Si(111) surface, reducing D. We note that this is the first report of D for Li on a Si substrate, providing a key transport parameter for Li on a Si anode. Determination of D for Li on other Si orientations and energy storage material substrates is of significant interest, and may be accomplished by extending SLi-NPM to these systems.

2.12 Conclusions

We have shown that SNPM, a nanotechnology/technique first suggested over ten years ago, can be accomplished when the CNT-pipetted material is Li and the protocols detailed herein are followed. This was demonstrated by using an open-ended MWCNT (appended to the tip of a conductive SPM cantilever) as a multi-functioning MWCNT-nanopipette and SPM probe for Li: SLi-NPM. By

controlling bias, separation distance, and contact time Li mass (volume) ranging from 10^{-2} ag to 10's of ag (100's of nm^3 to 10,000's of nm^3) was reproducibly transferred between a Li/Si (111) surface and the MWCNT with nm planar precision. Voids in the Li film (by pipetting with a negative tip bias) and Li mounds (by pipetting with a positive tip bias) were readily generated and measured with SLi-NPM. The MWCNT's used in this study, *ca.* 1 micron length x 30 nm diameter, became saturated after sequential Li withdrawals, demonstrating a Li capacity on the order of 10^5 nm^3. Transfer of Li to the silicon surface was accomplished with both a filled or partially filled MWCNT tip. The electrostatics of MWCNT-nanopipetting by SLi-NPM were modeled, as a guide to interpret the electrostatic mechanisms behind Li mass transfer.

The SLi-NPM MWCNT tip conveniently also serves as a conductive SPM probe, permitting observation of the dynamics of Li surface features. A continuum model generally applicable for thin film vacancy island decay of cylindrically symmetric voids by surface diffusion was developed. This model was used to describe the decay of cylindrically symmetric voids in Li films of two thicknesses: .6 nm and 1.2 nm (two and four Li layers respectively). The Li surface diffusion parameter on the silicon anode substrate in both cases was quantified for the first time. A reduction in the diffusion coefficient with decreasing film thickness from four to two Li layers was measured due to increased Li/surface interaction: respectively, $D = 8\ (\pm 1.2) * 10^{-15}\ cm^2\ s^{-1}$ and $D = 1.75\ (\pm .15) * 10^{-15}\ cm^2\ s^{-1}$ with 99% confidence at room temperature. SLi-NPM represents a solid-state electrochemical nanocell during pipetting operation, and provides an enabling

nanotechnology/technique for future studies of fundamental importance to basic energy storage research such as nanoelectrode characterization and controlled nanoelectrode lithiation and de-lithiation.

2.13 Experimental Details

Silicon Substrate Preparation. All 7x1 mm^2 samples were cleaved from a Si (111) wafer (Electro-Optic Materials, resistivity < .1 Ohm-cm). Samples were transferred into a UHV environment and flash annealed to 1150 ^{0}C through resistive heating. The samples were then cooled to room temperature under UHV with protocols (quickly to 900 ^{0}C, then slowly to room temperature) to create well-ordered Si(111) surfaces with the desired 7x7 reconstruction, as confirmed by UHV STM using a tungsten or platinum-iridium tip.

*Lithium Film Deposition***.** A Li getter source (SAES Getters catalog code LI/NF/0.85/17 FT10+10) positioned *ca.* 7 cm from the surface was used to deposit atomic Li at room temperature under UHV conditions onto the (7x7)-Si(111) substrate. Typical getter deposition temperatures were approximately 706 ^{0}C, as monitored by a thermocouple directly attached to the getter. Lithium deposition times ranged from two to four minutes. This method for Li film deposition has been previously used by others to generate Li films on crystalline Si(111) - (7 X 7) with coverages ranging from sub-monolayer to multilayer[114,115]. At coverages on the order of 0.01 monolayer, alkali metals[109], including Li[116], form small clusters on Si(111)-(7x7). With increasing coverage, cluster size (diameter) grows[116], eventually leading to multilayer Li films on crystalline Si(111) - (7 X

7)[114] in UHV. In the present work control experiments using Auger electron spectroscopy confirmed deposition amounts needed for multilayer Li. The Auger spectrum displayed the characteristic ~50 eV peak indicating the presence of metallic Li (two or more layers), as opposed to a peak at ~42eV that would indicate less than a monolayer of Li coverage[117,118]. The thickness of the Li film was determined from the depth of the SLi-NPM pipette-induced voids in the films and corroborated with Li flux measurements performed in our laboratory.

*Scanning Lithium-Nanopipette and Probe Cantilever & Tip***.** Probes used in our experiments consisted of an open-ended MWCNT attached to the terminus of a conductive AFM cantilever and were custom-made for our experiments by Carbon Design Innovations (CDI). The MWCNTs were grown by chemical vapor deposition (CVD)[119], a growth method known to produce open-ended MWCNTS[120]. The nominal dimensions of the CVD-grown MWCNTs were 1 μm long and 30nm in diameter. The tubes were then attached to the end of a conductive, non-contact atomic force microscope cantilever (APPNANO Model: ANSCM-PA; f=300 kHz, k=40 N/m) with a proprietary technique. Post attachment the MWCNTs were straightened with a patented alignment process called "Ion Flux Molding"[121,122]. The tube-shafts were reinforced with a platinum coating leaving < 250nm of the MWCNT-tip exposed at the tube's apex. This process increases tip rigidity and gives the tips the tapered appearance seen in Figure 7c (SEM image provided by CDI). Prior to SPM measurements, probe tips were additionally treated in situ by field emission (10-70 V, ~1μA) to clear any potential end contaminants and discharge any content.

Current Threshold for STM Tip – Sample Contact. Control experiments were performed in which conventional STM tips (both Tungsten and Platinum-Iridium) were made to approach a sample surface while monitoring current. Once current surpassed 10 nA mechanical contact had been made between the tip and sample as evidenced by tip deformation measured with SEM. This tip-sample contact current threshold has been observed in other STM experiments[123]. Thus a current threshold of 10 nA was used to determine when the SLi-NPM MWCNT tip had made contact with the surface.

Modeling Electrostatics of Nanopipetting. COMSOL Multiphysics was used to simulate the local electrostatic potential and electric field under pipetting conditions. Numerical solutions to the Continuity equation (current conservation) and Laplace equation, based on Ohms' Law, were found with finite element analysis for a range of tip-sample separation distances (electric potential boundary conditions matched those of our experiments). The simulations took into account the relevant material properties of the MWCNT, thin Li film, and supporting Si(111) substrate. For simulations of tip-film contact, a contact resistance of 2.97 MΩ was used by placing a 3.5 Å thick (sum of Li and C van der Waals radii) resistive material between the tip and film surface. The MWCNT was treated as a conducting cylindrical shell of inner radius 4.5nm and outer radius 15nm (congruent with the nominal dimensions of our MWCNT tips). The geometry of the tip/sample system possesses azimuthal/cylindrical symmetry about the MWCNT cylinder axis resulting in a simplification of the problem eliminating all azimuthal angular dependence. Thus the problem was solved using 2D

axisymmetric coordinates (r,z). Cross-sections of the electrostatic potential, current density, and electric field were all determined in this way.

Chapter 3: Pascalammetry with Operando Microbattery Probes

Acknowledgment: This work is prepared for submission for journal publication. Authors who participated in the work, with associations held at the time, are:

Jonathan M. Larson[1] (J.M.L.)*, Eleanor Gillette*[2] (E.G.)*, Kristen Burson*[1] (K.B.)*, Yilin Wang* [1](Y.W.)*, Sang Bok Lee*[2] (S.B.L.)*, and Janice E. Reutt-Robey*[2] (J.E.R.-R.)

University of Maryland Department of [1]Physics, [2]Chemistry and Biochemistry

J.M.L., E.G., S.B.L., and J.E.R-R developed the initial idea to create probe tips clad with metallic lithium for SPM [82]studies of local lithiation. J.M.L. and E.G collaborated to fabricate probe tips. J.M.L, K.B. and Y.L. discussed and conducted methods of tip transfer to UHV and prepared and characterized Si cathode substrates. J.M.L. and K.B. conducted initial exploratory SPM experiments. J.M.L. discovered increased pressure on operando microbatteries induced current transients. He planned and performed specific SPM experiments to test these effects and develop pascalammetry measurements. J.M.L. developed the diffusion/activation theory for stress-assisted diffusion – the analytical framework to quantify pascalammetry data. J.M.L. analyzed all data, generated all figures, and wrote the paper. The paper was then edited and refined by all authors. All authors discussed the results and implications.

3.1 Introduction

Advancements in energy storage research will affect the future of mankind and the environment. While there has been decades-long progress in the development of energy storage solutions for portable electronic devices, major hurdles persist for grid-scale energy storage and for safe vehicular batteries. To address these challenges, the research community is pursuing innovative storage concepts[13,14], chemistries[16-18], electrolytes[19-21], interfacial layerings[22-24], and geometries[25-27]. To realize these innovations, techniques are needed to characterize charge-transport phenomena over a range of scales and material conditions.

One condition of particular concern in rechargeable batteries is that of mechanical stress. High stress within battery systems is common – caused by electrode swelling/volume change[124,125], gaseous byproducts of side reactions[126,127], and/or ionic diffusion[128,129]. Stress can eventually lead to performance loss, degradation, and failure. A better physical understanding of ion transport dynamics through stressed battery materials would enable the early sensing of stress and its deleterious consequences, and enable effective mitigation strategies.

In non-stressed electrochemical systems, ion transport dynamics obey the classic Cottrell equation[130-132]. This analytical solution of Fick's second law in one dimension leads to a convenient expression for diffusion-limited current. The Cottrell equation predicts that diffusion-limited current decays as time$^{-1/2}$ [130-

132], and has been widely confirmed and utilized. However, as early as 1948, it was reported that this equation would need to be altered for stressed systems[133].

In the following decades, rigorous mathematical treatments of stress-assisted diffusion (SAD) were developed[134-137]. SAD is broadly defined here as any physical situation in which stress non-negligibly affects the diffusional behavior of active species within an electrochemical system. In cases of SAD, ion transport dynamics and concentration profiles cannot be adequately described by the conventional Cottrell formalism. Recently, SAD modeling has been extended to energy storage applications[138-141]. While these formulations are fundamentally important, and precise, they can include coupling terms, tensors, or non-linear terms, and are typically not tractable for most experimental systems.

Nevertheless, possible deviation from Cottrellian behavior through SAD is intriguing in light of the needs to understand and sense high stress, and its impact on operando energy storage devices. If a specific signal for SAD could be discovered in highly stressed solid electrolytes, that signal could be used to identify the onset of high levels of stress and, thus, the threat of impending degradation or failure. In the following, we describe the development of pascalammetry, a novel electrochemical/mechanical technique we invented to study stress-related phenomena in electrochemical systems. We also present the first application of pascalammetry, here used for controlled study of SAD. Additionally, we report a convenient framework for the detection and quantitative analysis of SAD, providing unique opportunity to measure stress-induced degradation in solid-state batteries.

3.2 Development of Pascalammetry

To develop this new pascalammetry technique, we draw direction from voltammetry. In voltammetry, a voltage waveform is applied to an electrochemical system, and induced currents are measured and analyzed[132]. In pascalammetry, a stress waveform is applied to an electrochemical system – at constant chemical potential difference (bias voltage) – and induced currents are measured and analyzed. While conventional electrochemistry has been done at various static pressures in the past[142], pascalammetry is altogether different, relying on gross dynamic stresses to induce faradaic current responses in electrochemical systems for quantitative analyses.

The electrochemical system used to demonstrate this pascalammetry technique, and study SAD, is a microscopic version of a full cell, solid-state battery depicted in Figure 15A. Experiments utilize a JEOL JSPM-4500A ultra-high vacuum (UHV), multifunctional scanning probe microscope (SPM), with in situ scanning electron microscope (SEM). The microbattery consists of a microscale half-cell probe (microbattery probe) in contact with an oxide-free silicon electrode (Figure 15B) as described in Appendix D. For the half-cell probe, a blunted W scanning tunneling microscope tip functions as a current collector, an ca. 10 μm Li metal film coated on the tip functions as the anode, and the ca. 1 μm lithium oxide terminal coating on the Li metal film functions as the solid-state electrolyte. Probe tip geometry and materials are chosen to facilitate pascalammetry measurements; see Appendix D for further details.

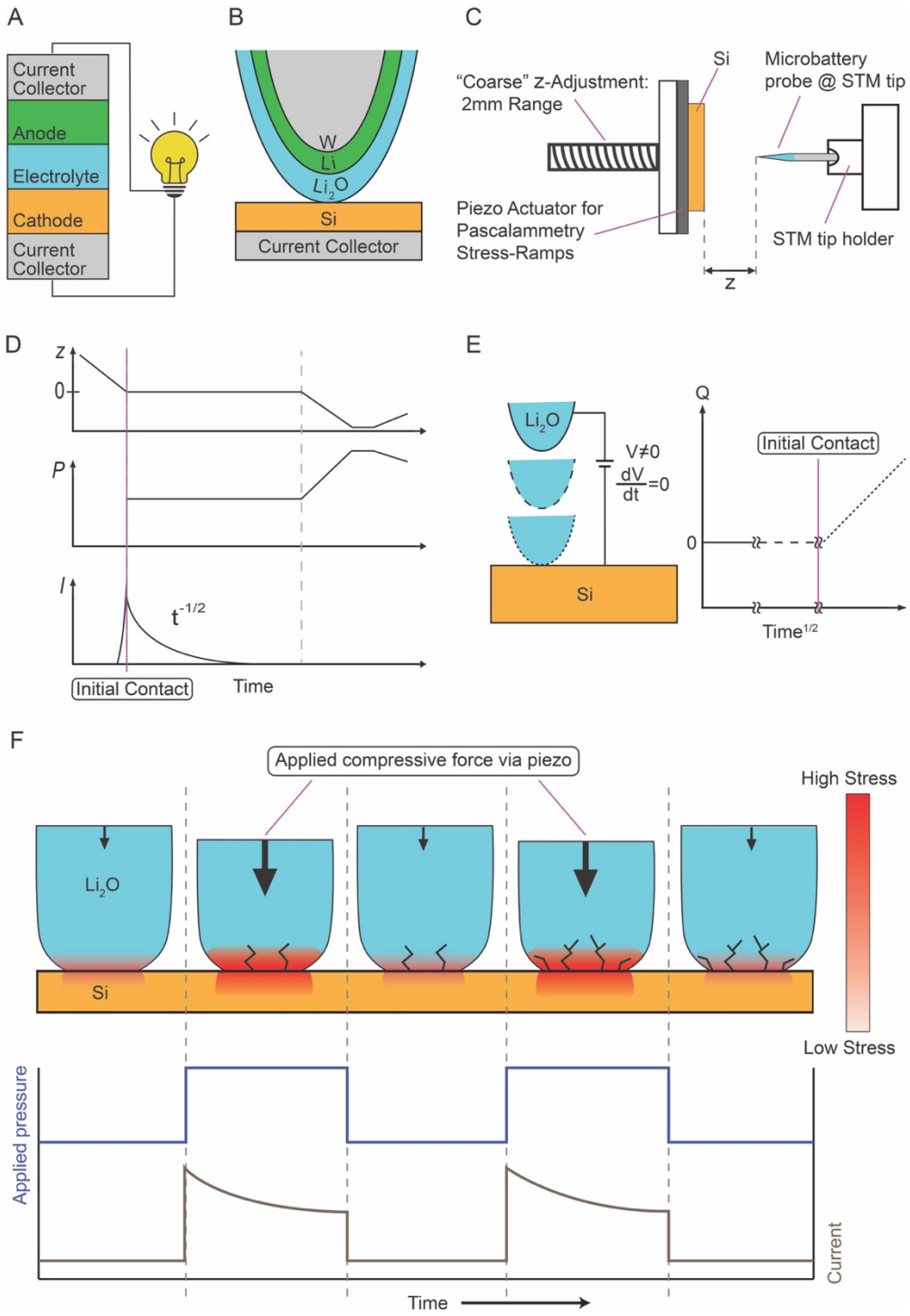

Figure 15: (A) Schematic of a solid-state battery (B) Schematic of the solid-state microbattery, consisting of a microbattery probe in contact with a Si-cathode. (C) Scan-probe experimental geometry. (D) Microbattery probe approach, contact, and validation protocols prior to pascalammetry measurements. (E) Schematic close-up of biased microbattery probe approaching the counter electrode. Solid, dashed, and dotted outlines, and adjacent charge vs time$^{1/2}$ plot, correspond to different times with respect to the approach and initial contact. (pre-pascalammetry). (F) Illustration of two sequential pascalammetry measurements. Applied compressive forces, induced faradaic current transients, and mechanical degradation (cracking of the electrolyte coating) are depicted.

A full-cell solid-state microbattery is established using a "coarse" motor to reduce the separation distance 'z' between microbattery probe and Si(111) cathode until mechanical contact is made (Figure 15C). During this approach, a constant charging bias condition of -2.0V Si relative to Li is applied. Mechanical contact is evidenced by a sudden increase in current, at which point the mechanical motor is disengaged, a point called "initial contact" (Figure 15D). This point of mechanical contact is equivalent to a potential-step voltammetry experiment in that the biased circuit is open until contact is made. The current subsequently decays as $time^{-1/2}$, according to the Cottrell equation, with any capacitive effects disappearing in <0.5s, see Appendix D for further details. The microbattery current eventually decays to a steady state value below our measurement limit (Figure 15D), indicating electronic (ionic) contribution to the current signal by leakage (migration) is negligibly small. All these findings demonstrate measured current upon initial mechanical contact is faradaic and limited by ion diffusion through the minimally stressed lithium oxide electrolyte. Figure 15E provides another graphical representation of the approach and initial contact. The solid, dashed, and dotted outlines of the microbattery represent different times (separation distances) and correspond to the plot of charge Q vs $time^{1/2}$, where Q is the time-integrated current.

After the diffusion-limited faradaic current reaches a steady state, we slowly increase the pressure at constant voltage, such that there is no increase in current or observable morphological change (Figure 15D time values to the right of the dashed vertical line). This establishes a more stable junction for subsequent measurements. Note that $z<0$ corresponds to application of compressive forces on the microbattery,

as the ½-cell probe with contact area of ca. $2{,}000\ \mu m^2$ cannot penetrate the Si cathode. After establishing this stable contact, we proceed with pascalammetry measurements in sets of stress ramps (P-sets). During a given P-set, the chemical potential difference (bias voltage) is kept constant to suppresses possible interfacial capacitive charge transfer due to changes in voltage. Figure 15F schematically illustrates a P-set with two successive stress ramps, in which black arrows represent applied compressive forces, red color gradients represent qualitative stress fields, and the resulting cracks correspond to mechanical degradation.

3.3 Application of Pascalammetry

As described above, once a stable junction is established, pascalammetry experiments are conducted. Figure 16 displays representative data in a top-to-bottom chronological timeline. In situ SEM measurements before/after P-sets are color-coded to match materials in Figure 15. The gray area in the SEM data is an exposed region of the core W tip, proving a convenient gauge for the thickness of the coating materials. The first SEM image in Figure 16 is obtained after stable contact is established, and prior to pascalammetry measurements. Three examples of pascalammetry measurements are presented on Figure 16 (right side). For clarity, currents are displayed with a third order Gaussian filter, while all analyses utilize raw data. During a stress step pascalammetry experiment, compressive stresses to the lithium oxide electrolyte are applied with a piezo actuator, and are limited to a maximal value of ca. 800 MPa as described in Appendix D. All "pressure" signals in Figure 16 refer to the stress in the electrolyte, and are

normalized to one, corresponding to the limiting stress value. We find pascalammetry measurements on our operando device cause faradaic current transients attributable to SAD, as well as degradation.

Mechanical degradation is evident by comparison of SEM data before and after the pascalammetry measurements. Arrows indicate obvious cracking locations in the middle SEM image. Following multiple stress ramps and retraction

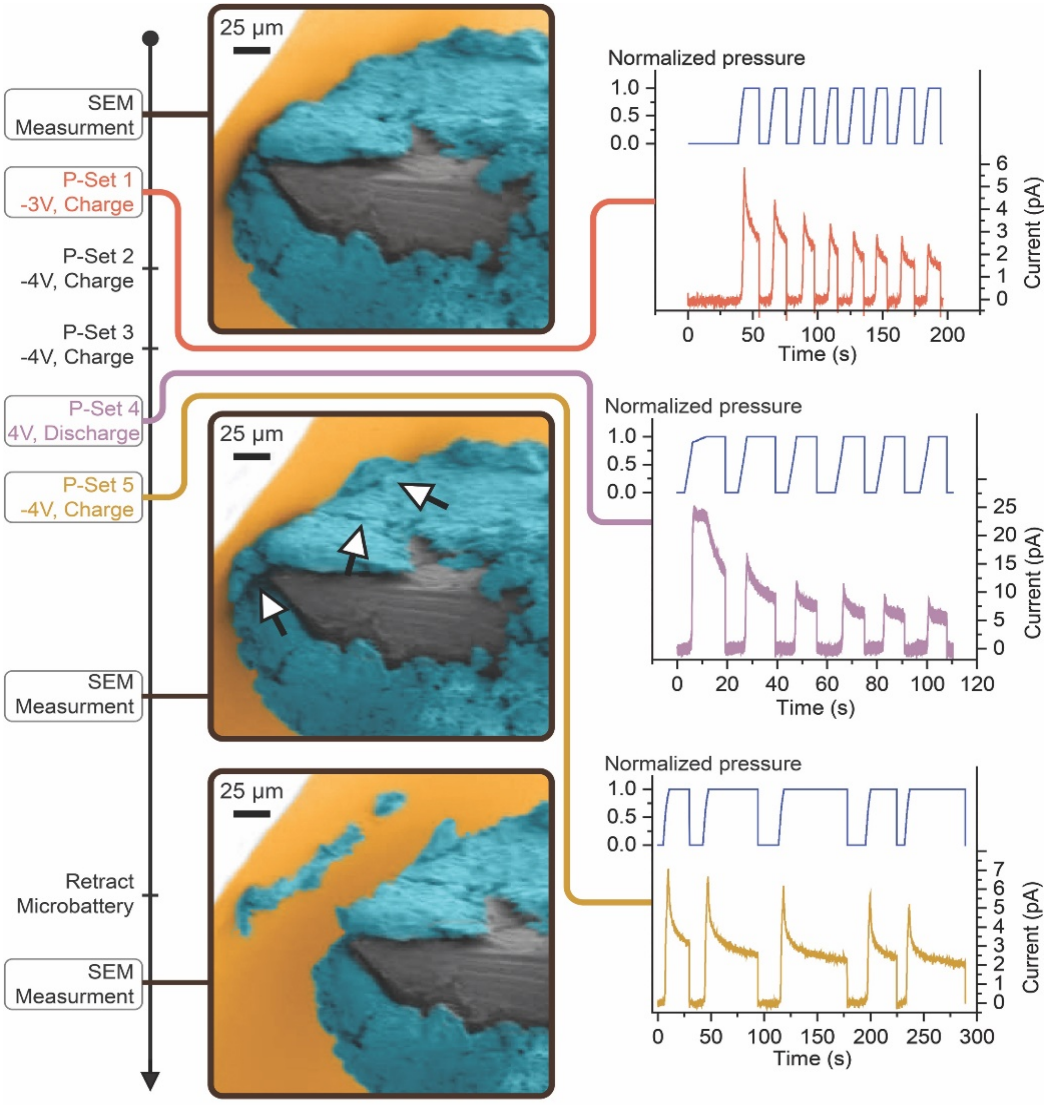

Figure 16: The left-hand timeline provides a chronology of the pascalammetry measurements and interleaved SEM imaging. SEM images are displayed center and color-matched to Figure 15, while representative pascalammetry data sets (P-sets) for charging and discharging are plotted at right.

of the microbattery probe (bottom SEM), the electrolyte is found to have fractured: the applied stresses (upper bound of ca. 800 MPa) are sufficient to cause mechanical degradation of the lithium oxide electrolyte. Thus, the electrolyte stress value is ideal to study signatures of SAD in solid electrolytes experiencing mechanical degradation.

While stress ramps from pascalammetry experiments induce current transients (Figure 16), it is important to distinguish between faradaic and capacitive effects. Generally, changes in voltage or contact area change the capacitance, and induce capacitive charging or discharging. All pascalammetry stress-step measurements are conducted at constant bias voltage to avoid such capacitive charging. We utilize large contact areas ($2{,}000\ \mu m^2$) and non-ductile electrolytes so that relative changes in contact area are negligible. Moreover, while capacitance is linearly proportional to contact area, the time constant for capacitive charging/discharging does not depend on the contact area (see Appendix D). Therefore, if slight contact areal changes occur in sync with a stress step, capacitive charging/discharging contributions to measured current will vanish in less than 0.5s, as described above, and in Appendix D. We thus confirm that measured stress-induced current transients are faradaic in nature.

3.4 Analyses of Pascalammetry Data

Analysis of the 27 faradaic current transients arising from stress ramps in pascalammetry measurements confirms the prediction of Cottrell and others – stress can induce currents that cannot be described with the Cottrell equation, namely, stress can induce SAD. In Figure 17A (17B) we plot charge versus time (square-root time) for initial non-stressed contact in black and representative pascalammetry measurement in red. Because the Cottrell equation predicts a

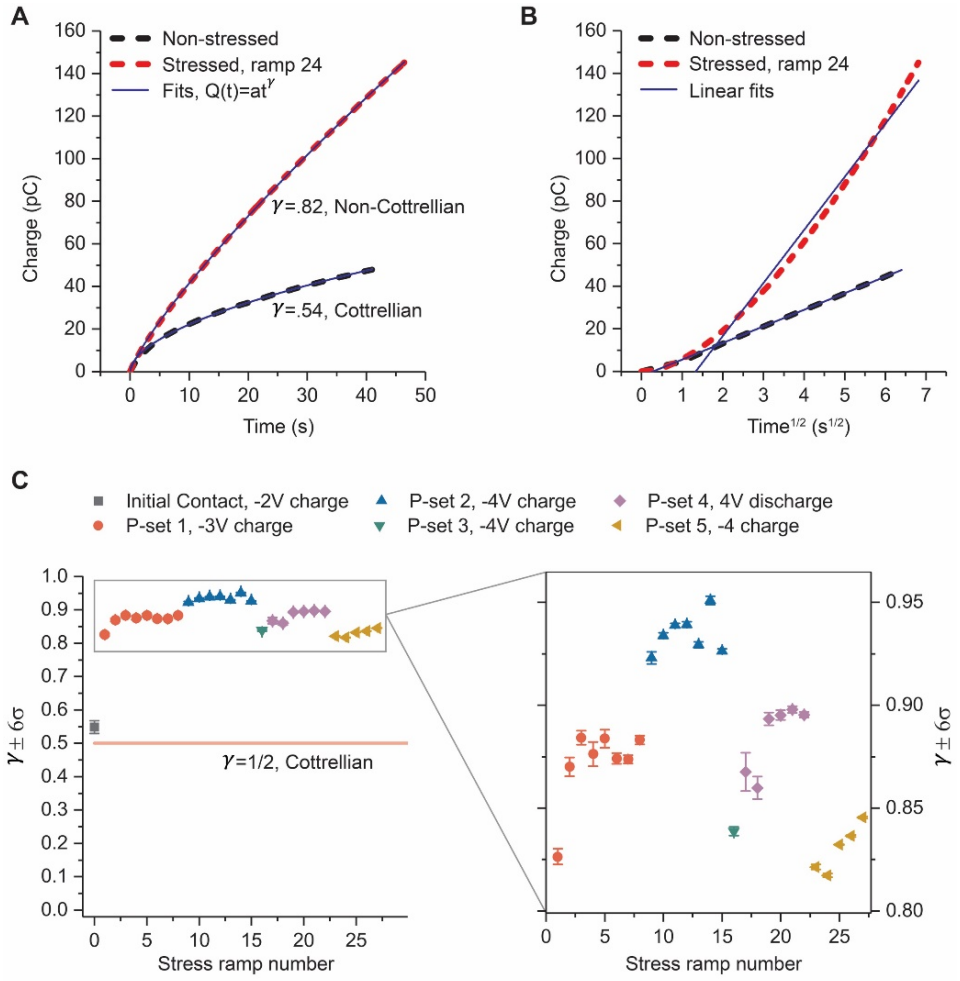

Figure 17: (A) Time integrated current plotted versus time for initial contact and representative stress ramp. Power law fitting (blue traces) demonstrates the non-stressed microbattery follows the time dependence of the Cottrell equation, while the stressed microbattery deviates. (B) Plots of the same data from Figure 17A versus time$^{1/2}$, with linear fits overlaid (blue traces). (C) Plot of the fitting parameter γ ($\pm$ 6σ) for non-stressed initial contact and all pascalammetry measurements.

functional form for charge versus time to be $Q=at^{1/2}$, plots in Figure 17A (17B) are overlaid with appropriate power-law (linear) fits in blue. Initial non-stressed measurements clearly follow the Cottrell equation, whereas the stressed measurements cannot be properly fit with a functional form of $Q=at^{1/2}$. This is emphasized by plotting the power-law fitting parameter γ for all pascalammetry measurements, where the power law is $Q=at^{\gamma}$ (Figure 17C).

Figure 17C demonstrates that regardless of the sign of the cell voltage (charging or discharging), all SAD faradaic current transients exhibit similar non-Cottrellian time dependence: $0.5 < \gamma < 1$. This measured range for gamma is distinct from a more-common deviation from the Cottrell equation (Figure 18): diffusion with a driving force, which evolves in a similar manner to a time-dependence of $0 < \gamma < 0.5$ as shown in Figure 19. Due to our findings that $0.5 < \gamma < 1$ in all pascalammetry measurements, without exception, we propose this time evolution as a signature for SAD. Next, a concise theory will be presented to describe this time evolution. For convention, $t = 0$s is chosen as the point in time in which peak SAD current occurs, just before non-Cottrellian decay begins.

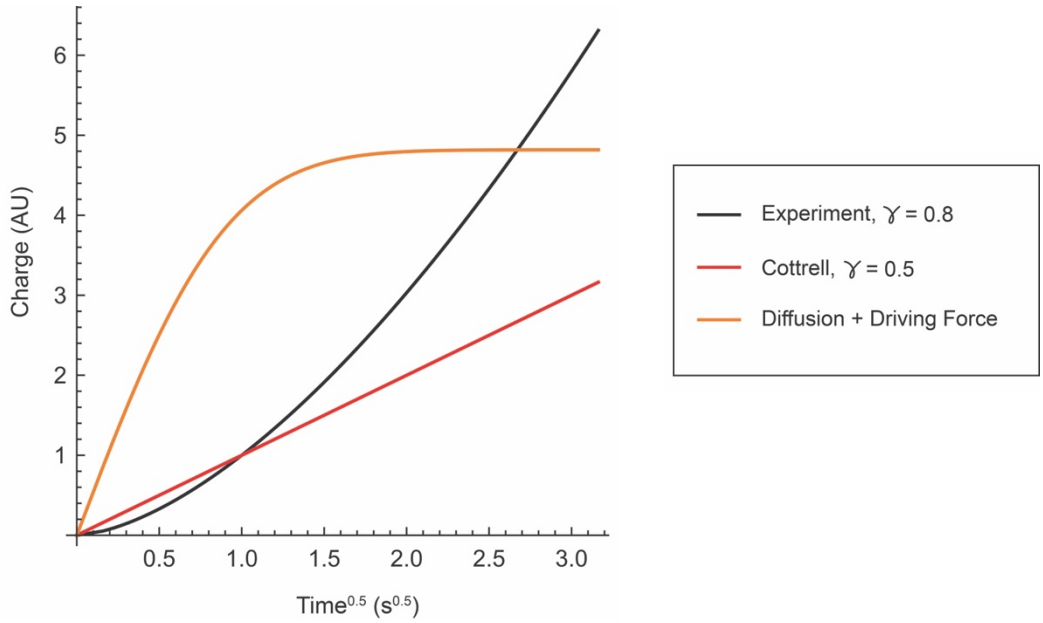

Figure 18: Charge vs. square-root time for experiment, Cottrell, and diffusion + driving force.

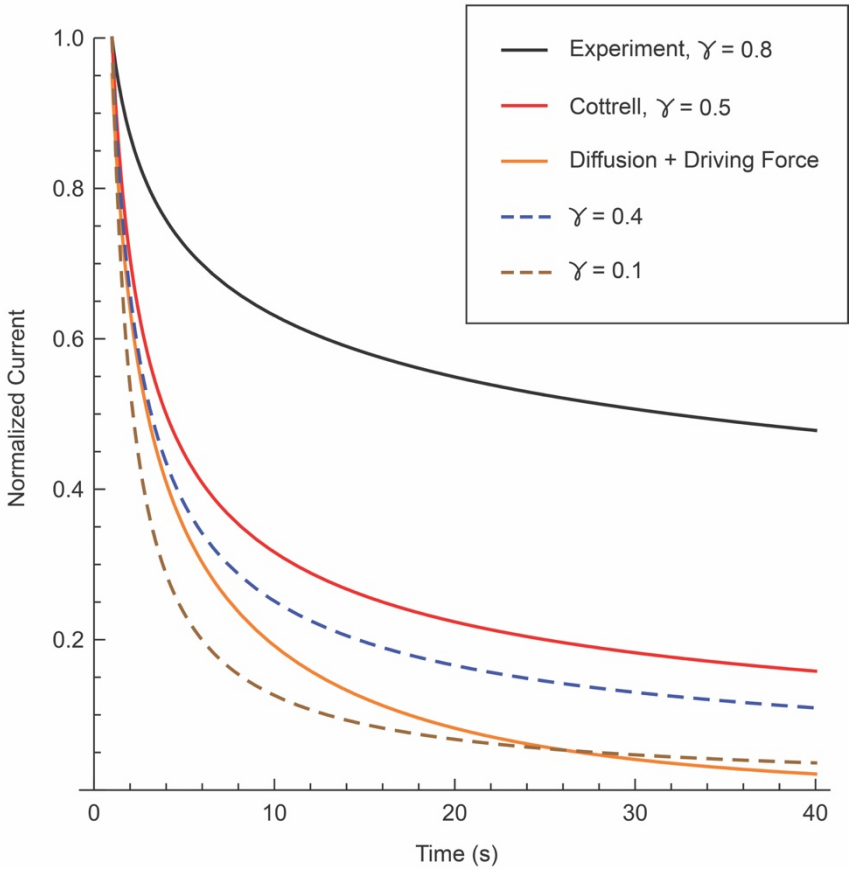

Figure 19 Normalized current vs. time for various values of fitting parameter γ

3.5 SAD Modeling

To account for complex stress affects during SAD, we adopt a time-dependent diffusion coefficient and introduce an activation/source term (Appendix C), as shown in Equation (3.1). We call the resulting approach the "diffusion activation theory" (DAT) for SAD.

$$\frac{\partial}{\partial t} C(x,t) = D(t)\, \nabla^2 C(x,t) + \Sigma(x,t) \tag{3.1}$$

In Equation (3.1), $D(t)$ is the stress-assisted, time-dependent diffusion coefficient, $C(x,t)$ is the concentration of an "active" chemical species (here Li^+) with sufficient energy and a pathway to diffuse. Within this picture, only a fraction of the stoichiometric concentration of a chemical species within a solid electrolyte is active. If energy and/or defects are added to the electrolyte, through increased stress imparted by an external force or a volumetric expansion of an electrode, inactive species may be activated. This process cannot be accounted for by a diffusional mechanism and is addressed mathematically by the inclusion of an activation (source) term $\Sigma(x,t)$ in Equation (3.1).

We choose $\Sigma(x,t)$ to have linear proportionality, η, to the time derivative of the concentration. This simplification is sometimes used in diffusion problems with local chemical reactions[143], and avoids a non-linear term in the differential equation. The proportionality constant η must range between $0 \leq \eta < 1$: Physically, η represents the time and space averaged percentage of the rate of change in

concentration attributable to activation of inactive species. The result in one dimension is a "diffusion/activation equation:"

$$\frac{\partial}{\partial t}\, C(x,t) = \frac{D(t)}{1-\eta}\, \frac{\partial^2}{\partial x^2}\, C(x,t) \tag{3.2}$$

The diffusion/activation equation is solved (Appendix C) for the finite length of the electrolyte and the finite duration of SAD. The analytical solution, cast as a function of dimensionless time $\tau \equiv \frac{t}{1s}$, is

$$C(x,\tau) = C^* \left(1 + \frac{\mathcal{D}_0 k^2 [(\tau+1)^\gamma - 1]}{\gamma(1-\eta)}\right) \frac{\sinh(kx)}{\sinh(kL)} \tag{3.3}$$

where L, $\mathcal{D}_0$, C^*, and k are the length of the electrolyte, the initial stress-assisted diffusion coefficient multiplied by one second, the initial concentration at oxidation interface, and a positive constant, respectively. The parameter η relates to latent species activation as described before. The parameter γ defines the power-law of charge evolution and relates physically to stress-effects, including activation, over the time interval being studied. Additionally, the time-dependent diffusion coefficient reads

$$D(\tau) = \frac{D_0 (\tau+1)^{\gamma-1}\, \gamma(1-\eta)}{\mathcal{D}_0 k^2 [(\tau+1)^\gamma - 1] \, + \gamma(1-\eta)} \tag{3.4}$$

which decreases in time, and D_0 is the initial stress-assisted diffusion constant. The resulting expression for SAD current, as predicted by the DAT, can thus be written:

$$I_{\mathrm{SAD}}(\tau) = \frac{nFAC^{*}D_0}{\mathcal{L}\,(\tau+1)^{1-\gamma}} \tag{3.5}$$

In Equation (3.5), the structure of $\mathrm{I}_{\mathrm{SAD}}(t)$ resembles that of the well-known Cottrell Equation – $nFAC^{*}\sqrt{D}/(\pi t)^{1/2}$ – albeit with non-Cottrellian time-dependence. In Equation (3.5), F is Faraday's constant, n is the mole number of electrons involved in the interfacial redox reaction, A is the contact area of the reduction interface, and $\mathcal{L}$ is a positive constant related to L (appendix C) with dimensions of length. Note that no unphysical divergence exists at $\tau = 0$.

3.6 SAD Model Applied to Pascalammetry Data

Equation (3.5) is as tractable as the Cottrell equation, and fitting charge data from each pascalammetry measurement to the time integral of Equation (3.5)

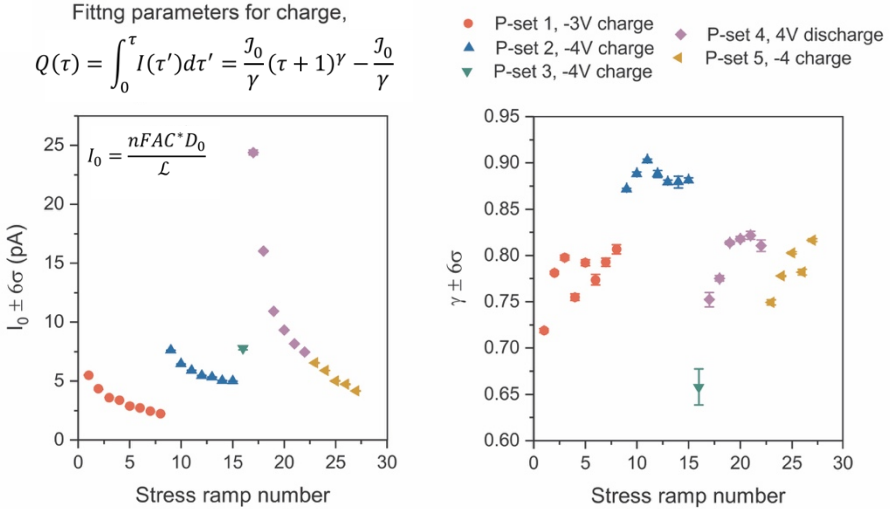

Figure 20: Charge fitting parameters I_0=$\mathcal{I}_0$/1s (left), and γ (right), for all pascalammetry measurements.

demonstrates exceptional agreement between experiment and theory. Provided in Figure 20 are the two fitting parameters, with confidence bands of >99.99% ($\pm 6\sigma$). Also displayed in Figure 20 is the integral of $I_{SAD}(\tau)$, the charge expression used for fitting, and the fitting parameter $I_0 \equiv I_{SAD}(\tau = 0)$.

A comparative analysis between the DAT for SAD, and Cottrell's solution to Fick's second law is facilitated with Figure 21 and Figure 24 below. Figure 21 displays normalized concentration and flux profiles for SAD (colors) and non-

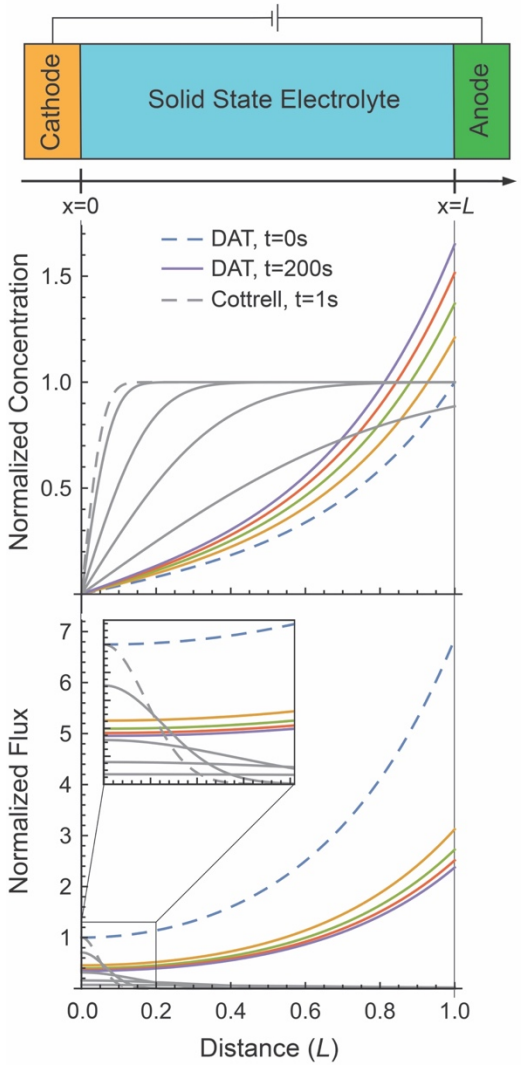

Figure 21: Plots share a common horizontal axis of electrolyte thickness from x=0 to x=L. Top – Schematic of an operando solid-state electrochemical storage device at constant potential difference. Middle – Evolution (0s-200s) of active species concentration profiles for stress-assisted diffusion/activation (colored) vs. Cottrellian (gray). Concentrations are normalized by $C(x,t)/C(L,0)$, and the early-time curves are dashed. Bottom – Evolution (0s-200s) of active species fluxes for stress-assisted diffusion/activation (colored) versus Cottrellian (gray). Fluxes are normalized by $j(x,t)/j(0,t_{min})$, and the early-time curves are dashed.

stressed diffusion (gray) over a time interval of 200s. All plots in Figure 21, including the schematic at the top, share the same horizontal axis for electrolyte

thickness, and parameters are chosen to match those of our experimental system (Appendix D). The earliest-time plots are dashed, and in the SAD case, concentration increases in time. Notably, a temporal increase in concentration matches the predictions from rigorous continuum and molecular dynamics models of SAD[139,141]. Fluxes are derived from Fick's first law in the usual way. Concentrations are normalized by $C(x,t)/C(L,0)$, while fluxes are normalized by $j(x,t)/j(0,t_{min})$. For the normalized fluxes, $t_{min} = 0$s for SAD, while $t_{min} = 1$s for Cottrell to avoid fictitious divergence.

For the non-stressed Cottrellian case (gray traces in Figure 21), larger concentrations and fluxes are found at opposite sides of the electrolyte: higher fluxes at the reduction interface, and higher concentrations at the oxidation interface. In the case of SAD (colored traces in Figure 21), described by the DAT, larger concentrations and fluxes both spatially reside at the same interface: the oxidation interface. This has important consequences. The DAT for SAD suggests that SAD itself may contribute to electrolyte degradation near the oxidation interface by mechanical failure due to increased concentration of active species, and/or hot spots, via increased fluxes. While normalized concentrations and fluxes are provided here for purposes of comparative analysis, other plots for the same time interval are also valuable: active species concentration in reference to stoichiometric concentration (Figure 22), as well as active species current density (Figure 23).

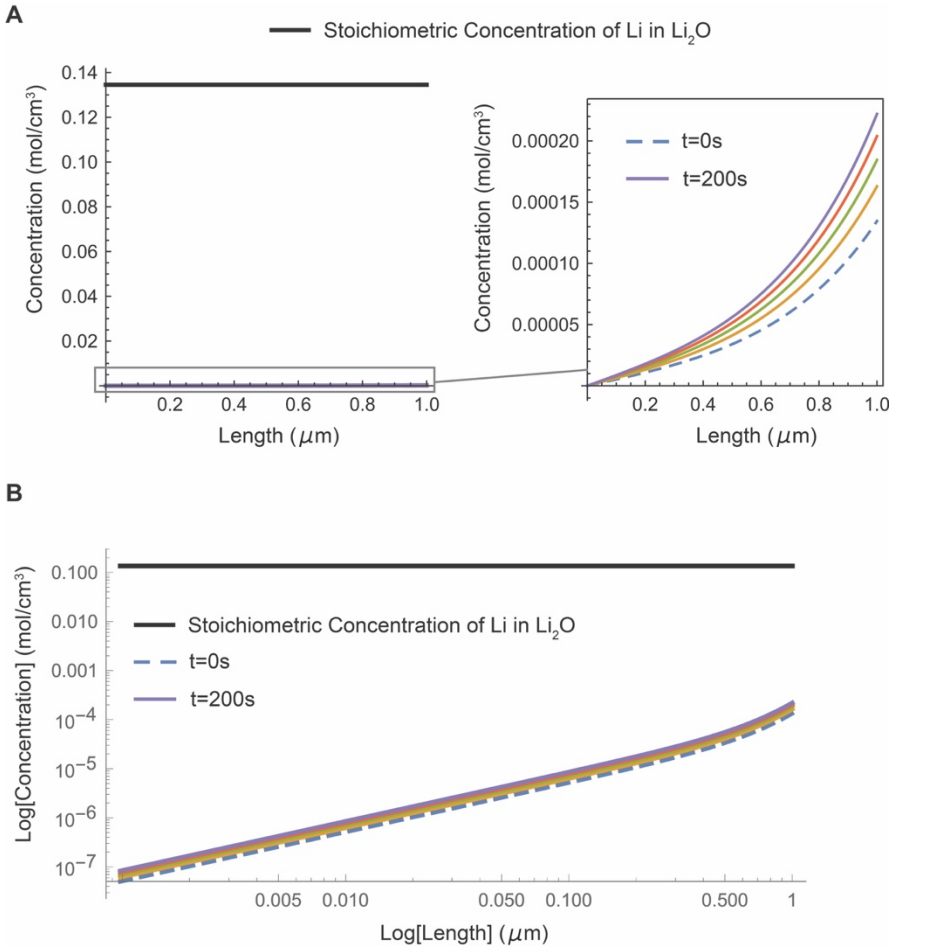

Figure 22: Temporal Evolution of Active Species Concentration Within Electrolyte During SAD (A) SAD Concentration profiles (colored curves) plotted in reference to the stoichiometric concentration of lithium in lithium oxide (black line). (B) SAD Concentration profiles (colored curves) plotted in reference to the stoichiometric concentration of lithium in lithium oxide (black line) plotted on a log scale. Recall that by construction, active species concentration is zero at x=0, the reduction interface.

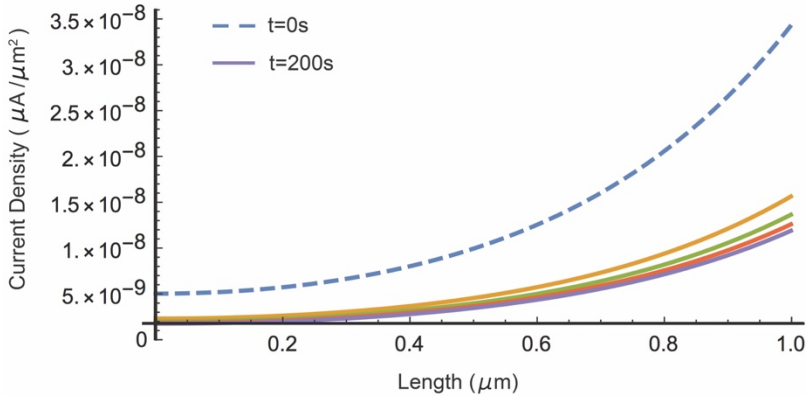

Figure 23: Evolution of active species current density within electrolyte during SAD

Continuing a comparative analysis between the DAT for SAD, and Cottrell's solution to Fick's second law, all plots in Figure 24 share the same time axis, and the middle and bottom plots are used to visualize important time-dependent physical results of describing SAD with the DAT. The top plot shows a sketch of the applied stress during a pascalammetry measurement, representing a time window in which applied stress crosses a threshold to generate SAD. The middle of Figure 24 is a plot of the total active species concentration in the

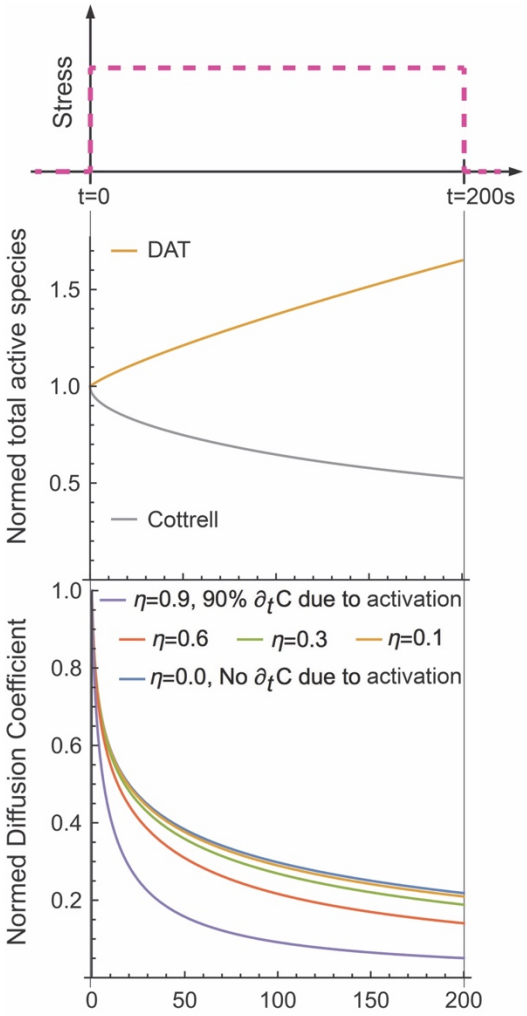

Figure 24: Top – Sketch showing applied stress. Middle – Evolution of the normed total active species within the electrolyte (integral of $C(x,t)/C(x,0)$, from x=0 to x=L). Bottom – Evolution of the normed time-dependent diffusion coefficient, $D(t)/D(0)$ for various fractions of latent species activation.

electrolyte as a function of time. Plotted in gold is the prediction that the total active species within an electrolyte increases during SAD. For comparison, the total active species concentration predicted by the Cottrell formalism is also plotted(gray), demonstrating that that formalism cannot replicate a physical phenomenon in which the total amount of active species within the electrolyte is increasing. The bottom of Figure 24 plots $D(t)/D_0$ for various changes in concentration due to local activation of inactive species. As shown in Equation (3.4), and plotted at the bottom of Figure 24, the diffusivity decreases in time (as concentration increases) after peak SAD current has been reached at $t = 0$s. We note that a decrease in diffusivity in compressively stressed electrochemical systems is also predicated in rigorous continuum and atomistic models[139,140] within spatial regions of high and increasing concentration. Lastly, from the DAT (Appendix C), the following inequality is derived

$$J_0 \equiv \frac{I_0}{A} < \frac{nFC^*D_0}{L} \tag{3.6}$$

which gives an upper bound on the SAD current density, J_0, during a stress-step. Because C^* and D_0 both have material-specific realistic ranges, Equation (3.6) can be used to estimate electrolyte thicknesses required to suppress or enhance this effect. In this way, scientists and/or engineers desiring to perform pascalammetry, or sense high stresses by the emergence of non-Cottrellian current evolution, can use Equation (3.6) as an initial guide for system design.

3.7 Conclusion

Generally, pascalammetry is a novel approach to controllably study all stress-related electrochemical/mechanical phenomena at any scale. Particularly at the micro-to-nano scale, pascalammetry with operando microbattery probes is ideally suited, as we demonstrated. Based on this work, we suggest that scientists and engineers look for ways to monitor operando solid-state batteries for the emergence of stress-assisted diffusional currents evolving according to the derived analog to the Cottrell equation, Equation (3.5). The observance of such currents proceeding in time according to $(\tau + 1)^{\gamma-1}$, where $0.5 < \gamma < 1$, indicate the presence of stress and provides the opportunity to detect stress-induced degradation in solid-state batteries.

Chapter 4: Nanoscale Solid-State Electrochemistry with Nanobattery Probes

4.1 Introduction: Motivation and Utility of Nanobattery Probes

The frontier of electrical energy storage (EES) research has intense efforts directed towards integrating nanoscale electrodes and technologies into functional electrochemical storage devices[30-33]. Simultaneously efforts are being made to better understand ion transport dynamics at the nanoscale. These EES efforts call for new methods for characterization and discovery of ion transport at the nanoscale. One powerful approach is to fabricate scanning probe microscopy (SPM) probes whose operating termini are either coated with, or completely composed of, electrochemically active materials. This class of SPM battery probes (BPs) can then be actuated for numerous creative approaches for local ion transport and characterization at desired interfaces, down to the nanoscale. Schematically shown in Figure 25 is a nanobattery probe (NBP) – a BP whose material coatings have nanoscale thicknesses.

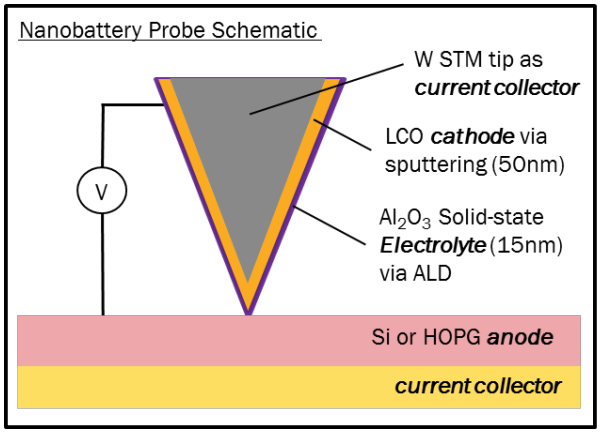

Figure 25: Schematic illustration of a nanobattery probe

By using NBPs within an existing SPM, nanoscale solid-state electrochemistry can readily be performed. The active materials for any redox reaction are spatially constrained to a nanoscale volume at the tip end. Consequently, local positioning of the NBP enables precision electrochemical studies of discrete nanostructures. Controlled positioning also enables the study of interface inhomogeneities such as domains, structural and composition defects, and variations in local morphology. This is illustrated in Figure 26 in which a NBP is positioned over two regions of a highly ordered pyrolytic graphite (HOPG) anode

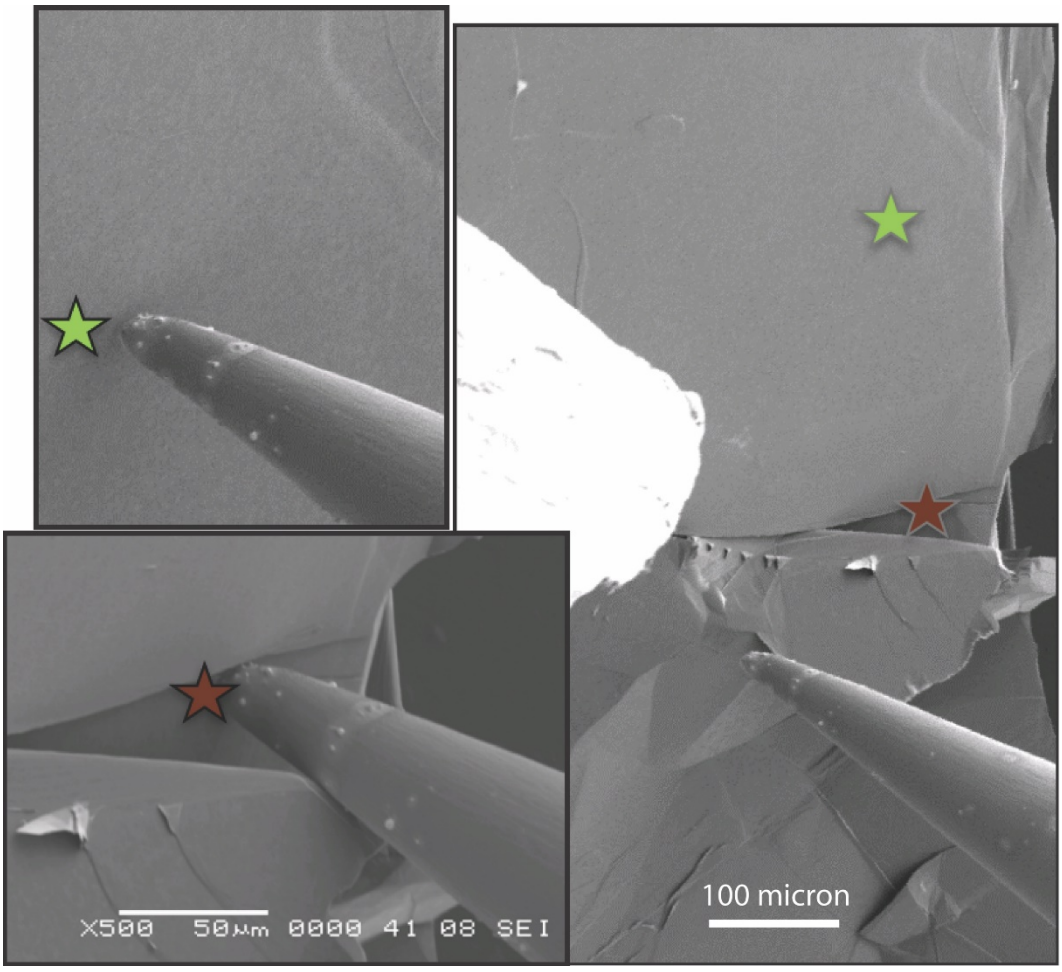

Figure 26: Scanning electron micrographs of a nanobattery probe positioned above two different regions of an anode (highly ordered pyrolytic graphite) with varied local morphology. The right-hand scanning electron micrograph is a wide-angle view with stars highlighting two local regions with different morphologies. The left- side demonstrate how the nanobattery probe can access these different regions for local nanoscale solid-state electrochemistry.

with vastly different local morphologies.

The integration of the NBP within the SPM measurement platform allows for multi-mode measurements. In addition to local nanoscale solid-state electrochemistry measurements, subsequent characterization of the locally charged/discharged region is tractable. After a local electrochemistry experiment, which involves local injection or removal of ion intercalant species (like lithium), retraction of the NBP exposes the region of interest. Exchange of the NBP for a conventional scanning tunneling microscope (STM) probe, or atomic force microscope cantilever (AFM) cantilever, allows the full arsenal of SPM tools to be employed.

In the present work, tungsten STM tips serve as the scaffold for the active battery materials needed to create BPs. Thus, the conductive tungsten scaffold functions also as a current collector, and can be electrochemically etched to have a desired tip radius of curvature (ROC) prior to coating with active materials. In this way, NBPs, or even microbattery probes (MBPs), like those used for pascalammetry in chapter three, can be made. The broad range of possible radii of curvature is shown in Figure 27. Before NBPs were utilized in nanoscale solid-

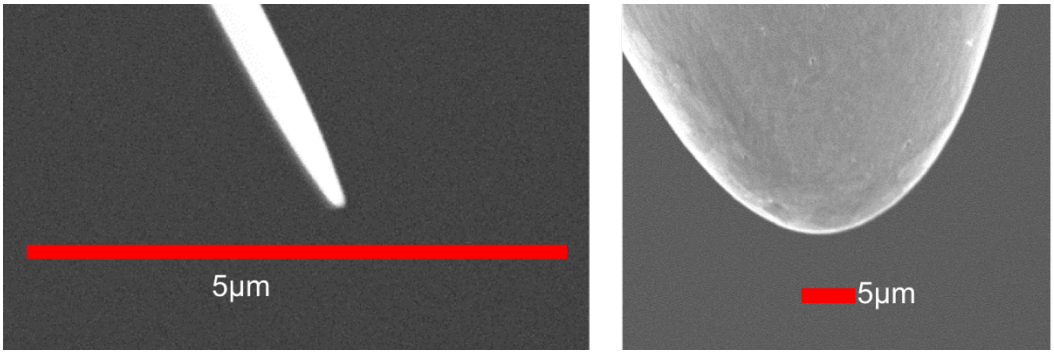

Figure 27: Scanning electron micrographs of STM tips prepared with nanoscale (left) and microscale (right) radii of curvature. By coating these tips with layers of active battery materials, battery probes appropriate to study phenomena at varied spatial scales can be fabricated.

state electrochemical experiments, the electronic and chemical properties of the coating materials on probe tips were characterized, as described below.

4.2 Electronic Characterization of NBPs: Inverted Tunneling Spectroscopy

In order to characterize the electronic properties of NBP coating materials in situ, – inverted scanning tunneling spectroscopy (ISTS) measurements were conceived and performed. Vacuum scanning tunneling spectroscopy (STS) is arguably the gold standard for measuring electron band gaps[46,144] and density of states[44,145,146] with high spatial resolution. In vacuum STS, a biased metallic STM tip is brought close to the surface of a semiconducting sample surface of interest, in ultra-high vacuum (UHV). When the tip-sample separation distance is within a range to support a steady-state vacuum-electron tunneling current, the tip-sample bias is swept. The derivative of the resulting tunneling current with respect to the applied bias voltage is proportional to the local electron density of states (LDOS) of the substrate[44,145,146].

While STS with a metallic tip and semiconducting substrate has been used to study the electronic properties of substrate *surfaces*, by the same logic, the electronic properties of semiconducting probe *tips* can be studied with tunneling spectroscopy against a metallic substrate. This follows the symmetry in the Hamiltonian for vacuum electron tunneling between two bodies: the density of states of the two bodies enter into the expression with exchange symmetry[44,46]. The characterization of probe-tip electronic properties through spectroscopy

measurements performed against a metallic film is denoted ISTS. Figure 28 displays a schematic of the ISTS setup.

$$I \propto \int_0^{eV} \rho_{tip}(\varepsilon)\ T(\varepsilon, eV, z)\, d\varepsilon$$

$$T(\varepsilon, eV, z) = \exp\left\{-\alpha z \left(\Phi + \frac{eV}{2} - \varepsilon\right)^{1/2}\right\}$$

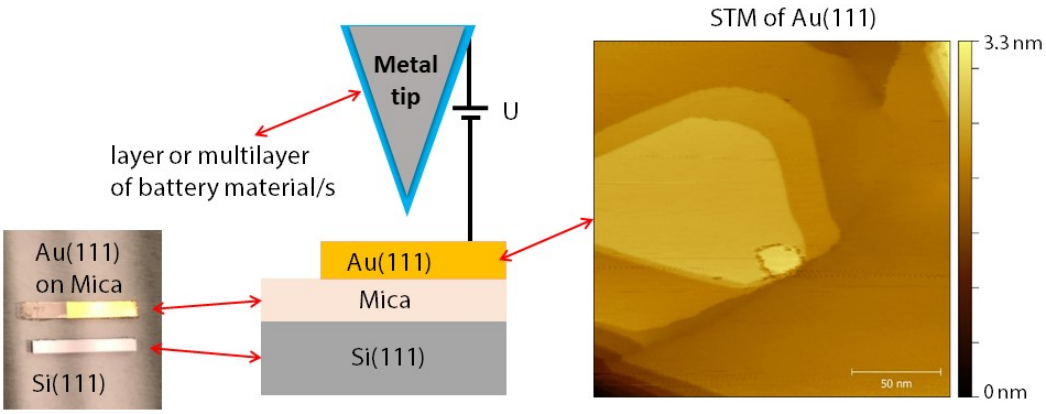

Figure 28: Expression for tunneling current (top) and schematic of inverted scanning tunneling spectroscopy (ISTS) for electronic characterization of probe coatings (bottom)

For the NBP experiments described herein, the chosen battery material coatings were lithium cobalt oxide ($LiCoO_2$) and aluminum oxide (Al_2O_3) as labelled in Figure 1. The solid-state electrolyte (SSE) chosen was a ca. 15 nm thick thin film of aluminum oxide (alumina) deposited by atomic layer deposition (ALD)[147]. The cathode material chosen was a ca. 50 nm thick coating of lithium cobalt oxide (LCO) deposited via sputtering. For electronic characterization of these materials with ISTS, single coatings on underlying metal tips were used. In this way, 15 nm thick alumina film coatings on sharp platinum iridium STM tips (~15 nm ROC) were characterized. As shown in Figure 29 below, ISTS measurements for the Al_2O_3 film give a band gap of ~8eV, close to the bulk value from the literature of ~9eV[148]. In Figure 29 each curve is an average of 30 local measurements. The four different colors correspond to four different spatial

locations that ISTS was conducted versus the Au(111) substrate. The initial tunneling conditions before sweeping the bias voltage from -6V to 6V were a current of -20pA, and a bias voltage of -6V (gold sample relative to tip).

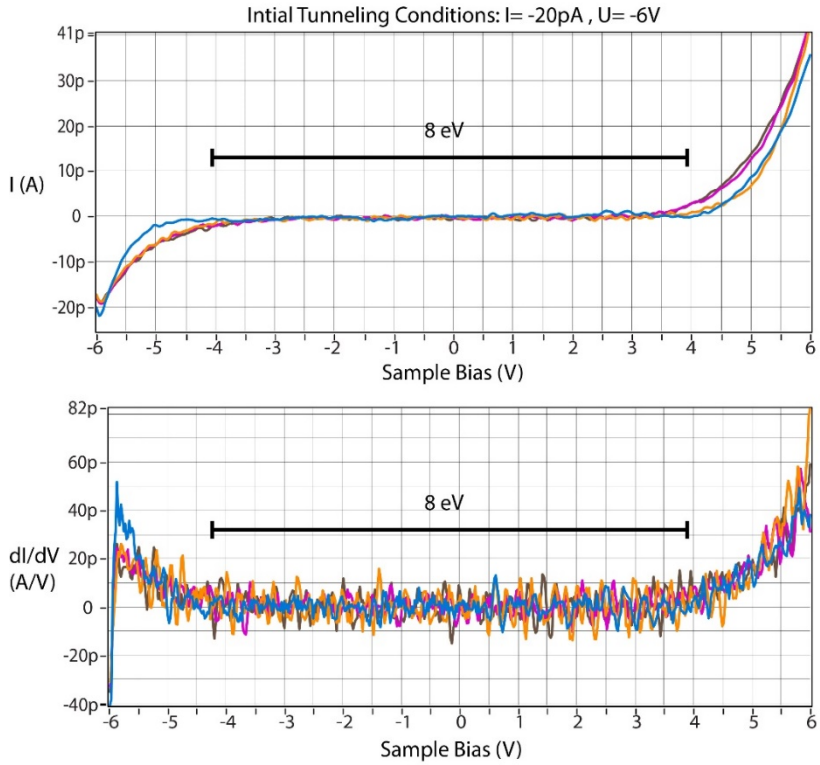

Figure 29: Inverted scanning tunneling spectroscopy data of 15nm thick coatings of alumina on platinum iridium STM tip versus a Au(111) substrate. The bar denotes the 8eV electronic band gap of bulk Al_2O_3.

To further corroborate the results of these ISTS measurements, additional ISTS measurements were repeated with initial current an order of magnitude larger than previously. These results are shown in Figure 30. As before, each trace is an average of 30 local measurements, and different colors refer to different planar locations the probe was positioned against the Au(111) substrate. The data confirm the conclusion that alumina conformally covers the STM tip, yielding the bulk electronic band gap of ~8eV. Similar measurements were conducted to electrically characterize ca. 50nm coatings of LCO on W STM tips, as displayed in Figure 31.

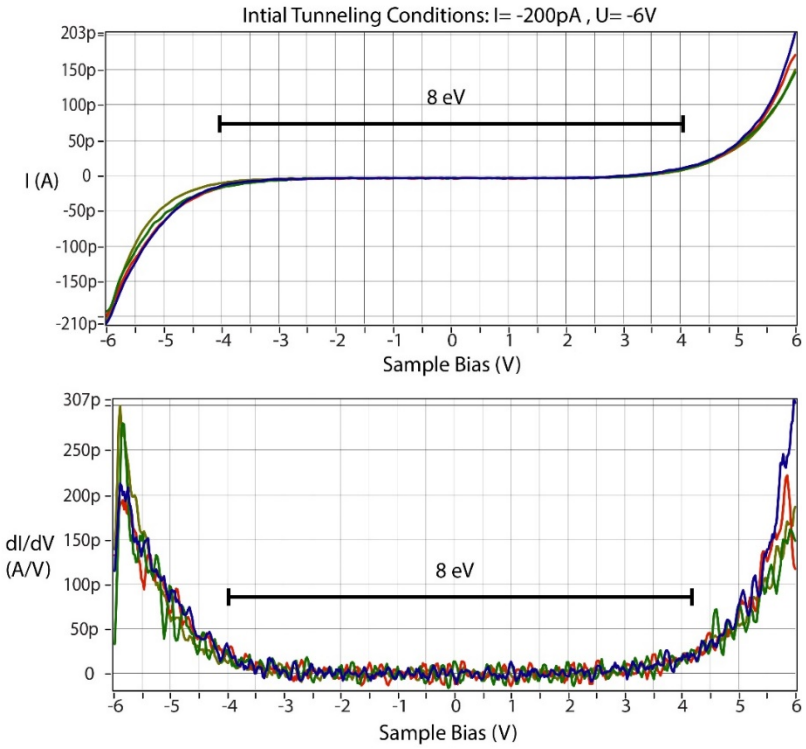

Figure 30: Inverted scanning tunneling spectroscopy data of 15nm thick coating of alumina on platinum iridium STM tip versus a Au(111) substrate

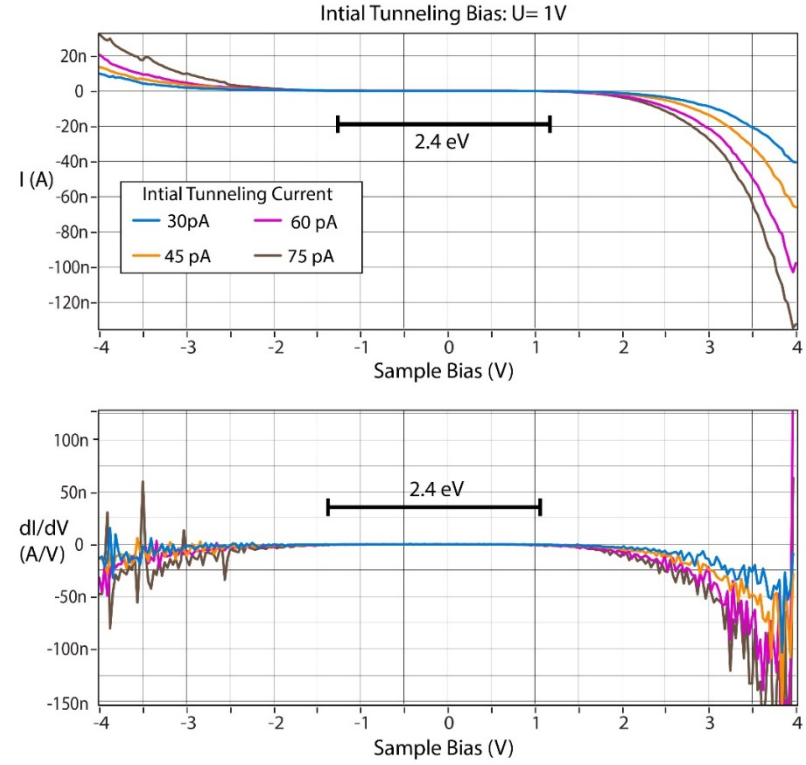

Figure 31: Inverted scanning tunneling spectroscopy data of 50nm thick coating of LCO on tungsten STM tip versus a Au(111) substrate. A 2.4 eV band gap reported for $LiCoO_2$.

Each trace is an average of ten measurements, and different colors correspond to different initial tunneling conditions. As highlighted in the figure, the measured band gap is consistent with the reported 2.4 eV band gap of LCO[148]. Based upon the observed band gap, can we can confirm a coating material of $LiCoO_2$.

4.3 Chemical Testing NBPs: Verifying Activity/Cyclability

The source of lithium (Li) in our NBP experiments is the LCO cathode. The chemical activity of Li in this geometry was studied to verify the LCO coating was of sufficient quality and quantity to support cycling of Li. The first step of this process was to determine the bias voltage threshold required to transfer lithium (induce lithiation). This was determined with a simple NBP probe consisting of a LCO-clad W tip, functioning as cathode/current collector, in mechanical contact with a silicon (Si) substrate functioning as an anode. In this contact junction, a voltage polarity, consistent with driving Li into the Si (charging bias) is applied. As shown in Figure 32, the absolute value of this charging bias (red trace) is step-wise increased to charge the Si anode, followed by restoring the bias to zero volts. If the current signal (blue trace) sustains a non-zero value with no bias applied, the current reflects ionic discharging of the nanobattery. (A chemical potential difference, for lithium, between lithiated silicon and LCO will drive discharge at zero bias.) As shown in Figure 32, the lithiated silicon discharges with currents in the range of 0.5 nA – 0.9 nA following charging with a bias voltage of an absolute value of 3V-4V. This confirms that the bias required to remove Li from the LCO

nano-cathode, and lithiate the Si anode, is within this range, and consistent with the voltage (4V) utilized in macroscopic batteries comprised of these materials.

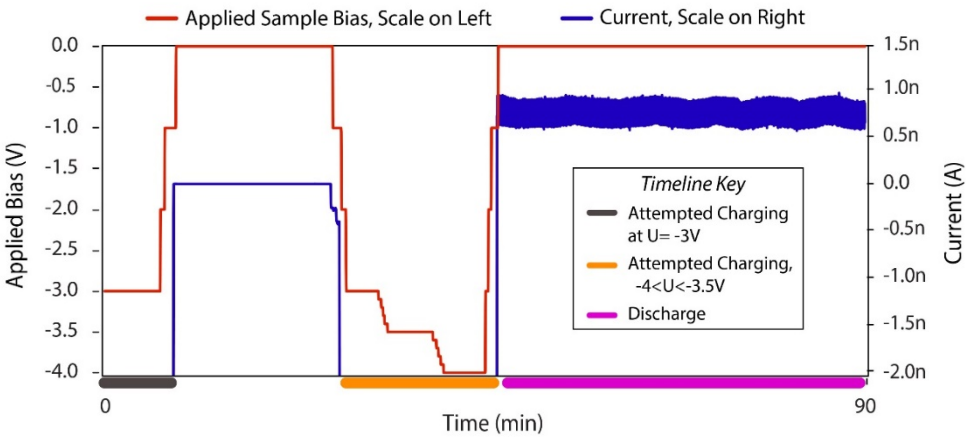

Figure 32: Data for the experimental determination of the potential difference threshold required to lithiate a Si(111) anode surface with a nanobattery probe having a lithium cobalt oxide cathode.

Further verification of chemical activity (ability to locally lithiate) was obtained from SEM measurements before and after attempts of local lithiation of a Si anode. Lithiation of silicon should be manifested as contrast changes in SEM images at the local region of lithiation, where solid-state amorphization[149,150] of Si has been induced by Li. A NBP is brought into mechanical contact with a Si(111) anode as schematically shown in Figure 33a. Figure 33b shows the NBP / Si anode junction just prior to mechanical contact. Once mechanical contact is made, a charging bias of 3.5V (above the threshold for lithiation) is applied and sustained for 2 min, before mechanical contact is broken by retraction of the NBP. This process is sequentially repeated to create a circular pattern on the Silicon anode. The NBP probe contact with the Si(111) (the spatial points of charging) was positioned along the circumference of a circle of ca. 1μ radius. Figure 33c-d

shows an SEM image of the Silicon surface following this spatially patterned lithiation. These lithiation features confirm the activity of the LCO nano-cathode coating.

A control experiment was conducted ca. 15μm to the right of the circle of lithiated Si with opposite bias polarity (Figure 33e). This was done to verify that the circle of contrast in Figure 33c-d was not due to mechanical indention or abrasion. A change in bias polarity would not make any substantive difference to mechanical scribing, and another circle of contrast should emerge. The SEM image demonstrates no such contrast for the same experiment with opposite polarity (Figure 33f). The patterned circle in the SEM images of Figure 33c-d are thus due to lithiation of Si. Both the electrical and chemical properties for these NBPs have thus been verified, enabling further solid-state electrochemical experiments at the nanoscale, as described below.

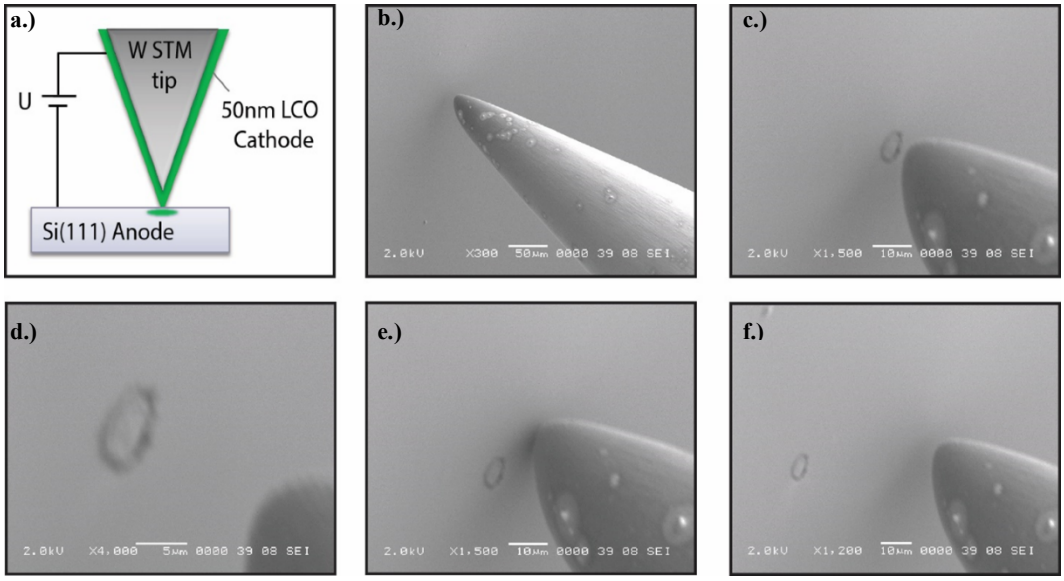

Figure 33: a.) Schematic of lithiation. b.)-d.) Data demonstrating the precision of local lithiation with nanobattery probes by "drawing" a circle of lithiated Si(111) at a bias of -3.5V. e.)-f.) The same experiment as in b-d, but with a bias of 3.5V, shows no change in SEM contrast. Therefore, the contrast in c-d is not due to mechanical abrasion and is attributable to local lithiation.

4.4 Potential Step, Staircase, and Cyclic Voltammetry with NBPs

Local solid-state electrochemical experiments were conducted as a proof of concept to develop and establish NBPs as a nanoscale electrochemical tool. In all the forthcoming described experiments, the full cell solid-state nanobattery materials and dimensions match those outlined in Figure 25: Si or HOPG (anode) / nano-thin alumina (electrolyte) / nano-thin LCO (cathode). Figure 34 shows representative data of potential step voltammetry experiments that were conducted. Eight sequential potential steps (dashed blue) between 0V and -4V induce current responses (solid black). As mentioned above, a negative bias in our experimental convention (Si sample lower potential than tip) corresponds to a bias polarity that will induce local charging, provided that the magnitude of the bias exceeds the charging threshold. A charging bias of -4V was chosen because it is sufficient to induce charging in the *electrolyte-free* case as shown in Figure 32. The alumina SSE, which is an ion-conductor when nano-thin[148,151], is not expected to raise

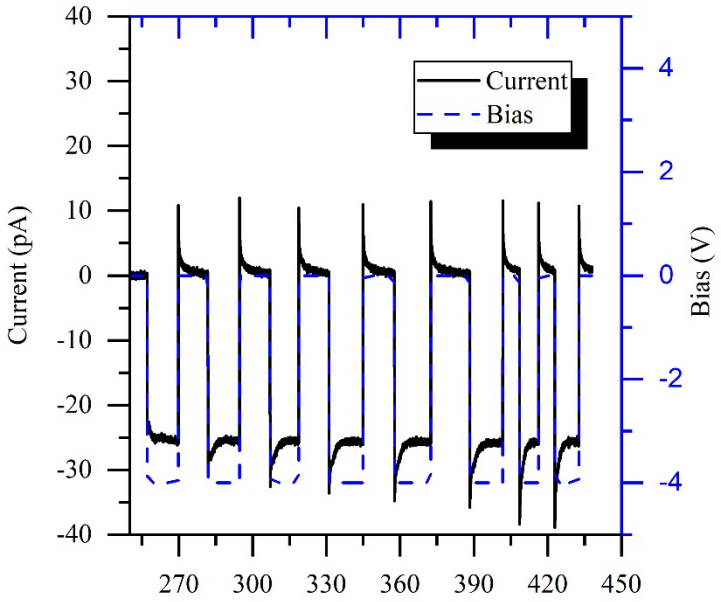

Figure 34: Potential step voltammetry of nanobattery probe vs. Si(111) between 0V and -4V (charging)

the threshold for lithium transfer. Indeed, the data from these potential step experiments, shown in Figure 34, demonstrate current transients that arise at the zero-bias condition after charging, consistent with spontaneous discharging.

Analysis of discharge current transients, with removal of early-time capacitive currents, reveals a range for how much charge is transferred faradaically during discharge of the nanobatteries. This charge window, by order of magnitude, is between 10 pC and 10 nC. Using the typical capacity of LCO, this corresponds to active volume of LCO ranging between 10^{-3} μm^3 and 1 μm^3. For perspective, this volume range is equivalent to the volume of spheres with radii ranging from 100nm – 800nm. Figure 35 shows another set of representative data from potential step voltammetry experiments with a partially charged nanobattery. In this case, six consecutive steps between 4V discharging and -4V charging. The results reveal that a single cycle of charging increases peak discharging currents from ca. 30pA

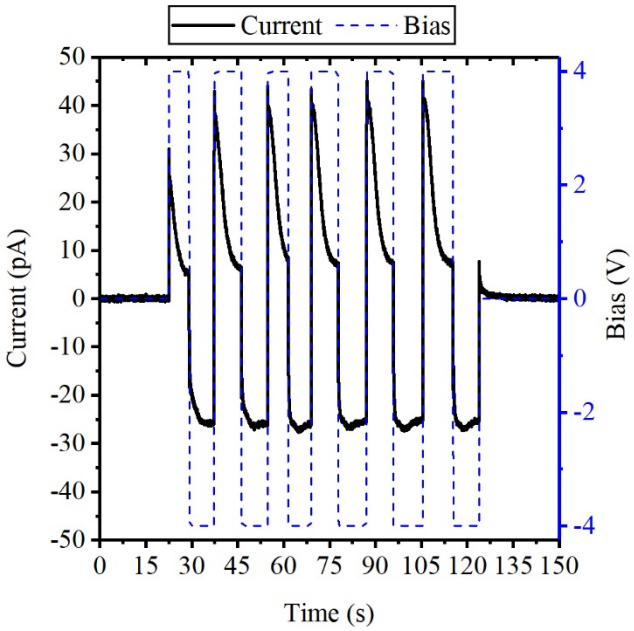

Figure 35: Potential step voltammetry of nanobattery probe vs. Si(111) between 4V (discharging) and -4V (charging)

to ca. 45 pA, attributable to the additional chemical potential difference that is established during charging.

Potential step experiments with longer step times provide additional insight into the lithium ion transfer kinetics. Plotted in Figure 36 are four consecutive potential step experiments between -4V (charging) and 4V (discharging). The duration of the potential steps are between 30 min and 1.5 hours. The potential steps occur congruent with points in time where the current sharply spikes in one direction or the other. The first two potential steps are highlighted with red (green) arrows indicating the point in time where -4V (4V) are applied.

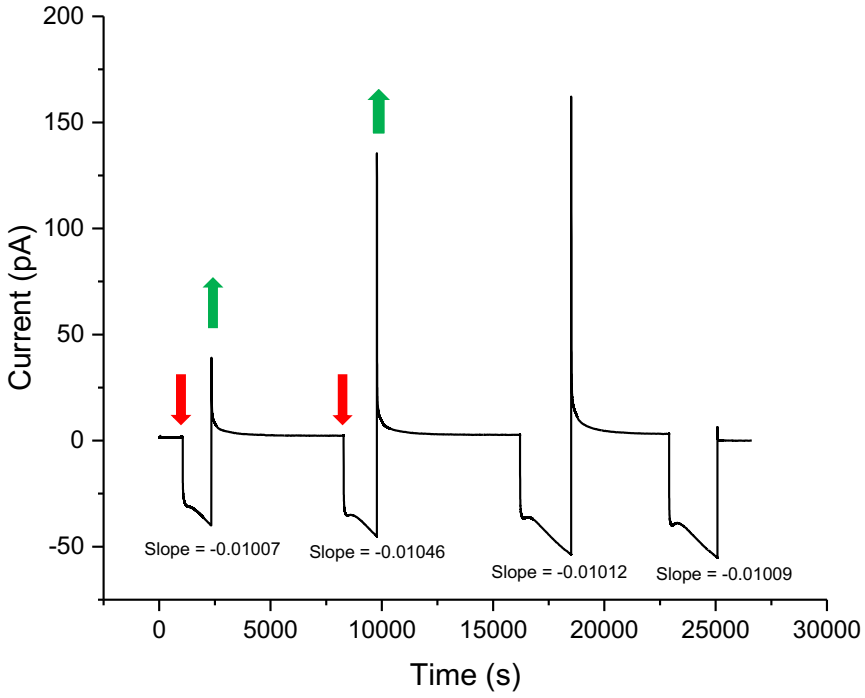

Figure 36: Potential step voltammetry of nanobattery probe vs. Si(111) between -4V (charging) and 4V (discharging). Potential steps occur at times where current sharply spikes positive or negative. The first two sets of potential steps are highlighted with red (-4V applied) and green arrows (4V applied).

Very interestingly, during charging, the absolute value of the current does not decay exponentially to a steady-state to indicate the expected diffusion-limited

current. Instead, after about 20 minutes of decay, the absolute value of the charging current actually begins to *increase*. The rate of this increase can be quantified by fitting lines to those segments – segments of current just above the slopes provided in Figure 36. For this nanobattery, on these time scales of about 0.5 hours, the rate of increase is 0.01pA/s = 36pA/hr. For another nanobattery probe this same phenomenon is found over much larger time scales of days, as shown in Figure 37. This can be explained through a combination of two mechanisms described in the following paragraph.

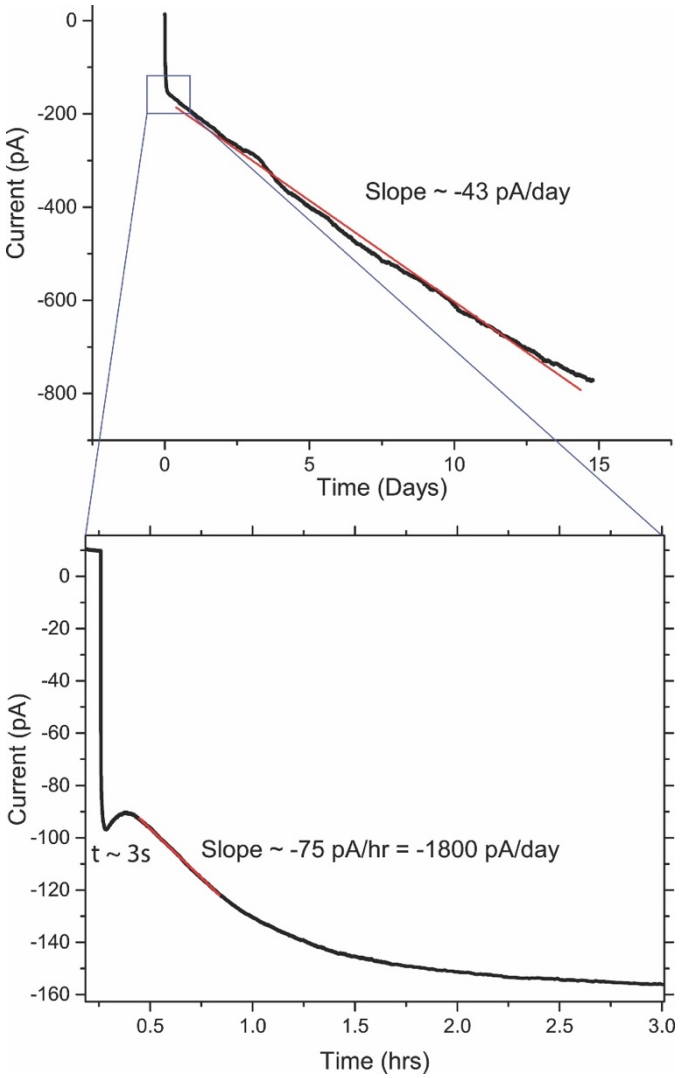

Figure 37: "Charging" of a NBP/Si(111) wafer for two weeks.

The "bottle-neck" material for electron and ion transport, both potential contributors to the measured current, is the alumina electrolyte. At the point of the potential step to a charging bias of -4V, LCO begins to delithiate, providing Li to the alumina electrolyte. As LCO delithiates, it becomes more electrically conductive[152], resulting in more of the potential drop to occur across the alumina electrolyte. This greater potential drop in the alumina increases the electric field in the alumina, and so ion migration and electron leakage currents will increase as a result. A second mechanism for the increase in the absolute value of the charging current could be the increase in ion diffusivity and electron conductivity within the alumina as its concentration of Li increases.

Finally, more complex voltammetry experiments are readily accessible with this NBP method. Displayed in Figure 38 are the signals of applied bias (blue) resistance (red), and current (black) for a staircase voltammetry experiment from 0V to -10V charging. Figure 39 shows 10 consecutive cyclic voltammetry (CV)

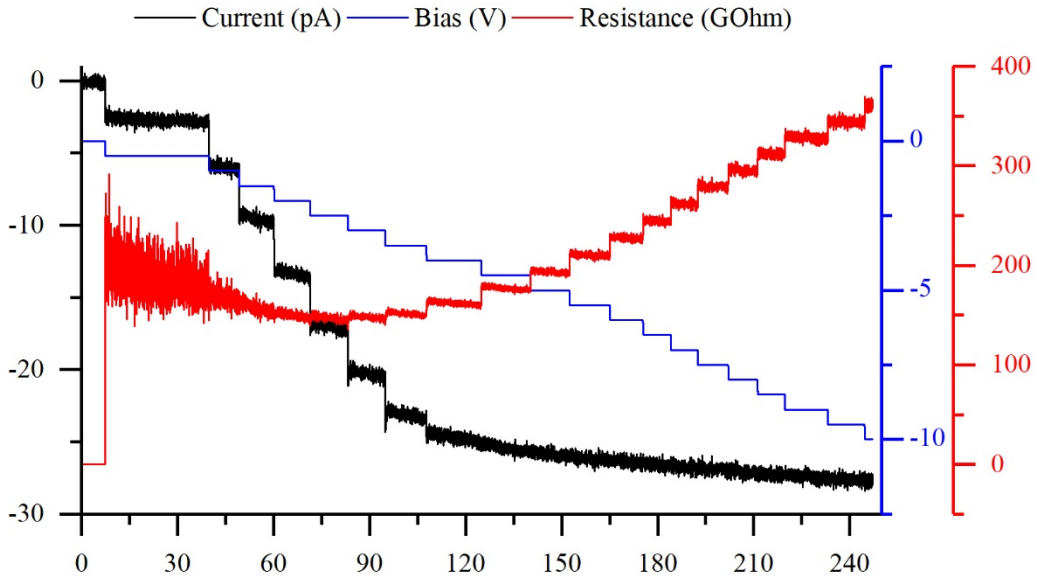

Figure 38: Traces of current (black), resistance (red), and applied bias (blue) for an applied staircase bias signal from 0V to -10V

experiments in which a NBP is in contact with mechanically exfoliated HOPG. The HOPG contact site for these nanoscale CVs was near the green star in Figure 26, and had local planar morphology. For these measurements bias was cycled between -8V and 8V at a rate of 1,300 mV/s. The first CV recorded the largest currents, and currents decreased for each subsequent cycle – establishing the viability to measure changes in capacity in these nanobattery systems. All these experiments demonstrate the capability and utility of NBPs for local, nanoscale solid-state electrochemical studies. Also, developed and demonstrated herein is ISTS for electrical characterization of high aspect ratio nano-thin films at their apex.

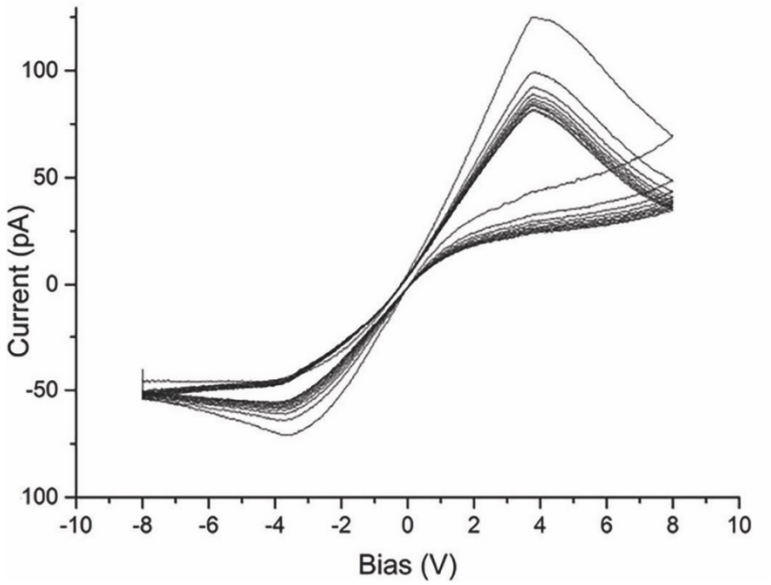

Figure 39: Ten consecutive cyclic voltammograms(CV) with bias ramp rate of 1,300 mV/s. NBP vs. HOPG. The first CV is the trace with the largest absolute current.

The ability to perform local lithiation experiments with NPBs opens up opportunities for the systematic measurements needed to extract quantitative insight on lithium insertion/deinsertion dynamics, and material-specific bottlenecks

to kinetic processes. In the future, we plan to perform more systematic CV measurements, so that variations in sweep rate can be used to relate the charging/discharging rate to the theoretical circuit. We are particularly interested in examining the kinetic role of the solid-state electrolyte, and anticipate that investigations performed as a function of electrolyte thickness or even electrolyte composition (alumina vs. lithium phosphorus oxynitride, "LiPON") can provide essential information. An additional avenue of exploration concerns finite-size effects. To date, experiments have been performed with macroscopic anodes, which are infinite sinks for lithium. Experiments that involve finite-sized anodes, perhaps as Si nanoparticles on a conductive (Pt) substrate, would provide a direct and microscopic path to explore capacity limits.

Chapter 5: Summary and Prospects for Scanning Battery Probe Approaches

Energy storage research is uniquely positioned in modern science and technology. Advancements in the field (or lack thereof), will affect the future of humans, ecosystems, environments, and economies in a positive (or negative) way. While there has been decades-long progress in the energy storage solutions of everyday portable electronic devices, major energy storage hurdles persist such as grid-scale storage, and economically viable, safe vehicular batteries. In an attempt to tackle these massive issues, the research community is looking beyond typical storage concepts, chemistries, electrolytes, and geometries.

Many of these approaches make use of nanoscale or mesoscale technologies. For example, one promising approach replaces conventional planar electrodes with a collection of nanostructures, arranged in dense mesoscale architectures, aiming to increase key figures of merit, like power density (via nanostructures) and energy density (via dense mesoscale architectures)[153]. Regardless of the novel approach, new techniques are needed for characterization and scientific discovery of operando solid-state electrochemical systems at the nano-to-microscale.

My dissertation research**,** described herein, has been vision-based to target these measurement needs within the energy storage community. The many specific, rich, and motivating scientific questions behind my research can be summarized in the following question: How does active material size, local

morphology, local intercalant-content (like Li), temperature, and stress affect local (and non-local), properties of relevant battery materials at the nano-to-microscale and contribute to battery degradation? My work has resulted in innovative approaches that enable basic energy storage discovery at the nano-to-microscale. These cutting-edge technologies, techniques, and theories are producing scientific discoveries that were previously intractable to experimentalists[49]. In the following, I summarize these advances, and provide suggested directions for future work.

Scanning Li-nanopipette and probe microscopy[49], described in chapter two, is based on an open-ended multi-walled carbon nanotube (MWCNT) affixed to the apex of a conductive atomic force microscope cantilever. The nanotube serves as both probe-tip and active counter electrode – that is, the MWCNT-terminated cantilever is a NBP. In this way, quantities of 10^{-2} - 10^{1} attograms of Li can be faradaically transferred at an interface of choice, with local nm-scale precision. This realistically enables the controlled faradaic transfer of 10^{2}-10^{6} atoms between nanoscale active materials, with the ability for subsequent, in situ, scanning-probe analysis.

Beyond the immediate experimental impact, this technique could be groundbreaking to the theoretical community: The lower-bound of atoms involved in the nanoscale redox reaction is on the order of the number of atoms that can be used in state-of-the art density functional theory simulations; thus, empirical data could greatly expedite progress in those calculational efforts. This could be done in a liquid or solid-state cell. Perhaps the most efficient way to begin such an effort

would be to delithiate Li-rich nanoparticles in ultra-high vacuum, as shown in Figure 40. Kelvin probe force microscopy of the nanoparticle before and after delithiation would provide an unprecedented empirical measure of how potential changes due to delithiation at the nanoscale. These results, in turn, could be used as baselines for density functional theory pseudopotential optimization. I note that this would be most helpful to the density functional theory community if performed at low temperature. Furthermore, extending these measurements to systems that host other ions, like magnesium, and/or other cathode materials with various oriented galleries for ion insertion/deinsertion would be exciting.

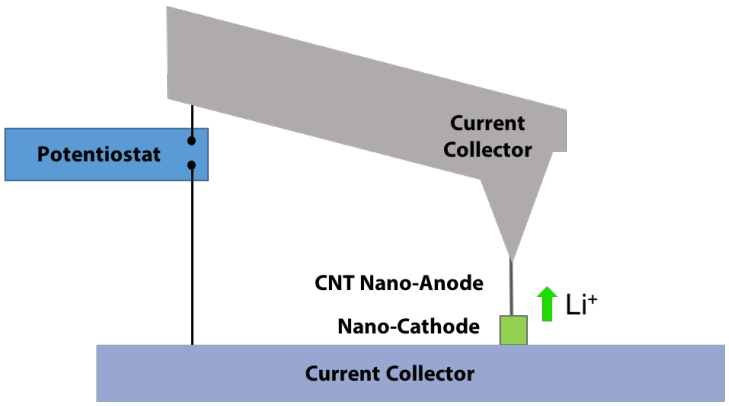

Figure 40: Schematic of possible scanning nanopipette and probe microscopy experiment to measure nanoscale changes is potential as a function of delithiation

Pascalammetry (chapter three), drawing inspiration from voltammetry, measures transient current responses induced by applied stresses to operando, solid-state microbatteries – all at constant chemical potential difference (bias). The experiment is enabled by use of microbattery probes in a SPM. By accessing this rarely studied phase space, pascalammetry has proven invaluable in elucidating

how ions move through stressed and degrading solid-state electrolytes. The work has resulted in the discovery of a previously unknown, simple to detect, measure of high stress in solid state batteries. This measure, a characteristic deviation from Cottrellian current evolution, indicates the presence of a phenomena called stress-assisted diffusion.

Because high stress in battery systems is common and has implications for performance and safety, further pascalammetry investigations on operando solid-state systems is warranted. So far, measurements have been conducted in a scanning tunneling set up in which there was no real-time measure of force. I suggest for a next stage of research to fabricate microbattery probes on the end of conductive atomic force microscopy cantilevers. Then, during stress ramps of pascalammetry measurements, force will be known. Consideration should be taken to the possible use of state-of-art force sensors, like tuning forks[154]. This measure, in conjunction with SPM measures of contact area post pascalammetry, can yield interfacial stress values. I also suggest measurements on systems with magnesium and sodium rich materials.

Inverted Scanning Tunneling Spectroscopy (chapter 4) inverts the paradigm of scanning tunneling spectroscopy by bringing a tip clad with a semiconducting battery material close to a metallic surface in order to perform IV-measurements to determine the electronic band gap of the battery material at the tip's end. The tip-end in this case mimics the apex of an individual, large aspect ratio, nanoscale structure within a mesoscale architecture of nanostructures – like the end of a nanotube in a forest of nanotubes. This technique enables the electronic

characterization of nano-thin material coatings at the apex of high aspect ratio nanostructures of direct relevance to basic energy storage science. I suggest future work should focus on controlled change in tip radius of curvature and in coating material thickness, to search the relevant parameter space for any unexpected emergent behavior of electronic properties that may be helpful or detrimental in a battery system. Also, tracking electronic changes to nano-thin material coatings as a function of delithiation would be of specific interest.

Nanobattery (Microbattery) probes, described in chapter 4, are metallic scanning tunneling microscope tips clad with nano (micro)-thick layers of active battery materials – literally a solid-state nanobattery (microbattery) half-cell. This is depicted on the left-hand side of Figure 41. When mechanical contact is made with a counter-electrode@current-collector, a *local* nanobattery (microbattery) full-cell is created. Since the lion's share of electrochemical energy storage experiments are performed in layered devices, like coin cells, all measurement results using such devices are implicitly insensitive to any form of planar inhomogeneity because results are averaged over the entire interfacial area. Nanobattery (Microbattery) probes enable precision-based *local* lithiation at the nanoscale (microscale), in order to study how local (and non-local) properties are affected by local topography, Li-content, stress, and degradation.

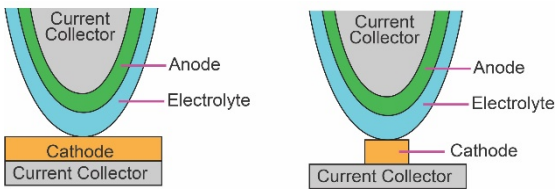

Figure 41: Schematic of a nanobattery probe (left) and nanobattery probe at nanoscale cathode (right)

There are numerous potential future research vectors to use microbattery and nanobattery probe technology and techniques. One such suggested approach is to perform nanoscale solid-state electrochemistry on nanoscale anodes and cathodes, as schematically shown on the right-hand side of Figure 41. This work could quantify how size affects electrochemical performance/properties of individual nanoparticles, providing highly relevant basic scientific information for EES science. This work would be of particular importance to experimentalists trying to design electrodes composed of mesoscale architectures of nanostructures. Finally, NBPs and MBPs should be leveraged to exhaustively explore all buried interfaces/surfaces as shown in Figure 42, especially as new chemistries and concepts for EES arise.

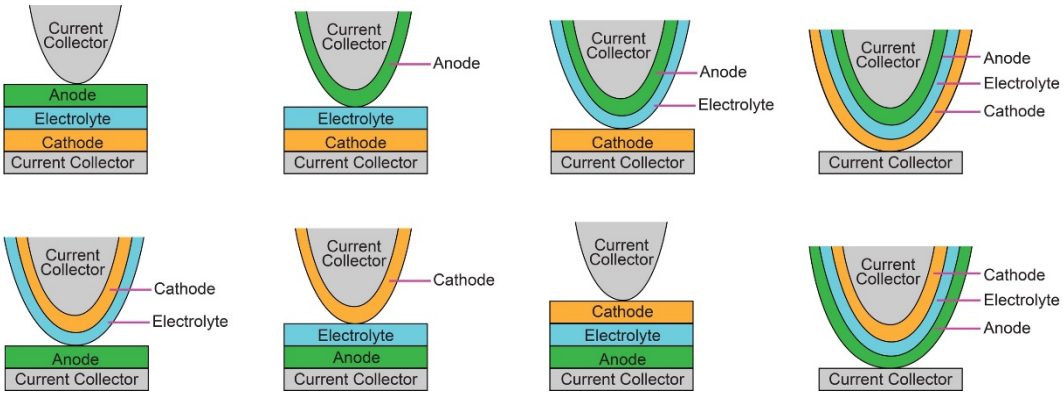

Figure 42: Schematic highlighting how all scientifically relevant battery interfaces/surfaces can be studied by use of nanobattery or microbattery probes with appropriate choice of layering materials

Appendices

Appendix A: Analytic Model of Chemical Surface Diffusion

Derivation of Equations (2.3) and (2.4) in Chapter two

The differential equation to be solved per Equation 2.2 in chapter 2 is

$$\frac{\partial \rho}{\partial t} = D\frac{1}{r}\frac{\partial}{\partial r}\left(r\frac{\partial \rho}{\partial r}\right) \tag{A.1}$$

An analytical solution to equation (A.1) is found by separation of variables. I assume:

$$\rho(r,t) = R(r)T(t) \tag{A.2}$$

which upon substitution into (A.1) yields:

$$R\dot{T} = DT\left[\frac{R'}{r} + R''\right] \tag{A.3}$$

Then, by separating the variables, Equation (A.3) becomes

$$\frac{\dot{T}}{DT} = \left[\frac{R'}{rR} + \frac{R''}{R}\right] \tag{A.4}$$

Now, choosing a negative separation constant of $-k^2$ gives two equations

$$\dot{T} = -k^2 DT \tag{A.5}$$

and

$$r^2 R'' + rR' + k^2 r^2 R = 0 \tag{A.6}$$

Equation (A.6) is a Bessel differential equation of zero order, and has two solutions: a zero order Bessel function of the first kind, $J_0(kr)$, and a zero order Bessel function of the second kind, $N_0(kr)$. Thus,

$$R(r) = A\, J_0(kr) + B\, N_0(kr) \tag{A.7}$$

As for the solution of Equation (A.5)

$$T(t) = Ee^{-Dk^2 t} \tag{A.8}$$

In (A.7) and (A.8) $A, B,$ and E are constants. So, the general solution now reads

$$\rho(r,t) = A\, J_0(kr) e^{-Dk^2 t} + B\, N_0(kr) e^{-Dk^2 t} + C \quad , \tag{A.9}$$

where I have chosen the most general solution by using the liberty to include an additive constant, C, to be determined.

Now I consider boundary conditions. Firstly, ρ must be finite within the vacancy island. As such, the constant B must vanish to avoid fictitious divergence at $r = 0$ that would arise from $N_0(kr)$ at $r = 0$. Secondly, the density of ad-lithium must be that of metallic lithium, g, at the vacancy island boundary for all time. In this cylindrical coordinate system with origin at the center of the island, the boundary occurs at the island radius, a. So, the second boundary condition is

$$\rho(r = a, t) = g \tag{A.10}$$

Using the results from above, and Equation (A.10) in (A.9) yields

$$g = A\,J_0(ka)e^{-Dk^2t} + C \tag{A.11}$$

Thus, two determinations can be made

$$C = g \tag{A.12}$$

and k is discretized to values of x_{0n}, the nth zero of J_0 Bessel function:

$$k \to k_n = \frac{x_{0n}}{a} \tag{A.13}$$

(A.12) and (A.13), along with $B = 0$ as discussed, into (A.9) gives Equation (2.3) from Chapter two as desired

$$\rho(r,t) = g + \sum_{n=1}^{\infty} A_n e^{-D\left(\frac{x_{0n}}{a}\right)^2 t} J_0\left(\frac{x_{0n}}{a} r\right) \tag{A.14}$$

Now, use of an initial condition with the orthogonality relationship of the J_0 Bessel function will lead to the determination of constants A_n. The initial condition is:

$$\rho(r, t = 0) = \rho_0(r) \tag{A.15}$$

The orthogonality relationship is:

$$\int_0^a r J_0\left(\frac{x_{0n'}}{a} r\right) J_0\left(\frac{x_{0n}}{a} r\right) dr = \frac{a^2}{2} [J_1(x_{0n'})]^2 \delta_{nn'} \tag{A.16}$$

Then, at time zero, multiplying by $r J_0\left(\frac{x_{0n'}}{a} r\right)$, and integrating (A.14), the following expression can be written

$$\int_0^a [\rho_0(\tilde{r}) - g] \tilde{r} J_0\left(\frac{x_{0n'}}{a} \tilde{r}\right) d\tilde{r} = \sum_{n=1}^{\infty} A_n \int_0^a \tilde{r} J_0\left(\frac{x_{0n}}{a} \tilde{r}\right) J_0\left(\frac{x_{0n'}}{a} \tilde{r}\right) d\tilde{r}$$

Use of (A.16) reduces the above to

$$\int_0^a [\rho_0(\tilde{r}) - g]\tilde{r}\, J_0\left(\frac{x_{0n'}}{a}\tilde{r}\right) d\tilde{r} = \sum_{n=1}^{\infty} A_n \frac{a^2}{2} [J_1(x_{0n'})]^2 \delta_{nn'}$$

which gives

$$\int_0^a [\rho_0(\tilde{r}) - g]\tilde{r}\, J_0\left(\frac{x_{0n'}}{a}\tilde{r}\right) d\tilde{r} = A_{n'} \frac{a^2}{2} [J_1(x_{0n'})]^2 \qquad (A.17)$$

Finally, (A.17) reduces to the last desired result: Equation (2.4) from chapter 2.

$$A_n = \frac{2}{a^2 [J_1(x_{0n})]^2} \int_0^a J_0\left(\frac{x_{0n}}{a}\tilde{r}\right) [\rho_0(\tilde{r}) - g]\, \tilde{r}\ d\tilde{r} \qquad (A.18)$$

Note: The initial conditions, $\rho_0(r)$, used in numerical modeling were defined as the density of metallic Li weighted with the initial experimental height profiles of the vacancy islands normalized to film thickness:

$$\rho_0(r) = \frac{z_{\text{experiment}}(r, t = 0)}{h} g \quad . \qquad (A.19)$$

Appendix B: Mathematica Code for Chemical Surface Diffusion

Continuum Model for Azimuthally Symmetric Vacancy Island Decay in Thin Films by Chemical Surface Diffusion:

User Inputs Needed for Model:

~Initial data for vacancy island height as a function of radial distance in {nm, nm}(denoted 'hic' in code)(list of ordered pairs: {{radial distance_1,height_1},{radial distance_2,height_2},...})

~Density of film in $\frac{ag}{nm^3}$ (denoted 'fd' in code)(constant)

~Film height in nm(denoted 'fh' in code)(constant)

~Data for vacancy island volume as a function of time in {mins, nm^3**}** (denoted 'v' in code)(a list of ordered pairs: { {time_1, volume_1}, {time_2, volume_2},....}): taken from experiment

~Number of terms (less one) to use in the Fourier-Bessel series expansion of the general solution (denoted 'nmax' in code)(constant)

~Boundary Distance in nm (denoted 'EDR' in code) (constant): The effective initial vacancy island radius. "EDR" comes from/is inspired by Gwyddion's "equivalent disk radius" grain-analysis option

Enter the appropriate information (as described above) into the cooresponding fields in "Step 1.)" below. Then evaluate the rest of the notebook for "Step 2.)."

Warning: A multi-core processing machine is required to run the below code

STEP 1.) Please enter the appropriate values below:

```
hic =;
fd =;
fh =;
v =;
nmax =;
EDR =;
```

STEP 2.) Please "Evaluate Notebook." Main results of the modeling will be printed and plotted at the end of the notebook.

```
(*Here I find the max radial distance
 with the hic data set and save it as 'radmax'*)
radmax = SortBy[hic, First][[Length[hic]]][[1]];
```

```
(*Here I check if the first time entry is zero,
and if not, shift all times entries accordingly*)
If[v[[1]][[1]] == 0, "first time entry was zero already",
 v = Table[{v[[i]][[1]] - v[[1]][[1]], v[[i]][[2]]}, {i, 1, Length[v]}];
]

(*Here I determine the max time of the data in minutes*)
maxtime = Take[v, -1][[1]][[1]];

(*Here I convert the experimental vacancy island volume measurments
 to total mass within the original region of interest (ROI)
 defined as the cylinder with height fh and radius EDR.*)
massMeasured =
  Table[{v[[i]][[1]], (π (EDR)^2 fh - v[[i]][[2]]) fd}, {i, 1, Length[v]}];

(*generating lists to be used in fitting*)
list7 = Table[r^i, {i, 0, 7}];
list7f = Table[r^i, {i, 1, 7}];



(*making fits to
 hic: two 7th order polynomial fits.  One constant basis
   true (cbt) and one constant basis false(cbf)*)
hicFit7th0 = LinearModelFit[hic, list7, r];
hicFit7th0cbf =
  LinearModelFit[hic, list7f, r, IncludeConstantBasis → False];



(*Here I take the bestfits from both LinearModelFits above.*)
hicFit = hicFit7th0["BestFit"];
hicFitf = hicFit7th0cbf["BestFit"];


(*Here I take the R^2 values from both LinearModelFits above.*)
hicFitRS = hicFit7th0["RSquared"];
hicFitfRS = hicFit7th0cbf["RSquared"];
```

```
(*Now plotting both fits along with the hic data*)
{Show[Plot[fh, {x, 0, radmax}, PlotStyle → {Thick, Black},
   PlotLegends → {"2σ Height"}], ListPlot[hic],
  Plot[hicFit, {r, 0, radmax}, PlotStyle → {Red, Thick}], AxesLabel →
   {"radius in nm", "initial vacancy vacancy height in nm"},
  PlotLabel → "cbt", ImageSize → Large],
 Show[Plot[fh, {x, 0, radmax}, PlotStyle → {Thick, Black},
   PlotLegends → {"2σ Height"}], ListPlot[hic],
  Plot[hicFitf, {r, 0, radmax}, PlotStyle → {Red, Thick}], AxesLabel →
   {"radius in nm", "initial vacancy vacancy height in nm"},
  PlotLabel → "cbf", ImageSize → Large]}

(*Here I convert the hicFits to density initial conditions (dic).*)
dicModel = hicFit / (hicFit /. r → EDR) * fd;
dicModelf = hicFitf / (hicFitf /. r → EDR) * fd;
```

Below is an algorithm to force experimentally valid constraints on ρ_0 that give both $\rho_0(\mathrm{EDR}) = \mathrm{fd}$ and $M^{th}_{ROI}(t=0) = M^{ex}_{ROI}(t=0)$. "p" (or "pf") below stands for "parameters" of the hic fit.

```
(*Here are the best fit parameters for the
 7th order fit to the hic data for cbt and cbf*)
p = hicFit7th0["BestFitParameters"];
pf = hicFit7th0cbf["BestFitParameters"];


(*   cbt M^th_ROI(t=0), coded as a function of hicFit parameters  *)
thryMroi0[P_] := NIntegrate[2 π fh (P.{1, r, r^2, r^3, r^4, r^5, r^6, r^7} /
      ((P.{1, r, r^2, r^3, r^4, r^5, r^6, r^7}) /. r → EDR)) * fd r, {r, 0, EDR}];


(*   cbf M^th_ROI(t=0), coded as a function of hicFitf parameters   *)
thryMroi0f[Pf_] := NIntegrate[
   2 π fh Pf.{r, r^2, r^3, r^4, r^5, r^6, r^7} / ((Pf.{r, r^2, r^3, r^4, r^5, r^6, r^7}) /. r → EDR) * fd r, {r, 0, EDR}];

(*   M^ex_ROI(t=0)   *)
expMroi0 = massMeasured[[1, 2]];
```

```
(* Now I generate the "test" functions....They take as
 their argument a parameters list and in turn calculate
 and output the % error between M_ROI^th(t=0) and M_ROI^ex(t=0) *)
test[P_] := N[Abs[(thryMroi0[P] - expMroi0)/expMroi0 * 100]]

testf[Pf_] := N[Abs[(thryMroi0f[Pf] - expMroi0)/expMroi0 * 100]]

(*Here functions are defined to generate
  a table of parameter lists.  Each parameter in
  the list is randomly generated to be within ±
 1% of the hicFit parameters found by the least squares method.*)

table[P_, num_] := Table[
  {RandomReal[{P[[1]] * .99, P[[1]] * 1.01}],
   RandomReal[{P[[2]] * .99, P[[2]] * 1.01}],
   RandomReal[{P[[3]] * .99, P[[3]] * 1.01}],
   RandomReal[{P[[4]] * .99, P[[4]] * 1.01}],
   RandomReal[{P[[5]] * .99, P[[5]] * 1.01}],
   RandomReal[{P[[6]] * .99, P[[6]] * 1.01}],
   RandomReal[{P[[7]] * .99, P[[7]] * 1.01}],
   RandomReal[{P[[8]] * .99, P[[8]] * 1.01}]
  }, {i, 1, num}]

tablef[Pf_, num_] := Table[
  {RandomReal[{Pf[[1]] * .99, Pf[[1]] * 1.01}],
   RandomReal[{Pf[[2]] * .99, Pf[[2]] * 1.01}],
   RandomReal[{Pf[[3]] * .99, Pf[[3]] * 1.01}],
   RandomReal[{Pf[[4]] * .99, Pf[[4]] * 1.01}],
   RandomReal[{Pf[[5]] * .99, Pf[[5]] * 1.01}],
   RandomReal[{Pf[[6]] * .99, Pf[[6]] * 1.01}],
   RandomReal[{Pf[[7]] * .99, Pf[[7]] * 1.01}]
  }, {i, 1, num}]

(*Here the number of randomized parameter lists to
 generate ('num' in code)is defined followed by steps
 to randomly generate and use the ideal parameter list
 for the cbt model.  The default value for num is 10^6*)

num = 1 000 000;

randplist = table[p, num];

Parallelize[
  Table[Append[randplist[[i]], test[randplist[[i]]]], {i, 1, num}]];

Sort[%, #1[[9]] < #2[[9]] &];
```

```
Take[%, 1][[1]];

bestp = Drop[%, -1];

bestphic = bestp.{1, r, r^2, r^3, r^4, r^5, r^6, r^7};

dicbestp = bestphic / (bestphic /. r → EDR) * fd;

(*Here I plot/check the dicModel along with the slightly
 perturbed dic having the best parameters for cbt*)

Plot[{dicModel, dicbestp, fd},
 {r, 0, EDR}, PlotStyle → {Black, Red, Yellow}]

thryMroi0[bestp]

expMroi0

(*Now I will follow the same procedure as above to randomly
 generate and use the ideal parameter list for the cbf model *)

randpflist = tablef[pf, num];

Parallelize[
  Table[Append[randpflist[[i]], testf[randpflist[[i]]]], {i, 1, num}]];

Sort[%, #1[[8]] < #2[[8]] &];

Take[%, 1][[1]];

bestpf = Drop[%, -1];

bestpfhic = bestpf.{r, r^2, r^3, r^4, r^5, r^6, r^7};

dicbestpf = bestpfhic / (bestpfhic /. r → EDR) * fd;

(*Here I plot/check the dicModel along with the slightly
 perturbed dic having the best parameters for cbf*)

Plot[{dicModelf, dicbestpf, fd},
 {r, 0, EDR}, PlotStyle → {Black, Red, Yellow}]

thryMroi0f[bestpf]

expMroi0
```

This marks the end of the algorithm to force experimentally valid constraints on ρ_0.

```
(*Here I generate a list of the
 first n zeros of the J0 Bessel function*)
x0 = Parallelize[Table[N[BesselJZero[0, i]], {i, 1, nmax}]];
```

```
(*Here I define the expansion coefficients
  of the general solution in terms of the 7th-
 order parameter-optimized dic fit for both cbt
  and cbf.  Each list will have nmax terms.*)
an = Parallelize[Table[N[ 2/((EDR)^2 (BesselJ[1, x0[[i]]])^2)
       Integrate[(dicbestp - fd) BesselJ[0, x0[[i]] * r/EDR] r,
        {r, 0, EDR}]], {i, 1, nmax}]];

anf = Parallelize[
    Table[N[ 2/((EDR)^2 (BesselJ[1, x0[[i]]])^2) Integrate[(dicbestpf - fd)
          BesselJ[0, x0[[i]] * r/EDR] r, {r, 0, EDR}]], {i, 1, nmax}]];

(*Here I define and generate a list of the terms of
 the general solution for both IC cases of cbt and cbf*)
ρterms = Append[Table[
     an[[i]] e^(-d (x0[[i]]/EDR)^2 t) BesselJ[0, x0[[i]] * r/EDR], {i, 1, nmax}], fd];

ρfterms = Append[Table[
     anf[[i]] e^(-d (x0[[i]]/EDR)^2 t) BesselJ[0, x0[[i]] * r/EDR], {i, 1, nmax}], fd];

(*Here I define functions to show how well the nmax-
 term general solution can reproduce the 7th order parameter-
 optimized dic having cbt or cbf.  I
  use these at the end of the notebook.*)

diccomp = Show[
   Plot[Total[ρterms] /. t → 0, {r, 0, EDR},
    PlotRange → {{0, EDR}, {0, fd}}, PlotStyle → {Orange, Thick},
    PlotLegends → {nmax "-Term General Solution IC: ρ(t=0,r)"}],
   Plot[dicbestp, {r, 0, EDR}, PlotStyle → {Red, Dashed, Thick},
    PlotRange → {{0, EDR}, {0, fd}},
    PlotLegends → {"7th Order parameter-optimized dic cbt"}],
   Plot[fd, {r, 0, EDR}],
   ImageSize → Large,
   PlotLabel → "CBT density IC vs General Solution ρ(t=0,r)"
  ];
```

```
diccompf = Show[
 Plot[Total[ρfterms] /. t → 0, {r, 0, EDR},
    PlotRange -> {{0, EDR}, {0, fd}}, PlotStyle -> {Orange, Thick},
    PlotLegends -> {nmax "-Term General Solution IC: ρ(t=0,r)"}],
   Plot[dicbestpf, {r, 0, EDR}, PlotStyle -> {Red, Dashed, Thick},
    PlotRange -> {{0, EDR}, {0, fd}},
    PlotLegends -> {"7th Order parameter-optimized dic cbf"}],
 Plot[fd, {r, 0, EDR}],
 ImageSize -> Large,
 PlotLabel -> "CBF density IC vs General Solution ρ(t=0,r)"
 ];

(*Now I move on to actually calculating diffusion coefficients*)

(*~~~~~~~~Now the total mass in the "region of interest"
  (ROI) is modeled by integrating the general
  solution ('d' and 't' free parameters)~~~~~~~~*)
massModel = Total[Parallelize[Table[Integrate[ρterms[[i]] r,
      {r, 0, EDR}, {z, 0, fh}, {ϕ, 0, 2 π}], {i, 1, nmax + 1}]]];
massModelf = Total[Parallelize[Table[Integrate[ρfterms[[i]] r,
      {r, 0, EDR}, {z, 0, fh}, {ϕ, 0, 2 π}], {i, 1, nmax + 1}]]];
(*~~~~~~~~~~~~~~~~~~~~~~~~~~~~~~~~~~~~~~~~~~~~~~~~~~~~~~~~~~~~~~~~~~~~~~~~
 ~~~~~~~~~~~~~~~~~~~~~~~~~~~~~~~~~~~~~~~~~~~~~~~~~~~~~~~~~~~~~~~~~~~~~~~~*)

(*Here I define the M^th_V0(t;
  d) and the scaled mass normalized as: M^th_V0(t;d) / M^exp_V0,max for cbt and cbf*)
massinV0Model = massModel - expMroi0;

massinV0ModelScaled = massinV0Model / (v[[1, 2]] * fd);

massinV0Modelf = massModelf - expMroi0;

massinV0ModelfScaled = massinV0Modelf / (v[[1, 2]] * fd);

(*Here I define the M^exp_V0(t)*)
massinV0Measured = massMeasured -
   Table[{0, massMeasured[[1]][[2]]}, {i, 1, Length[massMeasured]}];

(*Here I define the scaled mass to be nomalized: M^exp_V0(t) / M^exp_V0,max *)

massinV0MeasuredScaled =
  Table[{massinV0Measured[[i, 1]], massinV0Measured[[i]][[2]] / (v[[1, 2]] * fd)},
   {i, 1, Length[massinV0Measured]}];
```

```
(*Here the diffusion
       coefficient is modeled for two cases: 1.) M^ex_ROI(t;
      d)=M^th_ROI(t;
      d) and 2.) M^ex_V0(t;d)/(V0*fd)=M^th_V0(t;d)/(V0*fd).  Note that
  in the second case mass diffused into the initial
  vacancy island volume is equated and normalized
  to the max allowable diffused mass. *)
nlm = NonlinearModelFit[massMeasured,
   massModel, d, t, ConfidenceLevel → .99];
nlmf = NonlinearModelFit[massMeasured, massModelf,
   d, t, ConfidenceLevel → .99];

nlm2 = NonlinearModelFit[massinV0MeasuredScaled,
   massinV0ModelScaled, d, t, ConfidenceLevel → .99];
nlm2f = NonlinearModelFit[massinV0MeasuredScaled,
   massinV0ModelfScaled, d, t, ConfidenceLevel → .99];

(*Here I extract and define the 99% confidence interval,
d estimate, and R-Squared values.  Note I convert
  the found diffusion coefficient from nm^2/min to cm^2/s*)
CImin = nlm["ParameterConfidenceIntervalTable"][[1]][[1]][[2]][[4]][[
    1]] * 1/(60 (10^7)^2);

dEst = nlm["BestFitParameters"][[1]][[2]] * 1/(60 (10^7)^2);

CImax =
  nlm["ParameterConfidenceIntervalTable"][[1]][[1]][[2]][[4]][[2]] *
   1/(60 (10^7)^2);
RS = nlm["RSquared"];



CIminf =
  nlmf["ParameterConfidenceIntervalTable"][[1]][[1]][[2]][[4]][[1]] *
   1/(60 (10^7)^2);

dEstf = nlmf["BestFitParameters"][[1]][[2]] * 1/(60 (10^7)^2);

CImaxf =
  nlmf["ParameterConfidenceIntervalTable"][[1]][[1]][[2]][[4]][[2]] *
```

```
    1
  ----------;
  60 (10^7)^2
fRS = nlmf["RSquared"];



CImin2 =
  nlm2["ParameterConfidenceIntervalTable"][[1]][[1]][[2]][[4]][[1]] *
    1
  ----------;
  60 (10^7)^2
dEst2 = nlm2["BestFitParameters"][[1]][[2]] * 1/(60 (10^7)^2);
CImax2 =
  nlm2["ParameterConfidenceIntervalTable"][[1]][[1]][[2]][[4]][[2]] *
    1
  ----------;
  60 (10^7)^2
RS2 = nlm2["RSquared"];



CImin2f =
  nlm2f["ParameterConfidenceIntervalTable"][[1]][[1]][[2]][[4]][[1]] *
    1
  ----------;
  60 (10^7)^2
dEst2f = nlm2f["BestFitParameters"][[1]][[2]] * 1/(60 (10^7)^2);
CImax2f =
  nlm2f["ParameterConfidenceIntervalTable"][[1]][[1]][[2]][[4]][[2]] *
    1
  ----------;
  60 (10^7)^2
fRS2 = nlm2f["RSquared"];


(*writing code to compose a grid (and a plot)
 of the findings from the above modeling*)
```

```
grid = Grid[{
    {"Type of Model", "M_ROI^th(t=0)-M_ROI^exp(t=0)",
     "99% CI min for D in cm^2/s", "Estimate for D in cm^2/s",
     "99% CI max for D in cm^2/s", "R-Squared for D Estimate"},
    {"7th Order parameter-optimized
fit(with cbt), to z_0
data gives ρ(t=0,r).
Not Normalized/ROI",
     thryMroi0[bestp] - expMroi0, CImin, dEst, CImax, RS},
    {"7th Order parameter-optimized
fit(with cbt), to z_0
data gives ρ(t=0,r).
Not Normalized/ROI",
     thryMroi0f[bestpf] - expMroi0, CIminf, dEstf, CImaxf, fRS},
    {"7th Order parameter-optimized
fit(with cbt), to z_0
data gives ρ(t=0,r).
Normalized/V_0",
     thryMroi0[bestp] - expMroi0, CImin2, dEst2, CImax2, RS2},
    {"7th Order parameter-optimized
fit(with cbt), to z_0
data gives ρ(t=0,r).
Normalized/V_0",
     thryMroi0f[bestpf] - expMroi0, CImin2f, dEst2f, CImax2f, fRS2}
   }, Frame → All];
```

```
show = Show[Plot[(massinV0ModelScaled) /. d → dEst2 * 60 (10^7)^2,
    {t, 0, maxtime}, PlotStyle → {Black, Thick},
    PlotLegends → {" M_V0^th (t) / M_max, cbt"}, PlotRange → Full],
   Plot[(massinV0ModelfScaled) /. d → dEst2f * 60 (10^7)^2,
    {t, 0, maxtime}, PlotStyle → {Orange, Dashed, Thick},
    PlotLegends → {" M_V0^th (t) / M_max, cbf"}, PlotRange → Full],
   Plot[1, {t, 0, maxtime}, PlotStyle → {Red, Thick},
    PlotLegends → {"Max mass allowable in V0"}],
   ListPlot[massinV0MeasuredScaled, PlotStyle → {PointSize[.02]},
    PlotLegends → {"Data"}],
   AxesLabel → {"t (mins)", " M_V0^th (t) / M_max "},
   ImageSize → Large,
   PlotLabel → "Theory vs. Experiment for Normalized Mass in V0",
   PlotRange → {0, 1.1}
  ];

(*NOW SHOWING ALL RESULTS*)

{diccomp,
 diccompf,
 show,
 grid}
```

Appendix C: Diffusion/Activation Theory for Stress-Assisted Diffusion

Derivation of Equation (3.1) in Chapter 3

The total active species within a volume V is

$$N(t) = \int C(x, y, z, t)\, dV \tag{C. 1}$$

A change in the total active species can only occur in one of two ways:

1) Flux through a bounding surface S
2) Creation or annihilation of active species within V

$$\partial_t N(t) = -\oint \vec{j} \cdot \overrightarrow{dS} + \int \sum(x, y, z, t) dV \tag{C. 2}$$

Using the divergence theorem in (C.2) and combining with (C.1)

$$\int \partial_t C(x, y, z, t)\, dV = -\int \vec{\nabla} \cdot \vec{j}\, dV + \int \sum(x, y, z, t) dV \tag{C. 3}$$

Now because each term in (C.3) is a volume integral

$$\partial_t C(x, y, z, t) = -\vec{\nabla} \cdot \vec{j} + \sum(x, y, z, t) \tag{C. 4}$$

Now, using Fick's first law, with (C.4), and allowing a spatially constant time-dependent diffusion coefficient, Equation (3.1) is found in one dimension.

$$\frac{\partial}{\partial t}\, C(x,t) = D(t)\, \nabla^2\, C(x,t) + \Sigma(x,t) \qquad \text{(C. 5)}$$

This method of allowing a combination of a spatially constant time-dependent diffusion coefficient, $D(t)$, simultaneously with a *positive* source term, $\Sigma(x,t)$, is a modeling approach unique me.

Derivation of General Analytical Solution to the Diffusion/Activation Equation

As described in Chapter 3, (C.5) above is written as a diffusion/activation equation (DAE):

$$\frac{\partial}{\partial t}\, C(x,t) = \frac{D(t)}{1-\eta}\, \frac{\partial^2}{\partial x^2}\, C(x,t) \qquad \text{(C. 6)}$$

The DAE, Equation (C.6) above, is generally valid for cases of

a) No advection
b) Adherence to Fick's first law as: $j = -D(t)\vec{\nabla}C(x,t)$
c) A spatially averaged effective activation source $\Sigma = \eta \frac{\partial}{\partial t} C(x,t)$
d) No significant driving force effects like a strong electric field
e) Spatially constant (effective or otherwise) diffusion coefficient
f) Temporally varying, spatially averaged diffusion coefficient

In order to solve the DAE for our stressed system and describe "stress-assisted diffusion" (SAD), we must make an ansatz guided by five intuitive constraints for current $I(t)$ and charge $Q(t)$. (In this appendix, it is understood that the current and charge variables are for SAD, and subscripts for "SAD" are thus omitted.)

I) $Q(t) = \int_0^t I(t')dt'$

II) $Q(t = 0) = 0$

III) $I(t = 0) = finite$

IV) The functional form of $Q(t)$ must be a good fit to experimental data without over-parameterization

V) The functional form of $I(t)$ and $Q(t)$ must be related to an *analytical solution* of the DAE in the following way:

$$I(t) = -1 * A * j(0,t) * nF = nFAD(t)\frac{\partial}{\partial x}[C(x,t)]|_{x=0} \qquad (C.7)$$

So, the ansatz made is that the simplest general functional form to meet these requirements is

$$I(t) = I_0\left(\frac{t}{t_0} + \tau_0\right)^{\gamma-1} \quad , \qquad (C.8)$$

where I_0, t_0, τ_0, and γ are constant parameters. The first two, I_0 and t_0, have dimensions of current and time respectively. The last two, τ_0 and γ, are dimensionless. I note that while four free parameters are included here for generality, in order to satisfy intuitive constraint IV listed above, the number of free parameters in this work will be reduced to two as described below equation (C.31).

Integration of (C.8), according to requirement II.) gives

$$Q(t) = \int_0^t I(t')dt' = \frac{t_0 I_0}{\gamma}\left(\frac{t}{t_0} + \tau_0\right)^{\gamma} - \frac{t_0 \tau_0^{\gamma} I_0}{\gamma} \tag{C.9}$$

Now by use of (C.6)-(C.8), one can obtain an analytical solution for the DAE via standard separation of variables:

$$C(x,t) = X(x)T(t) \tag{C.10}$$

yielding two equations,

$$X''(x) = k^2\, X(x) \tag{C.11}$$

and

$$\dot{T}(t) = \frac{k^2}{1-\eta} D(t)\, T(t) \tag{C.12}$$

where a positive separation constant of k^2 is chosen. Now (C.10) into (C.7) with (C.8) gives

$$nFA\,D(t)\,X'(0)\,T(t) = I_0\left(\frac{t}{t_0}+\tau_0\right)^{\gamma-1} \tag{C.13}$$

or

$$D(t)\,T(t) = \frac{I_0\left(\frac{t}{t_0}+\tau_0\right)^{\gamma-1}}{nFA\,X'(0)} \tag{C.14}$$

Now (C.14) into (C.12) with integration gives

$$T(t) = \frac{k^2}{\gamma(1-\eta)}\;\frac{t_0 I_0\left(\frac{t}{t_0}+\tau_0\right)^{\gamma}}{nFA\,X'(0)} + \Phi \tag{C.15}$$

where Φ is a constant. (C.15) into (C.14) gives:

$$D(t) = \frac{I_0\left(\frac{t}{t_0}+\tau_0\right)^{\gamma-1}}{\left(\frac{k^2 t_0 I_0\left(\frac{t}{t_0}+\tau_0\right)^{\gamma}}{\gamma(1-\eta)} + \Phi nFA\,X'(0)\right)} \tag{C.16}$$

Now turning back to (C.11), its general solution is

$$X(x) = \alpha \cosh(kx) + \beta \sinh(kx) \qquad (C.17)$$

Assuming the reduction interface is at x=0, we choose a similar boundary condition that is used to derive the Cottrell equation, namely $C(x = 0, t) = 0$, meaning $X(x = 0) = 0$. Thus $\alpha = 0$ and

$$X(x) = \beta \sinh(kx) \qquad (C.18)$$

where β is a constant. Now (C.18) with (C.15) and (C.10) yield

$$C(x,t) = \frac{kt_0 I_0}{\gamma(1-\eta)nFA}\left(\frac{t}{t_0} + \tau_0\right)^{\gamma} \sinh(kx) + \Phi\beta \sinh(kx) \qquad (C.19)$$

where $X'(0) = \beta\, k$ has been used.

If the initial (possibly stress-altered) concentration at the electrolyte side of the oxidation interface is given by $C(L, t = 0) = C^*$, then a second boundary condition is $X(L)T(0) = C^*$. Applying this directly to (C.19) gives

$$\Phi\beta = \frac{C^*}{\sinh(kL)} - \frac{kt_0 I_0 \tau_0^{\gamma}}{\gamma(1-\eta)nFA} \qquad (C.20)$$

(C.20) then into (C.19) produces

$$C(x,t) = \left(\frac{kt_0 I_0}{\gamma(1-\eta)nFA}\left[\left(\frac{t}{t_0}+\tau_0\right)^{\gamma} - \tau_0^{\gamma}\right] + \frac{C^*}{\sinh(kL)}\right)\sinh(kx) \qquad (C.21)$$

The expression for the diffusion coefficient, (C.16), can likewise be simplified with (C.20)

$$D(t) = \frac{I_0\left(\frac{t}{t_0}+\tau_0\right)^{\gamma-1}}{\frac{k^2 t_0 I_0}{\gamma(1-\eta)}\left[\left(\frac{t}{t_0}+\tau_0\right)^{\gamma} - \tau_0^{\gamma}\right] + \frac{nFA\ kC^*}{\sinh(kL)}} \qquad (C.22)$$

where $X'(0) = \beta\ k$ has been used again. Now with (C.22), an expression can be derived for the initial diffusion coefficient as

$$D(0) \equiv D_0 = \frac{I_0\ \tau_0^{\gamma-1}\sinh(kL)}{nFA\ k\ C^*} \qquad (C.22)$$

which yields

$$I_0 = \frac{nFAC^* D_0\ k}{\tau_0^{\gamma-1}\sinh(kL)} \qquad (C.23)$$

then finally (C.22) and (C.23) with (C.21) and (C.22) gives the desired general analytical solution to the DAE equation:

$$C(x,t) = C^*\left(1 + \frac{D_0 k^2 t_0\left[\left(\frac{t}{t_0}+\tau_0\right)^{\gamma} - \tau_0^{\gamma}\right]}{\gamma(1-\eta)\ \tau_0^{\gamma-1}}\right)\frac{\sinh(kx)}{\sinh(kL)} \qquad (C.24)$$

and

$$D(t) = \frac{D_0 \left(\frac{t}{t_0} + \tau_0\right)^{\gamma-1} \gamma(1-\eta)}{D_0 k^2 t_0 \left[\left(\frac{t}{t_0} + \tau_0\right)^{\gamma} - \tau_0^{\gamma}\right] + \tau_0^{\gamma-1}\gamma(1-\eta)} \qquad (C.25)$$

Derivation of the General Expression for SAD current and constant $\mathcal{L}$

From (C.23) a non-algebraic expression relating k and the other system-specific parameters arises:

$$\frac{\sinh(kL)}{k} = \frac{nFAC^*D_0}{I_0\tau_0^{\gamma-1}} \qquad (C.26)$$

Practically, (C.26) is used to numerically solve for k, provided experimental determination of the system parameters on the right-hand side. Generally, though, in order for a positive real value of k to exist according to (C.26), the following inequality must hold:

$$L < \frac{nFAC^*D_0}{I_0\tau_0^{\gamma-1}} \qquad (C.27)$$

or

$$\frac{L\, I_0 \tau_0^{\gamma-1}}{nFAD_0} < C^* \qquad (C.28)$$

However, (C.23) into (C.28) gives

$$\frac{k\, L}{\sinh(kL)} < 1 \qquad (C.29)$$

Now $\mathcal{L}$ is defined as

$$\mathcal{L} \equiv \frac{\sinh(kL)}{k} > L \qquad (C.30)$$

with dimensions of length. To arrive at an expression for SAD current, we combine (C.23), (C.30), and (C.8), giving

$$I(t) = \frac{nFAC^* D_0}{\tau_0^{\gamma-1}\, \mathcal{L}} \left(\frac{t}{t_0} + \tau_0\right)^{\gamma-1} \qquad (C.31)$$

Derivation of Specific Expressions Used within the Work in Chapter 3

In order to avoid over-parameterization and satisfy intuitive constraint IV, I take $t_0 = 1s$ and $\tau_0 = 1$. Using these, the concentration and charge relations in (C.24) and (C.25) become:

$$C(x,\tau) = C^*\left(1 + \frac{\mathcal{D}_0 k^2[(\tau+1)^\gamma - 1]}{\gamma(1-\eta)}\right)\frac{\sinh(kx)}{\sinh(kL)} \qquad (C.32)$$

and

$$D(\tau) = \frac{D_0(\tau+1)^{\gamma-1}\,\gamma(1-\eta)}{\mathcal{D}_0 k^2[(\tau+1)^\gamma - 1]\; + \gamma(1-\eta)} \qquad (C.33)$$

where $\mathcal{D}_0$ is the initial stress-assisted diffusion constant multiplied by one second: $\mathcal{D}_0 \equiv D_0 * 1s$. Additionally, τ is dimensionless time defined as: $\tau \equiv \frac{t}{1s}$. The expressions (C.32) and (C.33) correspond to equations (3.3) and (3.4).

The expression for SAD current, (3.5), is found by using the aforementioned selected parameters in (C.31) giving

$$I(\tau) = \frac{nFAC^*D_0}{\mathcal{L}\,(\tau+1)^{1-\gamma}} \qquad (C.34)$$

again, where τ is dimensionless time defined as $\tau \equiv t/1s$. The charge expression used to fit raw charge data in this work is similarly found from (C.9)

$$Q(\tau) = \frac{\mathcal{I}_0}{\gamma}(\tau+1)^\gamma - \frac{\mathcal{I}_0}{\gamma} \qquad (C.35)$$

where $\mathcal{I}_0 \equiv I_0 * 1s$.

Additionally, from equation (C.28),

$$J_0 \equiv \frac{I_0}{A} < \frac{nFC^* D_0}{\tau_0^{\gamma-1} L} \qquad (\mathrm{C}.33)$$

and with the allowance of $\tau_0 = 1$, as mentioned above, Equation (3.6) is retrieved

$$J_0 \equiv \frac{I_0}{A} < \frac{nFC^* D_0}{L} \qquad (C.34)$$

Appendix D: Pascalammetry Details

D.1 Geometry and Materials of Microbattery Probes in Chapter 3

The microbattery probe geometry and measurement system (JEOL JSPM-4500A) provides a line-of-site side view of the cathode-electrolyte junction edge, a perspective not afforded in typical solid-state coin cells. This perspective is utilized for intermittent SEM measurements to observe stress-induced morphological changes and degradation, like cracking. The small cross-sectional area of the active electrolyte facilitates the introduction of large stresses by modest applied compressive forces. This principle has been exploited in a number of works to apply local high pressure with scanning probe tips[155].

I next describe the choice of Si cathode and electrolyte materials. In light of the asymmetrical swelling of lithiated Si[156], the Si(111) facet was chosen to minimize swelling[157]. To ensure that lithium oxide is the sole electrolyte in the system, the silicon oxide was removed from the Si cathode by resistive heating in UHV[49]. The Si(111) surface was heated for ~60s at 1,150˚C, quickly cooled to 900˚C, and then more slowly cooled to room temperature to reconstruct the Si surface into Si(111)-7x7[49]. This surface is metallic[158], and a good electron and heat conductor, which minimizes Joule or stress heating. Importantly, the ca. 1mm x 7mm x 400μu thick cathode has a surface area that is 3,500 times larger than that of the electrolyte, thus serving as both cathode, and infinite heat sink. In order to suppress possible electron leakage currents during pascalammetry experiments, a solid-state electrolyte with a large electron band gap is chosen:

lithium oxide is selected as it's band gap is reported in the literature to range between 7-16 eV[159,160]. Summarily, the experimental platform, materials, and geometry are optimized for use in our pascalammetry measurements.

D.2 Microbattery Probe Fabrication

A coating of Li is galvanostatically deposited onto the end of a bluntly-cut tungsten scanning tunneling microscope probe (diameter of 250 μm) via electrodeposition. About 3mm of the STM tip-end is submerged in the aprotic electrolyte, 1M $LiClO_4$ in propylene carbonate, within an Argon glovebox. Lithium metal served as counter electrode, separated from the W tip by a distance of ~2cm. The galvanostatically controlled current was held at 10 μA for 3hours, generating films with nominal thicknesses of ~10 μm. Li-coated W tips were stored in Argon. Prior to use, tips were exposed to atmospheric oxygen for < 10min, generating an ca. 1 micron thick lithium oxide outer film before being placed under vacuum and transferred into the ultra-high vacuum chamber for measurements.

D.3 Time Constant for Capacitive Charging/Discharging

As mentioned in the chapter 3, initial contact between the microbattery probe and Si cathode is equivalent to a potential-step voltammetry experiment in that the circuit doesn't "close" until contact is made. Then, capacitive charging/discharging will spontaneously proceed as $I_{cap}(t) \propto exp(-t/\tau)$. Of course, the measured current also consists of diffusion-limited faradaic current that proceeds in time as $I_{dif-lim}(t) \propto t^{-1/2}$. Due to the differences in time-

dependence, determining the lifetime of any capacitive effects is readily accessible in such an experiment by data analysis. When plotting the unstressed charge versus time (Fig 3B, black dashes), and choosing the origin of time to be congruent with moment of initial current decay, we find that deviation from linearity ends (end of capacitive effects) at some point before 1s, most likely, <0.5s.

D.4 Capacitive Time Constant is Independent of Contact Area

The time constant τ, for capacitive charging/discharging through a resistor, with contact resistance, is

$$\tau = RC = (R_{bulk} + R_{contact})C = \left(\frac{\rho_{bulk}\, L}{A_{contact}} + \frac{\rho_{contact}}{A_{contact}}\right)\frac{\epsilon\, A_{contact}}{L}$$

$$\tau = \epsilon\, \rho_{bulk} + \frac{\epsilon\, \rho_{contact}}{L} \qquad (D1)$$

It is evident in (D1) that the time constant is independent of the contact area.

D.5 Applied Compressive Forces and Stresses by Piezo Actuator

During the stress ramp/step of a pascalammetry experiment, compressive forces are applied to the operando electrochemical device by means of expanding a bipolar piezoelectric actuator (Fig. 1C). Stress is proportional to the applied force, and inversely proportional to cross-sectional area, thus applied compressive forces generate spatially variant compressive stresses along the probe axis. Because the

device's smallest cross sectional area normal to the applied compressive force is at the end of the microbattery probe, this is where the greatest pressure/stress will be – in the lithium oxide electrolyte. Via SEM imaging, this contact area is found to be ca. 2,000 μm^2.

In order to estimate the maximum stress at the tip end during a pascalammetry measurement, the maximum force the bipolar piezoelectric actuator can produce needs to be known. This value can be estimated by use of fundamental piezoelectric material constants (in our case, those for piezo material PZT-5H), piezo voltage, and geometrical parameters. For the transverse piezoelectric effect, used in our case, this maximal "blocking force" in the first direction is

$$F_1^{blocking} = \frac{d_{31}}{s_{11}} A E_3 \qquad (D2)$$

where $d_{31} = S_1/E_3$ and S_1 is the piezo strain in the 1st direction resulting from an electric field, E_3, applied in the 3rd direction. In (D2) $s_{11} = S_1/\sigma_1$ and σ_1 is the stress generated in the 1st direction by a strain S_1 in the first direction. Also for (D2), A is the cross-sectional area of the piezo actuator in the 2,3-plane, normal to the induced piezo force in the 1st direction. Finally, E_3 is the electric field applied to the piezo in the 3rd direction that generates piezo strain in the 1st direction by the transverse piezoelectric effect. We note in this convention, the 1st direction is parallel with the microbattery probe axis, normal to the surface of the Si(111) cathode.

The blocking force, equation (D2), is the force that would theoretically be generated by the actuator in the following event. Consider a case in which the piezoelectric actuator is in a state of complete contraction by the application of some appropriate bias voltage (in our case by the application of -150V). In this contracted state, an infinitely strong barrier is placed in front of the compressed actuator in such a way that the actuator is constrained to stay in the compressed state regardless of piezo voltage (the electric field in the 3rd direction). Then, the piezo voltage is ramped from the value corresponding to maximum contraction, to a voltage corresponding to maximum expansion (in our case -150V to 150V). This would result in a free actuator expanding by its maximum amount (in our case 1.5 μm). However, because the infinitely strong barrier will not comply, ramping of the piezo voltage in this way rather results in a force (stress) that is proportional to the applied bias (electric field), according to equation (D2). By plugging our piezo and voltage properties into (D2), this idealized maximum applied force to the microbattery along the probe-axis direction is ca. 318 N. This maximum applied force would generate a maximum applied stress of ca. 159 GPa in the lithium oxide solid-state electrolyte. This is found by the ratio of 159 N to $2{,}000\ \mu m^2$.

In our pascalammetry measurements, the full-cell solid-state microbattery takes the position of the infinitely strong barrier. During the stress ramp of a pascalammetry experiment the softest system material, Li, will comply to the compressive forces. The amount of compliance (1.5 μm maximum) depends on the magnitude of the applied compressive forces. If the force required to achieve complete compliance is less than the blocking force of 318N, complete compliance

will occur. An estimate for this "compliance force" is found by using Young's modulus of Li (4.9 GPa), the smallest cross-sectional area of the Li normal to the compressive force (ca. 2,000 μm^2), the uncompressed Li thickness (ca. 9 μm), and the total compression amount (1.5 μm). In this way, we approximate the compliance force to be 1.6 N, which is less than the blocking force, and hence the best estimate for the system force during the stress step of a pascalammetry measurement. This compressive force corresponds to a maximum stress of 800 MPa in the lithium oxide electrolyte during a pascalammetry experiment.

D.6 SAD and Liquid Electrolyte Battery Systems

Describing SAD via the DAT can be applied to physical scenarios where no creation of active species is expected, like in liquid electrolytes, by setting η to zero. This reduces Equation (3.2) in chapter 3 to Fick's second law with a time-dependent diffusion coefficient, and all solutions within the manuscript and supplemental persist with $\eta = 0$. The blue curve in the bottom plot of Figure 24 in chapter 3 is the normed time-dependent diffusion coefficient in such a limiting case. We note that even with $\eta = 0$, the concentrations during SAD will still increase in time. Therefore, if a full cell liquid electrolyte battery experiences sufficient pressure/stress to induce SAD, increasing concentrations (especially at the oxidation interface) may spur Li dendrite growth.

D.7 Plotting Parameters

The following parameters used for plotting in chapter 3:

$D_0 = 10^{-11}\,\frac{cm^2}{s}$, Conservative estimate, mid-range non-stressed value [161]

$A = 2{,}000\ \mu m^2$, Order of magnitude value based on experimental SEM data

$L = 1\ \mu m$, Experimental estimate based on Li oxidation time

$k = 2.61312\,\frac{1}{\mu m}$, Numerically determined via DAT (26)

$I_0 = 10{\times}10^{-12}\ pA$, Average Initial experimental SAD current (order of magnitude)

$\gamma = 0.8$, Experimental Average

$\eta = 0.1$, Estimate of 10% change in [45]concentration due to local active species creation

$C^* = 0.00013453\,\frac{mol}{cm^3}$, 1/1000 of the stoichiometric Concentration of Li in Li_2O

Bibliography

[1] C. Rosenzweig *et al.*, Nature **453**, 353 (2008).
[2] M. Höök and X. Tang, Energy Policy **52**, 797 (2013).
[3] S. J. Kazempour, M. P. Moghaddam, M. R. Haghifam, and G. R. Yousefi, Renewable Energy **34**, 2630 (2009).
[4] F. Sissine, (Library of Congress Washington DC Congressional Research Service, 2007).
[5] I. B. Fridleifsson, Renewable Sustainable Energy Rev. **5**, 299 (2001).
[6] H. R. Zhao, Q. W. Wu, S. J. Hu, H. H. Xu, and C. N. Rasmussen, Appl. Energy **137**, 545 (2015).
[7] V. Fthenakis and H. C. Kim, Renewable Sustainable Energy Rev. **14**, 2039 (2010).
[8] H. J. Snaith, J. Phys. Chem. Lett. **4**, 3623 (2013).
[9] L. Lu, T. Zheng, Q. Wu, A. M. Schneider, D. Zhao, and L. Yu, Chem. Rev. **115**, 12666 (2015).
[10] D. Bi *et al.*, Sci. Adv. **2**, e1501170 (2016).
[11] D. Larcher and J. M. Tarascon, Nat. Chem. **7**, 19 (2015).
[12] E. S. Beh, D. De Porcellinis, R. L. Gracia, K. T. Xia, R. G. Gordon, and M. J. Aziz, ACS Energy Lett. **2**, 639 (2017).
[13] L. Grande, E. Paillard, J. Hassoun, J. B. Park, Y. J. Lee, Y. K. Sun, S. Passerini, and B. Scrosati, Adv. Mater. **27**, 784 (2015).
[14] B. Huskinson *et al.*, Nature **505**, 195 (2014).
[15] J. Liu, C. Guan, C. Zhou, Z. Fan, Q. Ke, G. Zhang, C. Liu, and J. Wang, Adv. Mater. **28**, 8732 (2016).
[16] Y. Orikasa *et al.*, Sci. Rep. **4**, 5622 (2014).
[17] J. F. Parker, C. N. Chervin, I. R. Pala, M. Machler, M. F. Burz, J. W. Long, and D. R. Rolison, Science **356**, 415 (2017).
[18] H. Wang, Y. Yang, Y. Liang, J. T. Robinson, Y. Li, A. Jackson, Y. Cui, and H. Dai, Nano Lett. **11**, 2644 (2011).
[19] M. Le Thai, G. T. Chandran, R. K. Dutta, X. Li, and R. M. Penner, ACS Energy Lett. **1**, 57 (2016).
[20] L. Suo, O. Borodin, T. Gao, M. Olguin, J. Ho, X. Fan, C. Luo, C. Wang, and K. Xu, Science **350**, 938 (2015).
[21] V. Thangadurai, S. Narayanan, and D. Pinzaru, Chem. Soc. Rev. **43**, 4714 (2014).
[22] K. K. Fu *et al.*, Sci. Adv. **3**, e1601659 (2017).
[23] X. Han *et al.*, Nat. Mater. **16**, 572 (2017).
[24] J. Zhi, A. Z. Yazdi, G. Valappil, J. Haime, and P. Chen, Sci. Adv. **3**, e1701010 (2017).
[25] C. Liu, E. I. Gillette, X. Chen, A. J. Pearse, A. C. Kozen, M. A. Schroeder, K. E. Gregorczyk, S. B. Lee, and G. W. Rubloff, Nat. Nanotechnol. **9**, 1031 (2014).
[26] J. W. Long, B. Dunn, D. R. Rolison, and H. S. White, Chem. Rev. **104**, 4463 (2004).

[27] A. A. Talin, D. Ruzmetov, A. Kolmakov, K. McKelvey, N. Ware, F. El Gabaly, B. Dunn, and H. S. White, ACS Appl. Mater. Interfaces **8**, 32385 (2016).
[28] F. C. Strobridge *et al.*, Chem. Mater. **27**, 2374 (2015).
[29] P. D. Wang, X. Y. Zhang, L. Yang, X. Y. Zhang, M. Yang, H. S. Chen, and D. N. Fang, Extreme Mech. Lett. **9**, 459 (2016).
[30] R. Y. Wang, C. D. Wessells, R. A. Huggins, and Y. Cui, Nano Lett. **13**, 5748 (2013).
[31] K. Eom, T. Joshi, A. Bordes, I. Do, and T. F. Fuller, J. Power Sources **249**, 118 (2014).
[32] N. Liu, Z. Lu, J. Zhao, M. T. McDowell, H. W. Lee, W. Zhao, and Y. Cui, Nat. Nanotechnol. **9**, 187 (2014).
[33] A. Krause *et al.*, Sci. Rep. **6**, 27982 (2016).
[34] G. Binnig and H. Rohrer, Surf. Sci. **126**, 236 (1983).
[35] C. J. Chen, *Introduction to Scanning Tunneling Microscopy* (Oxford University Press, New York, NY, 2007), 2nd edn., Monographs on the Physics and Chemistry of Materials.
[36] G. Binnig, C. F. Quate, and C. Gerber, Phys. Rev. Lett. **56**, 930 (1986).
[37] F. J. Giessibl, Rev. Mod. Phys. **75**, 949 (2003).
[38] L. Gross, F. Mohn, N. Moll, G. Meyer, R. Ebel, W. M. Abdel-Mageed, and M. Jaspars, Nat. Chem. **2**, 821 (2010).
[39] L. Gross, F. Mohn, N. Moll, P. Liljeroth, and G. Meyer, Science **325**, 1110 (2009).
[40] M. Kageshima, H. Jensenius, M. Dienwiebel, Y. Nakayama, H. Tokumoto, S. P. Jarvis, and T. H. Oosterkamp, Appl. Surf. Sci. **188**, 440 (2002).
[41] R. Garcia, A. W. Knoll, and E. Riedo, Nat. Nanotechnol. **9**, 577 (2014).
[42] M. Nonnenmacher, M. P. O'Boyle, and H. K. Wickramasinghe, Appl. Phys. Lett. **58**, 2921 (1991).
[43] W. Melitz, J. Shen, A. C. Kummel, and S. Lee, Surf. Sci. Rep. **66**, 1 (2011).
[44] H. J. Zandvliet and A. van Houselt, Annu. Rev. Anal. Chem. **2**, 37 (2009).
[45] R. M. Feenstra, Surf. Sci. **299-300**, 965 (1994).
[46] B. Voigtländer, *Scanning Probe Microscopy* (Springer, 2016).
[47] P. K. Hansma, V. B. Elings, O. Marti, and C. E. Bracker, Science **242**, 209 (1988).
[48] D. A. Bonnell and S. V. Kalinin, *Scanning Probe Microscopy for Energy Research* (World Scientific, 2013), Vol. 7.
[49] J. M. Larson, S. C. Bharath, W. G. Cullen, and J. E. Reutt-Robey, Small **11**, 4946 (2015).
[50] L. Danis, S. M. Gateman, C. Kuss, S. B. Schougaard, and J. Mauzeroll, ChemElectroChem **4**, 6 (2017).
[51] C. C. Chen, Y. Zhou, and L. A. Baker, Annu. Rev. Anal. Chem. **5**, 207 (2012).
[52] A. J. Bard and M. V. Mirkin, *Scanning Electrochemical Microscopy* (CRC Press, 2012).
[53] E. Strelcov, S. M. Yang, S. Jesse, N. Balke, R. K. Vasudevan, and S. V. Kalinin, Nanoscale **8**, 13838 (2016).

[54] M. H. Hong, K. H. Kim, J. Bae, and W. Jhe, Appl. Phys. Lett. **77**, 2604 (2000).
[55] K. T. Rodolfa, A. Bruckbauer, D. Zhou, A. I. Schevchuk, Y. E. Korchev, and D. Klenerman, Nano Lett. **6**, 252 (2006).
[56] M. G. Schrlau, E. M. Falls, B. L. Ziober, and H. H. Bau, Nanotechnology **19**, 015101 (2008).
[57] F. O. Laforge, J. Carpino, S. A. Rotenberg, and M. V. Mirkin, Proc. Natl. Acad. Sci. U.S.A. **104**, 11895 (2007).
[58] M. Karhanek, J. T. Kemp, N. Pourmand, R. W. Davis, and C. D. Webb, Nano Lett. **5**, 403 (2005).
[59] C. H. Chen, C. T. Lin, Y. H. Lee, K. K. Liu, C. Y. Su, W. Zhang, and L. J. Li, Small **8**, 43 (2012).
[60] L. Ying, S. S. White, A. Bruckbauer, L. Meadows, Y. E. Korchev, and D. Klenerman, Biophys. J. **86**, 1018 (2004).
[61] D. Golberg, P. M. F. J. Costa, M. Mitome, S. Hampel, D. Haase, C. Mueller, A. Leonhardt, and Y. Bando, Adv. Mater. **19**, 1937 (2007).
[62] L. Dong, X. Tao, L. Zhang, X. Zhang, and B. J. Nelson, Nano Lett. **7**, 58 (2007).
[63] G. E. Begtrup, W. Gannett, T. D. Yuzvinsky, V. H. Crespi, and A. Zettl, Nano Lett. **9**, 1835 (2009).
[64] K. Svensson, H. Olin, and E. Olsson, Phys. Rev. Lett. **93**, 145901 (2004).
[65] K. Edgar, S. C. Hendy, D. Schebarchov, and R. D. Tilley, Small **7**, 737 (2011).
[66] M. Loffler, U. Weissker, T. Muhl, T. Gemming, J. Eckert, and B. Buchner, Adv. Mater. **23**, 541 (2011).
[67] M. Sun and Y. Gao, Nanotechnology **23**, 065704 (2012).
[68] S. Coh, W. Gannett, A. Zettl, M. L. Cohen, and S. G. Louie, Phys. Rev. Lett. **110**, 185901 (2013).
[69] S. Coh, S. G. Louie, and M. L. Cohen, Phys. Rev. B **88**, 045424 (2013).
[70] T. A. Hilder and J. M. Hill, Small **5**, 300 (2009).
[71] B. C. Regan, S. Aloni, R. O. Ritchie, U. Dahmen, and A. Zettl, Nature **428**, 924 (2004).
[72] S. Kramer, R. R. Fuierer, and C. B. Gorman, Chem. Rev. **103**, 4367 (2003).
[73] H. T. Soh, K. W. Guarini, and C. F. Quate, *Scanning Probe Lithography* (Springer Science & Business Media, New York, 2001), Vol. 7, Microsystems.
[74] R. D. Piner, J. Zhu, F. Xu, S. Hong, and C. A. Mirkin, Science **283**, 661 (1999).
[75] N. Balke, S. Jesse, Y. Kim, L. Adamczyk, A. Tselev, I. N. Ivanov, N. J. Dudney, and S. V. Kalinin, Nano Lett. **10**, 3420 (2010).
[76] N. Balke *et al.*, Nat. Nanotechnol. **5**, 749 (2010).
[77] S. Jesse, N. Balke, E. Eliseev, A. Tselev, N. J. Dudney, A. N. Morozovska, and S. V. Kalinin, ACS Nano **5**, 9682 (2011).
[78] A. L. Lipson, R. S. Ginder, and M. C. Hersam, Adv. Mater. **23**, 5613 (2011).
[79] A. L. Lipson and M. C. Hersam, J. Phys. Chem. C **117**, 7953 (2013).

[80] M. S. Gupalo, I. L. Yarish, V. M. Zlupko, and Y. Suchorski, J. Vac. Sci. Technol. B **15**, 491 (1997).
[81] M. S. Gupalo, I. L. Yarish, V. M. Zlupko, Y. Suchorski, and J. H. Block, Surf. Sci. **350**, 176 (1996).
[82] M. S. Gupalo, I. L. Yarish, V. M. Zlupko, and Y. Suchorski, in *Ivmc '96 - 9th International Vacuum Microelectronics Conference* (Saint-Petersburg, Russia, 1996), pp. 481.
[83] B. J. Landi, M. J. Ganter, C. D. Cress, R. A. DiLeo, and R. P. Raffaelle, Energy Environ. Sci. **2**, 638 (2009).
[84] M. F. De Volder, S. H. Tawfick, R. H. Baughman, and A. J. Hart, Science **339**, 535 (2013).
[85] R. H. Baughman, A. A. Zakhidov, and W. A. de Heer, Science **297**, 787 (2002).
[86] S. W. Lee, N. Yabuuchi, B. M. Gallant, S. Chen, B. S. Kim, P. T. Hammond, and Y. Shao-Horn, Nat. Nanotechnol. **5**, 531 (2010).
[87] Y. Chen, X. Li, K. Park, J. Song, J. Hong, L. Zhou, Y. W. Mai, H. Huang, and J. B. Goodenough, J. Am. Chem. Soc. **135**, 16280 (2013).
[88] Y. Liu *et al.*, ACS Nano **5**, 7245 (2011).
[89] W. F. Stokey, in *Harris' Shock and Vibration Handbook*, edited by C. M. Harris, and A. G. Piersol (McGraw-Hill, New York, NY, 2002).
[90] L. Kuipers and J. W. Frenken, Phys. Rev. Lett. **70**, 3907 (1993).
[91] N. Agrait, G. Rubio, and S. Vieira, Phys. Rev. Lett. **74**, 3995 (1995).
[92] G. L. Che, B. B. Lakshmi, E. R. Fisher, and C. R. Martin, Nature **393**, 346 (1998).
[93] E. Frackowiak, S. Gautier, H. Gaucher, S. Bonnamy, and F. Beguin, Carbon **37**, 61 (1999).
[94] G. Maurin, C. Bousquet, F. Henn, P. Bernier, R. Almairac, and B. Simon, Chem. Phys. Lett. **312**, 14 (1999).
[95] G. Maurin, C. Bousquet, F. Henn, P. Bernier, R. Almairac, and B. Simon, Solid State Ionics **136**, 1295 (2000).
[96] Z. Yang, Solid State Ionics **143**, 173 (2001).
[97] Z. H. Yang, Y. Feng, Z. F. Li, S. B. Sang, Y. H. Zhou, and L. H. Zeng, J. Electroanal. Chem. **580**, 340 (2005).
[98] J. Zhao, A. Buldum, J. Han, and J. Ping Lu, Phys. Rev. Lett. **85**, 1706 (2000).
[99] P. Dubot and P. Cenedese, Phys. Rev. B **63**, 241402 (2001).
[100] T. Kar, J. Pattanayak, and S. Scheiner, J. Phys. Chem. A **105**, 10397 (2001).
[101] J. L. Yang, H. J. Liu, and C. T. Chan, Phys. Rev. B **64**, 085420 (2001).
[102] V. Meunier, J. Kephart, C. Roland, and J. Bernholc, Phys. Rev. Lett. **88**, 075506 (2002).
[103] K. Nishidate, K. Sasaki, Y. Oikawa, M. Baba, and M. Hasegawa, e-J. Surf. Sci. Nanotechnol. **3**, 358 (2005).
[104] K. Nishidate and M. Hasegawa, Phys. Rev. B **71**, 245418 (2005).
[105] A. Udomvech, T. Kerdcharoen, and T. Osotchan, Chem. Phys. Lett. **406**, 161 (2005).

[106] M. W. Zhao, Y. Y. Xia, X. D. Liu, Z. Y. Tan, B. D. Huang, F. Li, Y. J. Ji, and C. Song, Phys. Lett. A **340**, 434 (2005).
[107] M. W. Zhao, Y. Y. Xia, and L. M. Mei, Phys. Rev. B **71**, 165413 (2005).
[108] D. Jeon, T. Hashizume, and T. Sakurai, Appl. Surf. Sci. **94-95**, 493 (1996).
[109] K. H. Wu, Sci. Technol. Adv. Mater. **6**, 789 (2005).
[110] M. G. Littman, M. M. Kash, and D. Kleppner, Phys. Rev. Lett. **41**, 103 (1978).
[111] E. G. Seebauer and C. E. Allen, Prog. Surf. Sci. **49**, 265 (1995).
[112] R. Gomer, Rep. Prog. Phys. **53**, 917 (1990).
[113] I. Wolfram Research, *Mathematica* (Wolfram Research, Inc., Champaign, Illinois, 2012), Version 9.0 edn.
[114] C. Weindel, H. J. Jansch, J. J. Paggel, R. Veith, and D. Fick, Surf. Sci. **543**, 29 (2003).
[115] C. Weindel, H. J. Jänsch, G. Kirchner, H. Kleine, J. J. Paggel, J. Roth, H. Winnefeld, and D. Fick, Phys. Rev. B **71**, 115318 (2005).
[116] Y. Hasegawa, I. Kamiya, T. Hashizume, T. Sakurai, H. Tochihara, M. Kubota, and Y. Murata, J. Vac. Sci. Technol. A **8**, 238 (1990).
[117] A. J. Jackson, C. Tate, T. E. Gallon, P. J. Bassett, and J. A. D. Matthew, J. Phys. F: Met. Phys. **5**, 363 (1975).
[118] Z. P. Hu and A. Ignatiev, Phys. Rev. B **30**, 4856 (1984).
[119] A. Cassell, L. Delzeit, C. Nguyen, R. Stevens, J. Han, and M. Meyyappan, J. Phys. IV **11**, 401 (2001).
[120] J. M. Bonard, H. Kind, T. Stockli, and L. A. Nilsson, Solid-State Electron. **45**, 893 (2001).
[121] R. Stevens, C. Nguyen, and M. Meyyappan, IEEE Trans. Nanotechnol. **5**, 255 (2006).
[122] B. C. Park, K. Y. Jung, W. Y. Song, O. Beom-Hoan, and S. J. Ahn, Adv. Mater. **18**, 95 (2006).
[123] L. Kuipers, M. S. Hoogeman, and J. W. M. Frenken, Surf. Sci. **340**, 231 (1995).
[124] M. Ebner, F. Marone, M. Stampanoni, and V. Wood, Science **342**, 716 (2013).
[125] N. Nitta, F. X. Wu, J. T. Lee, and G. Yushin, Mater. Today **18**, 252 (2015).
[126] J. Vetter *et al.*, J. Power Sources **147**, 269 (2005).
[127] V. Yufit, P. Shearing, R. W. Hamilton, P. D. Lee, M. Wu, and N. P. Brandon, Electrochem. Commun. **13**, 608 (2011).
[128] L. Ji, Z. S. Guo, and Y. J. Wu, Energy Technol. **5**, 1702 (2017).
[129] J. Q. Zhang, B. Lu, Y. C. Song, and X. Ji, J. Power Sources **209**, 220 (2012).
[130] F. G. Cottrell, Z. Phys. Chem. **42**, 385 (1903).
[131] A. J. Bard and L. R. Faulkner, *Electrochemical Methods: Fundamentals and Applications* (Wiley, New York, 2001).
[132] R. G. Compton and C. E. Banks, *Understanding Voltammetry* (Imperial College Press, London, 2011).

[133] A. H. Cottrell, in *Report of a Conference on Strength of Solids* (Physical Society, London, 1948), pp. 30.
[134] E. C. Aifantis, Acta Mech. **37**, 265 (1980).
[135] R. Wilson and E. Aifantis, Acta Mech. **45**, 273 (1982).
[136] D. J. Unger and E. Aifantis, Acta Mech. **47**, 117 (1983).
[137] Y. Weitsman, J. Mech. Phys. Solids **35**, 73 (1987).
[138] A. F. Bower, P. R. Guduru, and V. A. Sethuraman, J. Mech. Phys. Solids **59**, 804 (2011).
[139] H. Haftbaradaran, J. Song, W. A. Curtin, and H. J. Gao, J. Power Sources **196**, 361 (2011).
[140] B. Yang, Y. P. He, J. Irsa, C. A. Lundgren, J. B. Ratchford, and Y. P. Zhao, J. Power Sources **204**, 168 (2012).
[141] Y. C. Song, X. J. Shao, Z. S. Guo, and J. Q. Zhang, J. Phys. D: Appl. Phys. **46**, 105307 (2013).
[142] D. Giovanelli, N. S. Lawrence, and R. G. Compton, Electroanalysis **16**, 789 (2004).
[143] J. Crank, *The Mathematics of Diffusion* (Oxford University Press, Oxford, 1975), 2nd edn.
[144] R. M. Feenstra, Phys. Rev. B **44**, 13791 (1991).
[145] B. Naydenov and J. J. Boland, Phys. Rev. B **82**, 245411 (2010).
[146] M. Passoni, F. Donati, A. L. Bassi, C. S. Casari, and C. E. Bottani, Phys. Rev. B **79**, 045404 (2009).
[147] S. M. George, Chem. Rev. **110**, 111 (2009).
[148] H. M. Cheng, F. M. Wang, J. P. Chu, R. Santhanam, J. Rick, and S. C. Lo, J. Phys. Chem. C **116**, 7629 (2012).
[149] M. T. McDowell, S. W. Lee, J. T. Harris, B. A. Korgel, C. Wang, W. D. Nix, and Y. Cui, Nano Lett. **13**, 758 (2013).
[150] J. W. Wang *et al.*, Nano Lett. **13**, 709 (2013).
[151] I. D. Scott, Y. S. Jung, A. S. Cavanagh, Y. Yan, A. C. Dillon, S. M. George, and S. H. Lee, Nano Lett. **11**, 414 (2011).
[152] E. J. Fuller, F. E. Gabaly, F. Leonard, S. Agarwal, S. J. Plimpton, R. B. Jacobs-Gedrim, C. D. James, M. J. Marinella, and A. A. Talin, Adv. Mater. **29**, 1604310 (2017).
[153] G. W. Rubloff and S. S. Lee, Curr. Opin. Solid State Mater. Sci. **19**, 227 (2015).
[154] F. J. Giessibl, F. Pielmeier, T. Eguchi, T. An, and Y. Hasegawa, Phys. Rev. B **84**, 125409 (2011).
[155] C. Lee, X. Wei, J. W. Kysar, and J. Hone, Science **321**, 385 (2008).
[156] X. H. Liu *et al.*, Nano Lett. **11**, 3312 (2011).
[157] X. H. Liu *et al.*, Nat. Nanotechnol. **7**, 749 (2012).
[158] K. Oura, V. Lifshits, A. Saranin, A. Zotov, and M. Katayama, *Surface Science: An Introduction* (Springer Science & Business Media, 2013).
[159] E. A. Mikajlo, K. L. Nixon, V. A. Coleman, and M. J. Ford, J. Phys.: Condens. Matter **14**, 3587 (2002).
[160] Y. Duan and D. C. Sorescu, Phys. Rev. B **79**, 014301 (2009).
[161] J. Y. Huang *et al.*, Science **330**, 1515 (2010).